AMORPHOUS TUNGSTEN OXIDE AND NOVEL MOLYBDENUM DOPED TUNGSTEN OXIDE BASED SENSORS MADE PHOTOCHEMICALLY AT ROOM TEMPERATURE FOR SUB-PPM NO_x DETECTION

by

Chu-Hui Winnie Chu

M.Sc. University of Manitoba (Manitoba), 1992
B.Sc. Chung-Yuan Christian University (Taiwan), 1988

A THESIS SUBMITTED IN PARTIAL FULFILMENT OF
THE REQUIREMENTS FOR THE DEGREE OF
DOCTOR OF PHILOSOPHY
in the Department
of
Chemistry

Simon Fraser University
February 1998

0-612-37691-5

ABSTRACT

The objective of this thesis was to use a novel process to fabricate and characterise semiconducting metal oxide sensors which detect NO_x. This process involves the photochemical deposition of thin solid films of amorphous precursor complexes. The precursor film is exposed to light and photochemically produces the desired material, in this case the sensing element.

The metal complexes, $M(CO)_5PPh_3$ and $M(CO)_4(LL)_5$ (M= Cr, Mo, W; LL= $H(CH_3)NCH_2CH_2NH(CH_3)$, $H_2NCH_2CH_2N(C_2H_5)_2 \equiv (Et_2\text{-en})$, $H_2NCH_2CH_2NH_2$) were synthesised. Upon spin coating, these complexes all form photosensitive amorphous films. The film quality depends on both the metal centre and the ligands. The best starting materials were found to be $M(CO)_4(Et_2\text{-en})$ (M = Cr, Mo, W). Auger analysis indicates the formation of contamination free $Cr_{0.65}O$, $Mo_{0.27}O$, and $W_{0.5}O$ from these precursors.

The solid state photochemistry of the above metal complexes is described. The complexes containing the nitrogen donor ligands were found to follow a one photon process. The PPh_3 complexes were found to decompose via a two photon process. The quantum yields were determined with a kinetic equation derived for a one or a sequential two photon process. The photoefficiency was found to depend on the metal centre as well as the ligand environment.

Finally, we will conclude by presenting the characteristics of tungsten and molybdenum tungsten oxide sensors at various operating temperatures. The electron transport mechanisms for semiconducting metal oxides are reported. The electron flow in amorphous tungsten oxide devices was found to follow the variable range hopping conduction whereas the electron conduction in amorphous molybdenum doped tungsten oxides was via the single electron hopping mechanism. These sensors were found to respond to sub-ppm NO_x at ~100°C. The reproducibility, specificity and stability of these devices promise a reliable NO_x sensor operation for environmental monitoring.

DEDICATION

To Grandpa and Grandma

ACKNOWLEDGEMENTS

I would like to thank my supervisor Dr. Ross Hill for his guidance, patience and assistance during these years.

The clean room technical training and supervising from Dr. G. Chapmen and Bill Woods are greatly appreciated. Thanks also owes to Dr. M. Jamal Deen and Plamen Kolev for their patient teaching and valuable discussion as well as the continuous encouragement throughout the year.

I wish to thank Susan Einstein for her assistance in writing. I would also like to thank Fred H. Chin for his friendship and countless advices over these years. The support from my friends Grace, Steve, Susan, J. Pablo, Julie, Warren, Jimmy, Doug, Tammy, Harry, Frank, Papa and Mama Orfino was a constant source of inspiration, thanks to all of you.

I would like to thank my labmates for their assistance and valuable discussions. I would also like to thank Dr. J. Deen, Dr. P. Yager, Dr. D. Sutton, Dr. R. Hill and Dr. A. Bennet for their patient in reading my thesis and their important recommendations on the revision of the thesis.

Finally, thanks to Johnathon, Susan, Vivian, Miles, Julia and my grandparents for their believing in me and the unconditional love.

TABLE OF CONTENTS

Page Number

LIST OF ABBREVIATIONS AND SYMBOLS

AES	Auger electron spectroscopy
en	ethylenediamine $H_2NC_2H_4NH_2$
Me_2-en	*N, N'*-dimethylethylenediamine $(CH_3)HNC_2H_4N(CH_3)H$
Et_2-en	*N, N*-diethylethylenediamine $(C_2H_5)_2NC_2H_4NH_2$
CT	charge transfer
LF	ligand field
CVD	chemical vapour deposition
VE	vacuum evaporation
IBE	ion beam evaporation
MBE	molecular beam evaporation
M	transition metal
L	ligand
ϕ_1	quantum yield for the photochemical reaction of the starting material
ϕ_2	quantum yield for the photochemical reaction of the intermediate
FTIR	Fourier transformed infrared
A	absorbance in the UV/VIS spectrum
I_o	incident light intensity in units of E cm^{-2} s^{-1}
I_T	intensity of the incident light emerging from the sample
I_A	light absorbed by the sample
S	starting material
P	product
B	intermediate
A(t)	absorbance in the UV/VIS spectra at time t
A(f)	final absorbance in the UV/VIS spectra
A(0)	absorbance in the UV/VIS spectra at time zero
x	mole fraction

A^s	absorbance due to the starting material
A^p	absorbance due to the product
$h\nu$	energy of a photon
ε_A	extinction coefficient of S in the UV/VIS spectrum
ε_B	extinction coefficient of B in the UV/VIS spectrum
ε_a	extinction coefficient of S in the FTIR spectrum
ε_b	extinction coefficient of B in the FTIR spectrum
[S]	concentration of the starting material
$[S_o]$	initial concentration of the starting material
A^t	FTIR absorbance at time t
A^o	FTIR absorbance at time zero
HOMO	highest occupied molecular orbital
LUMO	lowest unoccupied molecular orbital
MO	molecular orbital
IR	infrared
2θ	diffraction angle
UV	ultraviolet
XRD	X-ray diffraction
V	Voltage
I	current
R	resistance
ρ	resistivity
T	Absolute temperature
G	Conductance
J	Current density
F	Electric field
E_a	Activation energy
$q\phi_B$	Barrier height
k	Boltzman's constant

e	elementary charge
Z	cross section
J_h	current density corrected with temperature
σ	conductivity
χ^2	correlation coefficient
λ	wavelength of light
l	distance between the two points at which the voltage is measured
d	lattice spacing
n	an integer
η^1	monodentate
η^2	bidentate
h	Planck constant
LEED	low energy electron diffraction
SPA	spot profile analysis
EPR	electron paramagnetic resonance
XPA	x-ray photoemission spectroscopy
ELS	electron-energy-loss spectroscopy
TDS	thermal desorption spectroscopy
STM	scanning tunnelling microscopy
TEM	tunnelling electron microscopy

LIST OF FIGURES

Page Number

LIST OF TABLES

CHAPTER 1

Introduction

1.1 Sensors

There is a great demand for sensors which are capable of detecting toxic gases in the atmosphere. The reason for such demand stems from environmental and safety concerns, since the toxic gases released from automobile exhausts or chemical plants can directly or indirectly pollute our environment [1]. For example, NO_2 is one of the major air pollutants released from automobile exhausts, because not only is NO_2 harmful to humans, but it is also a major source of acid rain. In order to control the amount of NO_2 released into the atmosphere, sensors for its detection and monitoring become essential. Various sensors are also required to detect explosive gases in chemical plants and laboratories for the prevention of explosions. For the same reason, homes that use natural gas sources require sensors for the detection of any leakage of the gas. Owing to the importance of gas sensors in our daily life, there are many research groups working on gas sensor development [2-5]. Areas of sensor research include: sensing material development, fabrication process development, device complexity development and performance development. These research areas will be discussed separately in the following sections.

There are two main types of sensing materials - organic and inorganic [6, 7]. Among these materials, semiconducting metal oxides have attracted attention because their resistivities are very sensitive to the gas environment [8-11]. Most of the research on metal oxide sensors has centred on ZnO_2, SnO_2 and TiO_2 [3-5, 12-17]. The reasons for this interest are that these materials have been proven to be sensitive to various gases and that there is an established technique for producing them. Generally, the types of sensing elements range from bulk sintered powders to thick or thin films, and these films may have an amorphous, single crystal, or polycrystalline structure. These sensing elements are the basic building blocks for more sophisticated devices, such as integrated sensors [5], sensor arrays [18], field-effect devices [11], and micromachined devices [19]. The increase in the complexity of the sensor devices may lead to the production of intelligent sensors with micro-scale dimensions. Even so, most of these sensor devices lack the specificity, long term stability and reproducibility desired for a commercial sensor.

Although techniques for the preparation of the materials vary from laboratory to laboratory, there are some common methods which were used. In the early days, ball milling and dry sintering techniques were used to prepare the materials [20-28]. Recently, techniques for the preparation of the materials have improved significantly. These new techniques include chemical vapour deposition (CVD), physical vapour deposition (PVD), various sputtering techniques, and the Langmuir-Blodgett technique [20-28]. With the development of the new techniques, an even wider range of metal oxide based semiconductors have been studied or re-investigated [29-32]. In some cases, the materials produced were found to have different physical and electrical properties dependent upon the method of preparation. As a result, materials which were studied a few years ago are currently being re-investigated intensely.

Recently, tungsten oxide based materials have proven to have a high sensitivity to NO_2 and a low cross sensitivity to other gases [33-39]. Even though there are a number of semiconductor metal oxides that respond to NO_2, these sensors all suffer from a lack of specificity. Without specificity, these sensors will not be reliable because of the possibility of producing a false alarm. Various types of tungsten oxide based sensors have been studied, including the nanocrystalline Ti-W oxides [33] and WO_3 thin films [34-39]. The structure of the WO_3 or Ti-W oxide thin films [40, 41] as well as temperature effects on the size of the mixed metal oxide powders has also been studied [40]. However, these studies are still at an early stage and consequently, little is known about reproducibility and long term stability of the sensors. Furthermore, most of these tungsten oxide based materials were produced by complicated methods such as CVD and sputtering [22, 23]. Hence an improvement in the fabrication of tungsten oxide based materials is desirable.

Despite the fact that there have been studies carried out on the sensing mechanism (adsorption/desorption of gas molecules on the surface of the sensor), the detailed mechanism remains unknown [42-44]. Evidence shows that the conductivities of semiconducting metal oxides change when specific gas molecules are adsorbed onto their surfaces. There are two classes of semiconducting materials, n-type and p-type. The conductivity of the n-type materials is usually sensitive to the oxidative nature of a gas whereas the p-type semiconductor is sensitive to the reductive nature of a gas.

After much research, the performance of sensors has improved and the demand for small, inexpensive gas sensors capable of detecting sub-ppm quantities of NO_2 has continued. In this project, our work to overcome some of the limitations of NO_2 sensors based on tungsten and molybdenum oxide is described. By using a room temperature photochemical method of preparation, sensitivity and recovery time of the sensors have been improved.

Since the interpretation of many experimental results in this thesis will be based on some theories, these theories will be described in the following introduction sections. They are the fundamentals of photochemistry, molecular orbital theory and the basis of crystallography. The structure of a material influences some of its key properties, including: electrical, thermal, magnetic, and optical properties. Thus, both the theoretical and experimental aspects for interpretation of the structure a material will be discussed. Electrical conduction in the solid material will be determined by examining its electrical properties at various temperatures. Finally the outline for the thesis will be presented.

1.2 Molecular orbital theory

Molecular orbital theory will be described first, since most of the work in this thesis will be explained in terms of molecular orbitals [45]. The molecular orbitals (MOs) of a molecule are constructed from the atomic orbitals of each of the atoms in the molecule. Atomic orbitals are defined as the allowed states for an electron moving in the field of one nucleus. Figure 1.1 illustrates the two molecular orbitals formed by the 1s orbitals of two hydrogen atoms. One orbital is the σ_{1s} bonding orbital, and the other orbital is the σ^*_{1s} antibonding orbital. Electrons in the bonding orbital have lower energy than those in the parent atomic orbitals. Electrons in the antibonding orbital have higher energy than those in the parent atomic orbitals. The molecular orbitals of a complicated molecule can be constructed in a similar manner. For instance, the molecular orbitals of $M(CO)_6$ are illustrated in Figure 1.2, where M is one of the group VI transition metals. This qualitative molecular orbital diagram is constructed by making symmetry allowed combinations of atomic orbitals from the metal (M) and the σ donor orbitals from the six CO molecules. The resultant molecular orbital diagram consists of σ-bonding orbitals, σ^*-antibonding orbitals and non-bonding orbitals (t_{2g}). The symbol beside each orbital represents its symmetry. In addition to the σ donation of electrons from the carbon to the metal, the metal d-orbitals also donate electrons to the carbonyl groups. The type of overlap involved in this bonding mode is shown in Figure 1.3 and is called π-back-bonding. The molecular orbitals of $M(CO)_6$ can then be constructed to include the π-interaction between the metal and the ligands (see Figure 1.4).

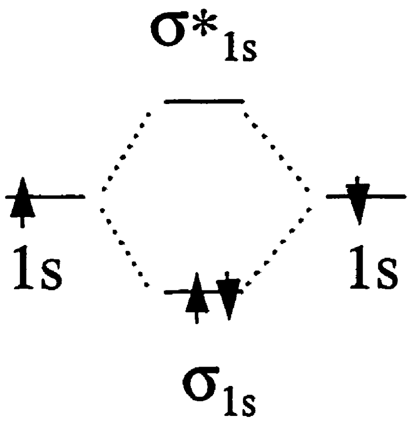

Figure 1.1 Molecular orbitals formed by the 1s orbitals of two hydrogen atoms

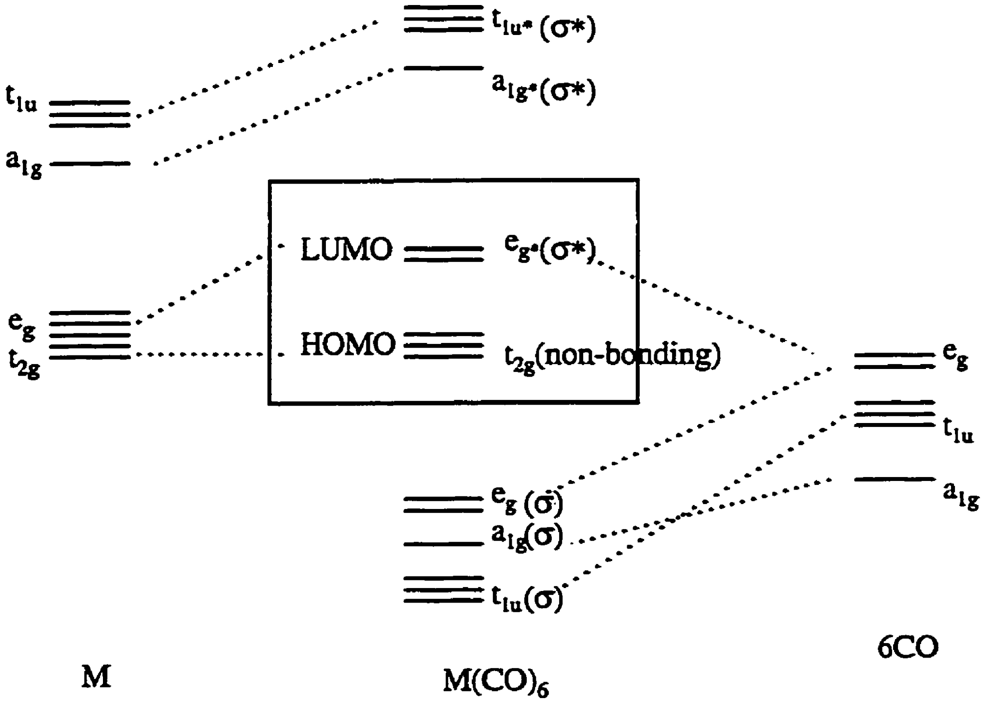

Figure 1.2 Qualitative molecular orbital diagram for M(CO)$_6$, M = Cr, Mo, W

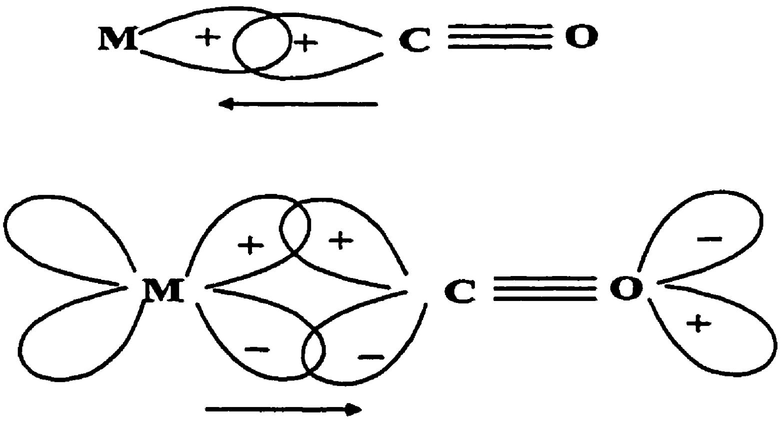

Figure 1.3 A simplified valence bond description of the bonding between the metal and the carbonyl ligands in $M(CO)_6$

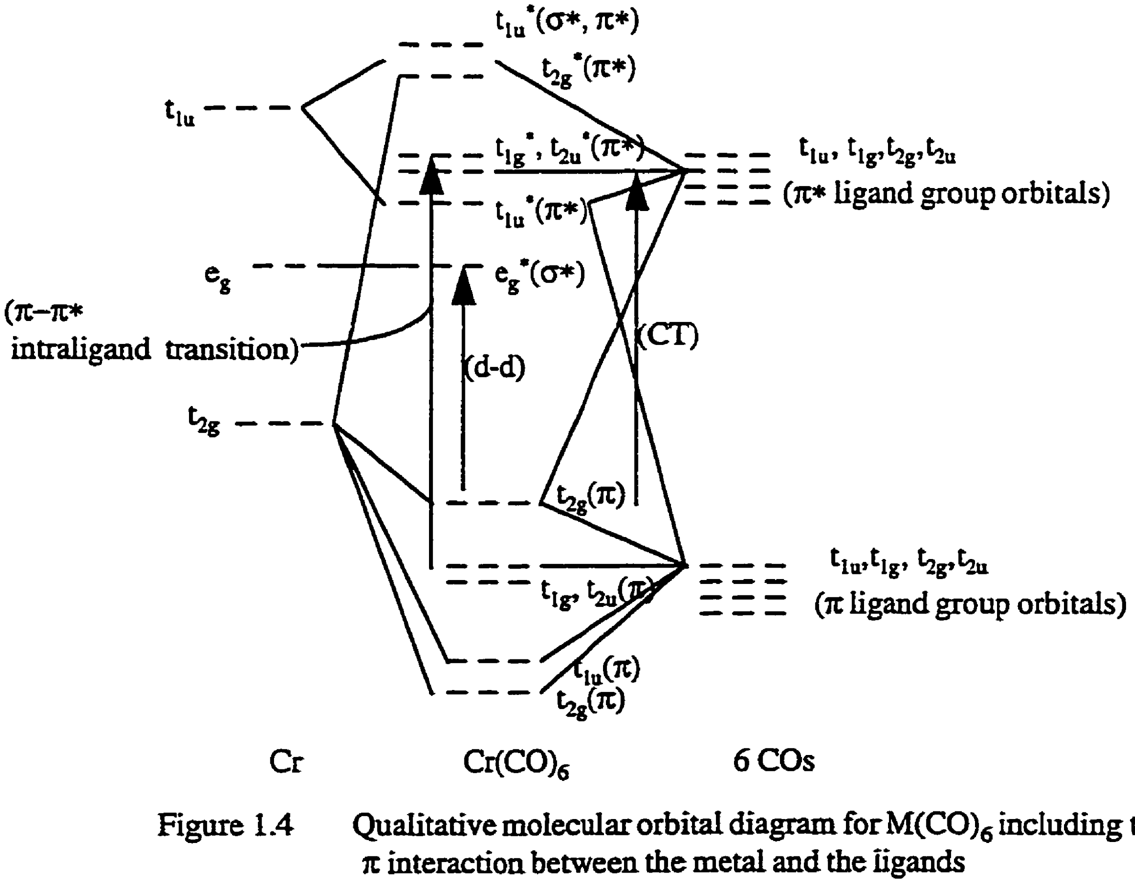

Figure 1.4 Qualitative molecular orbital diagram for $M(CO)_6$ including the π interaction between the metal and the ligands

If the relative energy difference between the metal and the ligands is small, then the perturbation of the σ-bonding orbital will increase. On the other hand, a bigger energy difference between the metals and the ligand orbitals will result a smaller perturbation of the σ orbitals. A more electronegative metal orbital will be closer in energy to the ligand orbitals, thus resulting in a higher energy σ* antibonding orbital. For $M(CO)_6$ complexes where M is one of the group VI transition metals, the HOMO-LUMO gap lies between the t_{2g} (π) orbitals and the e_g^* (σ*) orbitals. The relative energy difference between these two orbitals is crucial to the photochemical reactions of these complexes. The ideal wavelength of light used in a photochemical reaction depends on the relative energy difference of the molecular orbitals. For example, the energy of light selected to perform a photochemical reaction in the $M(CO)_6$ complexes should be equal to or larger than the energy difference between the t_{2g} (π) orbitals and the e_g^* (σ*) orbitals. All the chemical reactions described in this thesis are induced by light, in other words, they are photochemical reactions. Therefore, the general topic of photochemistry will be introduced next.

1.3 Photochemistry

The first law of photochemistry was established by Grotthus and Draper [46-48]. It states: *the only radiations that are effective in inducing photochemical changes are those absorbed by the system.* The second law states: *A molecule in a photochemical reaction*

absorbs one quantum of the radiation that induces the reaction. The general equations for photochemical processes in transition metals can be written as follows:

$ML_n + h\nu \rightarrow ML_n^*$ (1.1)

$ML_n^* \rightarrow \text{energy} + ML_n$ (1.2)

$ML_n^* \rightarrow ML_{n-1} + L$ (1.3)

where M is a transition metal, and L is the ligand. ML_n is a transition metal complex in its ground state. Upon light absorption, ML_n becomes ML_n^* which represents ML_n in the excited state (see Equation 1.1). Once ML_n^* releases energy in the form of heat or light, then the complex returns to the ground state ML_n (see Equation 1.2). Alternatively, ML_n^* can react and generate ML_{n-1} and an uncoordinated ligand L (see equation 1.3). It needs to be pointed out that whether or not these excited states are singlet or triplet would not be identified since it is beyond the scope of this work. In order to determine the photoefficiency of the photochemical reaction, the quantum yields will be calculated. The quantum yield, ϕ, is defined as the number of molecules which undergo a specific reaction for each photon absorbed [46-50]. In this thesis, the quantum yield for the first order photochemical reaction was calculated using Equation 1.4. The derivation of the equation is given in previous publications [51-53].

$$A^t = A^o \exp\left(-2.303 \cdot \phi_l \cdot \varepsilon_\lambda \cdot I_o \cdot t\right) \tag{1.4}$$

In this equation, A^t is the absorbance at the wavelength used to monitor the reaction at time t. A^o is the initial absorbance at the monitoring wavelength. I_o is the incident light intensity at the excitation wavelength, ε_A is the molar extinction coefficient at the excitation wavelength, ϕ_1 is the disappearance quantum yield, and t is the photolysis time. When a H_2 molecule absorbs light, one of the electrons in the σ_{1s} orbital is excited to the upper σ^*_{1s} orbital (see Figure 1.1). The resulting configuration is the first excited state of the molecule. Since the electron in the σ^*_{1s} orbital is higher in energy than what it was in the σ_{1s} orbital, the energy of the molecule is also higher. In order for the H_2 molecule to go from the first excited state to the ground state, the σ^*_{1s} orbital must be depopulated. This depopulation of the σ^*_{1s} orbital will result in either breaking of the bond between the two hydrogen atoms or in energy being released as heat or light. The situation is more complicated if the molecule is a transition metal complex. The electronic transitions which occur in a metal complex can be classified as: metal localised, ligand localised, and charge transfer (CT). Metal localised transitions occur between orbitals localised on the metal are referred to as either d-d or ligand field (LF) transitions. Ligand localised transitions include the σ-σ^*, π-π^* and n-π^* transitions of the coordinated ligands. Charge transfer transitions include the intramolecular charge-transfer transitions: metal to ligand and ligand to metal charge transfer transitions. Representative transitions are shown in Figure 1.4. The transition from a t_{2g} orbital to an e_g^* orbital is a d-d transition, since both the t_{2g} orbitals and the e_g^* orbitals have metal character. The transition between the π ligand group orbitals and the π^* ligand group orbitals is a π-π^* intraligand transition because both orbitals are ligand in character. The transition from the t_{2g} orbital to the t_{1g}^* orbital is a charge transfer transition (CT). Since the energy of each transition is different, in some cases the complexes can be selectively irradiated in order to promote specific transitions.

The excitation into the LF transition often results in the loss of ligands, making it a very powerful tool to induce ligand dissociation. For example, if one of the electrons in the t_{2g} orbitals is excited to a e_g^* orbital, then the bonding between the metal centre and the ligands will be weakened. Since t_{2g} orbitals are mainly metal in character, the depopulation of this orbital may not affect the bonding between the metal centre and the ligands significantly. However, population of σ^* orbitals will result in a weakening of the σ-bonding between the metal and the ligands because the e_g^* (σ^*) orbitals are of antibonding character with respect to the metal-ligand bonds. As a result, one of the ligands is often ejected from the complex.

1.4 Photochemical production of metal and metal oxide films

There has been a great deal of interest in processes which lead to the deposition of thin films of materials owing to the wide range of applications for thin films in electronic devices [20-27]. There are many existing techniques for fabrication of thin films such as, chemical vapour deposition (CVD), vacuum evaporation (VE), ion beam evaporation (IBE) , and molecular beam epitaxy (MBE) [20-27]. However, some of these processes such as CVD must be operated at high temperatures, and others require high or ultra high vacuum systems (VE, IBE, MBE). Since there is usually more than one layer produced on a single electronic device, one disadvantage of the techniques using high temperatures is the damage to the existing layers during the fabrication of a new layer. The disadvantages of the processes requiring high or ultra high vacuum systems are the high cost of the equipment and the time consumed in achieving the vacuum. As a result of the operating conditions, each deposition method imposes strict requirements on the choice of precursors, e.g., volatility and thermal stability. In addition, new processes may have advantages over more established methods and also may provide routes to materials which are not currently accessible. For these reasons, the development of new fabrication procedures is of importance. A room temperature photochemical processes to fabricate thin films will be described [54-56]. The general fabrication sequence for the room temperature deposition method is illustrated in Figure 1.5. The direct deposition process begins by placing a drop of the precursor solution on a spinning substrate. This precursor solution contains the starting material (ML_n) in a volatile solvent, where M is a metal and L is the ligand. An uniform amorphous film is formed upon spin coating. In order to convert the starting materials into metals and free ligands, the film is exposed to UV light for a specified time. Reaction of the photoproduced metal *in situ* with oxygen leads to the production of metal oxides. In this contribution, the process of designing suitable precursor molecules for the production of the metal oxides of chromium, molybdenum and/or tungsten will be described. To be a useful precursor for this method the precursor compound must form kinetically stable amorphous films upon spin coating. In addition, the resultant thin films must be photosensitive, and the photochemical reaction must lead to the desired products. Thus, the first main object in this thesis is the selection of suitable precursor compounds, and the second is the study on the efficiency of the photochemical process.

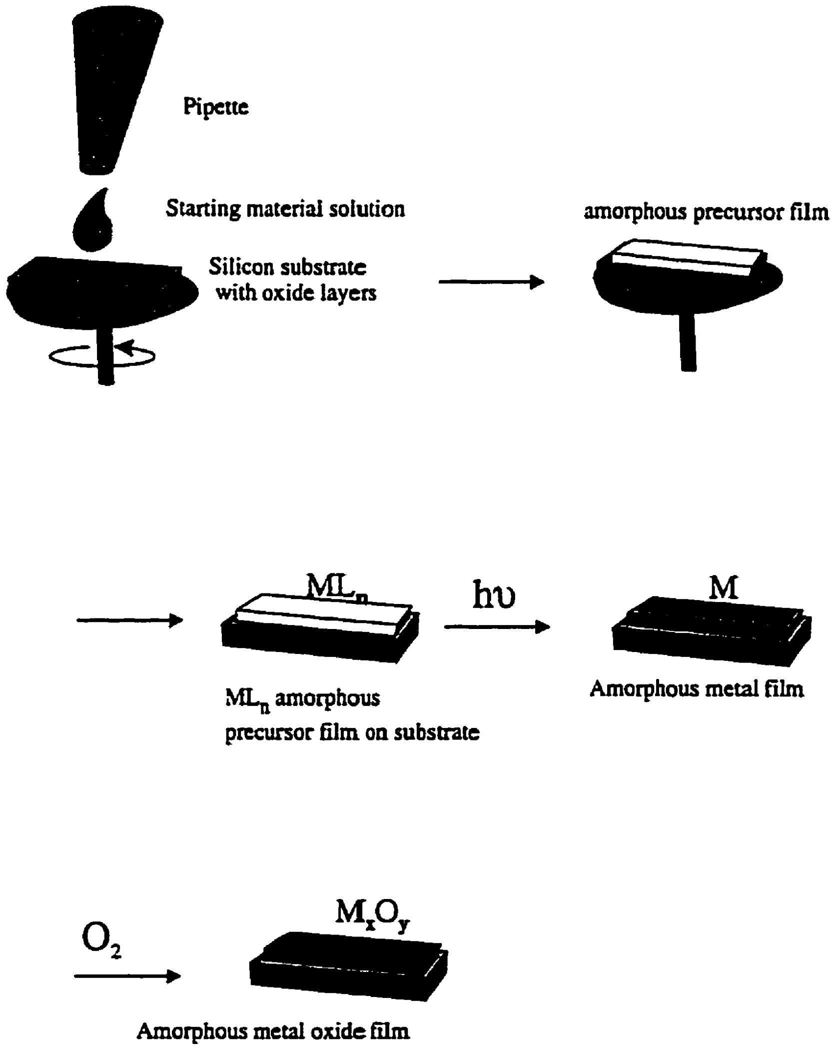

Figure 1.5 Figure illustrating the spin-coating method for making amorphous films and the room temperature photochemical process for the fabrication of thin metal or metal oxide films

1.5 Determination of structures of the material

The properties of a material depend very much upon its crystal structure. It is therefore desirable to identify the basic atomic arrangement in the solid. All crystalline materials are situated in a periodic array over large atomic distances (long range order), whereas an amorphous material has only a short range order [57]. Whether the solid formed is crystalline or amorphous depends on the preparation conditions. The atoms that make up crystals are arranged on a crystallographic lattice [58]. The structure of the material is determined by the unit cell, and its geometry is defined in terms of six lattice parameters (three edge lengths and the three inter-axial angles). In describing crystal structures, it is necessary to identify the crystallographic directions and planes. These directions and planes are specified by three Miller indices. The simplest crystals are those containing one element such as pure metals. Most metal crystals are based on one of the three simple crystal structures: face-centred cubic (FCC), body-centred cubic (BCC), and hexagonal close-packed (HCP). Transition metal oxides crystallise into various types of lattice structures which are often more complex, e.g., the rocksalt structure and the rutile structure. Of prime importance to this thesis is lattice structure of the ReO_3 metal oxide. The ReO_3 structure is constructed by linking ReO_6 octahedra through all vertices (see Figure 1.6). WO_3 adopts the ReO_3 structure with the same band structure but different occupancy [58-60]. (Band structure will be introduced in Section 1.6.) ReO_3 is a conductor because its conduction band is partially filled; however, WO_3 is a semiconductor because its conduction band is empty.

Experimentally, x-ray diffractometry is often used to determine the structure of materials. When a beam of x-rays impinges on a crystal, a diffraction pattern is produced. This is due to the constructive and destructive interference after the x-rays scatter from the crystals. Figure 1.7 shows x-rays of wavelength, λ, scattered from two atomic planes separated by some distance d. The beams will emerge in phase only if they satisfy the Bragg equation :

$$n\lambda = 2d \sin\theta \tag{1.5}$$

where n is an integer, λ is the wavelength of the X-ray, and d is the lattice spacing. The lattice spacing d can be calculated by the diffraction angle 2θ obtained in the XRD spectrum. The structure of the material can therefore be determined. In this thesis, the structure was identified by the X-ray powdered diffraction pattern (XRD) and the known XRD of the known structures of the material.

1.6 The electrical properties of materials

In most cases, the electrical properties of a solid material are a consequence of its electron band structure. A band is defined as a collection of closely spaced molecular orbitals, while a valence band is the bonding set which is completely filled with electrons and a conduction band is an empty antibonding set [25].

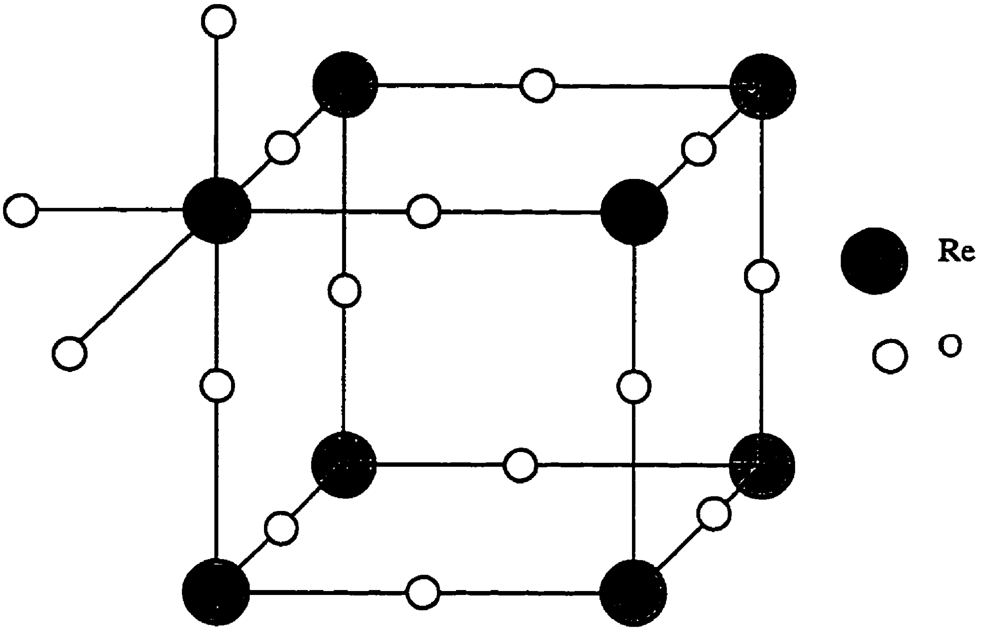

Figure 1.6 The ReO_3 structure

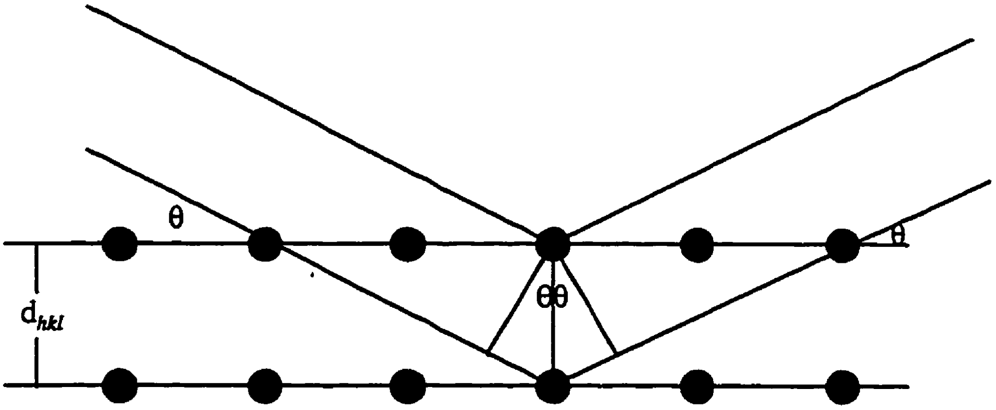

Figure 1.7 Diffraction of x-rays by planes of atoms.

The space between the valence band and the conduction band is called band gap which is analogous to the HOMO-LUMO gap in molecular orbitals. The HOMO-LUMO gap is smaller than the gap in H_2, if the molecular orbitals consist of five bonding and five antibonding orbitals from 10 hydrogen atoms (see Figure 1.8). The greater the number of hydrogen atoms, the more delocalised the molecular orbitals and the smaller the HOMO-LUMO gap. Therefore, the bonding and antibonding orbitals may approach the same energy if enough hydrogen atoms are combined together. With the combination of the bonding and antibonding orbitals of various metal atoms, three basic band structures arise - metal, insulator, and semiconductor. A solid is metallic if either the valence band or the conduction band is partially filled. It is an insulator if any one band is either completely filled or completely empty. The energy gap in a semiconductor is smaller than in an insulator. For this reason, electrons can move to the conduction band by absorbing energy from external sources such as heat or light. As a result, the conductivity of a semiconductor can be increased significantly.

The electrical properties of a material can also be explained as the response of the material to an applied electric field. The current, I, is related to the applied bias, V, by Ohm's law as follows:

$$V = IR \tag{1.6}$$

where R is the resistance of the material through which the current is passing.

The resistivity, ρ, is independent of specimen geometry and can be related to R through the expression:

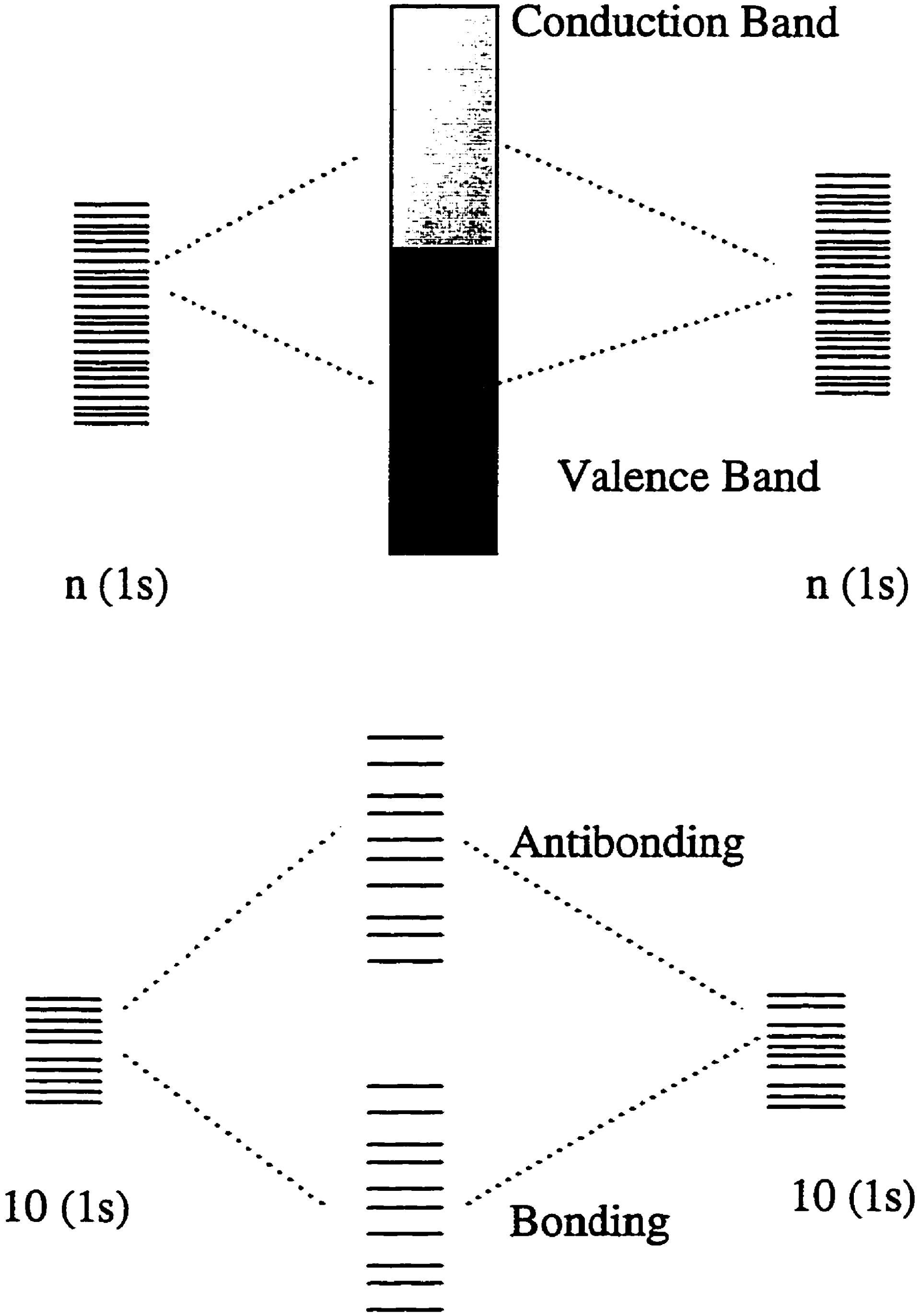

Figure 1.8 Band structure constructed from atomic orbitals

$$\rho = \frac{Z\,V}{I\,\ell} = \frac{RZ}{\ell} \qquad (1.7)$$

where l is the distance between the two points at which the voltage is measured, and Z is the cross-sectional area perpendicular to the direction of the current.

1.7 Research plan outline

There are three nitrogen oxides classified as air pollutants: nitric oxide (NO), nitrogen dioxide (NO_2), and nitrous oxide (N_2O) [61]. These nitrogen oxides were referred to as NO_x [61]. Nitric oxide converted to nitrogen dioxide in the presence of ozone, and nitrogen dioxide converted to nitric oxide by sun light [1].

$$NO_2 \xrightarrow{h\nu} NO + O \qquad (1.8)$$

$$O + O_2 \longrightarrow O_3 \qquad (1.9)$$

$$O_3 + NO \longrightarrow O_2 + NO_2 \qquad (1.10)$$

Therefore, the composition of NOx (the ratio of NO to NO_2) varies with the environment: the intensity of the light, and the presence of ozone. It was also reported that with the presence of reactive hydrocarbons in the air, the reaction mechanism became even more complicate [1]. Since both NO and NO_2 are toxic and they convert to each other in the atmosphere, it is important to detect both compounds in our surroundings at the same time. Therefore, the first main goal of this project was to fabricate sensors which were capable of detecting sub-ppm NO_x. The second goal was to apply the room temperature photochemical process to the fabrication of a chemical sensor in order to provide an alternative route for the process. Chapters 2 and 3 will be devoted to the designing of the starting materials. Chapters 4 and 5 present the fabrication and performance of the sensor devices and suggest a model for the sensing mechanism. In order to produce metals or metal oxides from the room temperature photochemical process, the precursors must satisfy two main requirements. The first is that they should be able to form amorphous films upon spin coating and the second is that they have to be photosensitive. Chapter 2 presents the photochemistry of $M(CO)_5PPh_3$ (M = Cr, Mo, W) as solid films on silicon substrates. A reaction correlation diagram for the photochemical reaction of these complexes is discussed. The differential equations, for a sequential two photon process, were derived for the calculation of the photo-dissociation quantum yields. There are two main problems which arose in Chapter 2. These are the presence of impurities in the resultant film and that the reaction is a two photon process. The impurities in the resultant film indicated that the precursor used in this chapter was not ideal; the two photon process indicated that this photochemical process was not efficient. Hence, the objective of Chapter 3 was to solve these two problems. In Chapter 3, the photochemistry of $M(CO)_4(L\text{-}L)$ (M= Cr (L-L = en, Me_2-en, Et_2-en), Mo (L-L = Me_2-en, Et_2-en), W (L-L = Et_2-en)) as solid films is reported. Their photochemical mechanism is similar and the primary photoreaction is interpreted using a molecular orbital approach. The quantum yields for the photo-dissociation for these complexes were determined. The best candidate to form an amorphous film efficiently will serve as the starting material for the fabrication of sensors as described in the next two chapters.

In Chapter 4, the fabrication and the performance of tungsten oxide sensors for the detection of NO_x is presented. The design of the sensor device as well as the chamber for testing the performance of the sensors is described. The fabrication of the sensor devices is presented. The structural characteristics of both the amorphous and polycrystalline tungsten oxide films are interpreted from XRD and Auger electron spectra. The electrical characterisation of the sensor devices is discussed. Finally, the sensing response of these metal oxide sensors to different concentrations of NO_x at various operating temperatures is reported. Discussed in Chapter 5 is the fabrication of novel amorphous $Mo_{0.05}WO$ and $Mo_{0.09}W_{0.73}O$ thin film sensors. The current-voltage behaviour for these mixed metal oxide devices is reported and their electron transport mechanisms are discussed. Finally the sensitivity of these devices is reported and discussed. A response to sub-ppm NO_x at temperatures ~100°C was shown. In summary, the room temperature photochemical process for fabricating functional devices has been proven to be an alternate approach to sensor construction. This simple and direct deposition process not only eliminates the possibility of damaging other functional layers on a chip, it also has the advantage of fabricating a wide range of materials in a short time period. The sensors fabricated have proven to be sensitive to sub-ppm NO_x concentrations. These sensors have advantages over others in their specificity, reproducibility, and long term stability. The design of the complexes and sensors as well as the testing of the process serves as a guideline for the fabrication of various types of sensors for gas detection. It is thus the goal of the thesis not only to fabricate sensors for NO_x, but also to serve as a guideline for the fabrication of many other types of sensors.

CHAPTER 2

Solid state photochemistry of $M(CO)_5PPh_3$ (M = Cr, Mo, and W)

2.1 Introduction

The goal of this project is to deposit metal oxide films of chromium, molybdenum, and tungsten on a silicon substrate via the room temperature photochemical process described in Chapter 1. In this process, there are two strict requirements which the starting materials must satisfy. The first is that the precursor molecules must be photosensitive, and the second is that they must be able to form amorphous films upon spin coating. Chromium hexacarbonyl is photosensitive in solution, and has been used for the deposition of chromium films by CVD [62-65]. However, because $Cr(CO)_6$ is a highly symmetric complex it is unlikely to form a randomly oriented amorphous film upon spin coating (see Figure 2.1). Instead, it tends to form a crystalline film because of its easily organised lattice. Since the replacement of a CO by a bulky PPh_3 ligand lowers the symmetry of the complex from O_h to C_{4v}, $Cr(CO)_5PPh_3$ was used as the precursor molecule instead of $Cr(CO)_6$. In order to determine whether or not this precursor is a good choice, it is necessary to investigate both ability of the compound to form an amorphous film upon spin coating as well as its photochemistry.

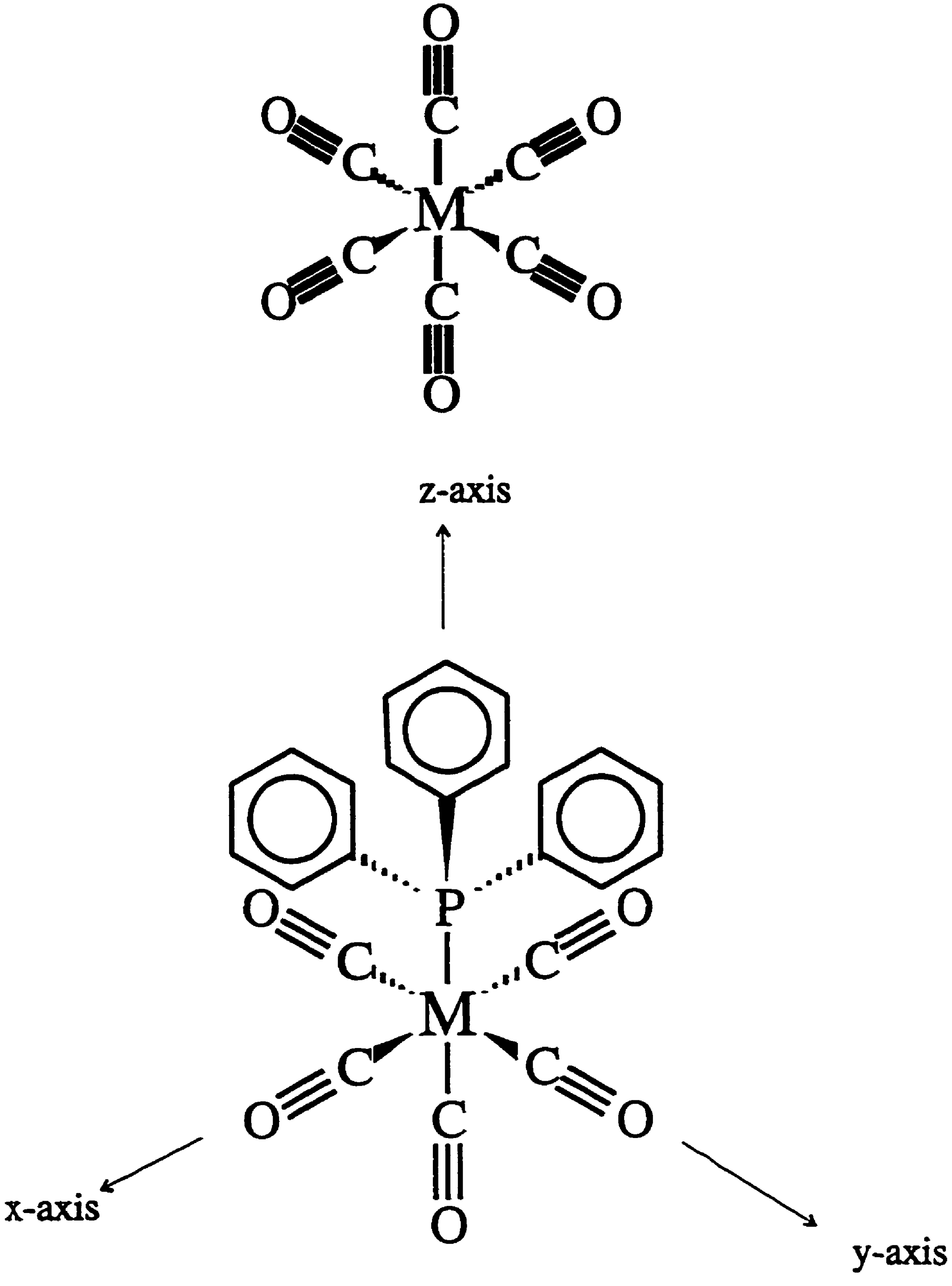

Figure 2.1 The structure of Cr(CO)$_6$, and the definition of the x, y and z axis for Cr(CO)$_5$PPh$_3$

The photochemical reactions of $Cr(CO)_5PPh_3$ as a solid film on a silicon substrate were investigated and will be presented. In addition, a reaction correlation diagram for the photochemical reaction of the chromium complex will be used for the interpretation of its photochemistry. Furthermore, it was found that this complex underwent a sequential two photon process. A kinetic equation for describing a sequential two photon process was derived in order to investigate the photoefficiency of this reaction. In order to produce molybdenum and tungsten oxides, $Mo(CO)_5PPh_3$ and $W(CO)_5PPh_3$ were synthesised. Photochemistry of these two complexes will be presented and compared to that of the chromium complex. Finally, the quality of metal oxide films of chromium, molybdenum, and tungsten deposited from $M(CO)_5PPh_3$ precursors via the room temperature photochemical process will be presented.

2.2 Results and Discussion

2.2.1 Spectroscopy of solid state $M(CO)_5PPh_3$ (M = Cr, Mo, W)

Amorphous films of $Cr(CO)_5PPh_3$ were easily cast on silicon substrates by spin coating from methylene chloride solvent. The FTIR spectral information for this metal complex in solution has been studied and is listed in Table 2.1 [66]. However, the observed frequencies in solid state of the carbonyl stretching vibrations may be different from the reported values in solution. It is therefore important to compare the spectral information in solid films and in solution, since the surroundings which the complexes are in may influence their vibrational frequencies.

Table 2.1 FTIR spectral information for the chromium, molybdenum, and tungsten complexes

Compound	cm^{-1}				Reference
$Cr(CO)_5PPh_3$	2064m	1985w	1931vs, 1917vs	-	a solid film*
Assignments	A_1	B_1	E		
	2066m	1988w	1942vs	-	in CCl_4 [66]
	2070w	1989w	1944vs	(1944vs)	in CCl_4 [67]
Assignments	A_1	B_1	E	A_1	
$Mo(CO)_5PPh_3$	2072m	1900w	1939vs, 1925vs	-	a solid film*
Assignments	A_1	B_1	E		
	2074m	1989w	1951vs	(1951vs)	in THF [68]
	A_1	B_1	E	A_1	
	2074m	1988w	1946vs	-	in CCl_4 [66]
	2075m	1989w	1950vs	(1945vs)	in hexane [69]
	A_1	B_1	E	A_1	
	2078w	1990w	1951vs	(1951vs)	in CCl_4 [67]
	A_1	B_1	E	A_1	
$W(CO)_5PPh_3$	2072m	1980w	1931vs, 1917vs	-	a solid film*
Assignments	A_1	B_1	E		
	(2072m)		(1944vs)	(1944vs)	in cyclohexane [70]
	A_1		E	A_1	
	2075m	1980sh	1938vs		in CCl_4 [66]
	2074w	1981w	1943vs	(1943vs)	in CCl_4 [67]
	A_1	B_1	E	A_1	
Assignments	A'	A'	A''	A'	
$Cr(CO)_4PPh_3$	2012	1900	1888	1825	a solid film*
$Mo(CO)_4PPh_3$	2020	1990	1895	1850	a solid film*
$W(CO)_4PPh_3$	2006	1890	1870	1820	a solid film*

vs = very strong; s = strong; w = weak; m = medium; sh = shoulder. * [this work],

[a] calculated frequencies are listed in parentheses, - band not observed due to more intense E band

The FTIR spectroscopic information for this solid film was recorded and the spectral data is summarised in Table 2.1. The FTIR spectrum in both solution and solid films consists of a band near 2065 cm^{-1}, a weaker band near 1985 cm^{-1} and two intense bands near 1931 cm^{-1} and 1917 cm^{-1}. Theoretically, there are three infrared active CO stretching fundamentals, the two A_1 modes and one E mode for the $Cr(CO)_5PPh_3$ (C_{4v}) complex [66]. However, the weak band at 1985 cm^{-1} was assigned as B_1 mode due to the slight mechanical coupling of the CO stretching vibrations to modes in the PPh_3 group [67]. The coupling enables the B_1 fundamental which would not otherwise be infrared active. As a result, there are four carbonyl stretching fundamentals for the $Cr(CO)_5PPh_3$ complex. Since all three observed bands have been assigned, the lower energy A_1 band was reported to be not observed. However, the position of the lower energy A_1 band was assigned to be at 1944 cm^{-1} on the basis of the force constant calculations [67]. Since there was no calculations performed to determine the band position of the lower energy A1 band in this work, the band position of A_1 fundamental was not assigned. The symmetry coordinates for the CO modes in $Cr(CO)_5PPh_3$ are illustrated in Figure 2.3, where arrows indicate the direction of dipole moments [71]. It can be seen from Figure 2.2 that the intense fundamental, E, is split into two bands. Presumably, the spitting is because of both the solid state effects and the coupling of the CO stretching vibrations to modes in the PPh_3 group. Because the two E bands couple with modes in PPh_3 differently, the E band is no longer degenerate. In solution, this difference is not significant because the ligands can rotate about the M-P bond. Therefore, the E bands are degenerate in solution but not in solid films.

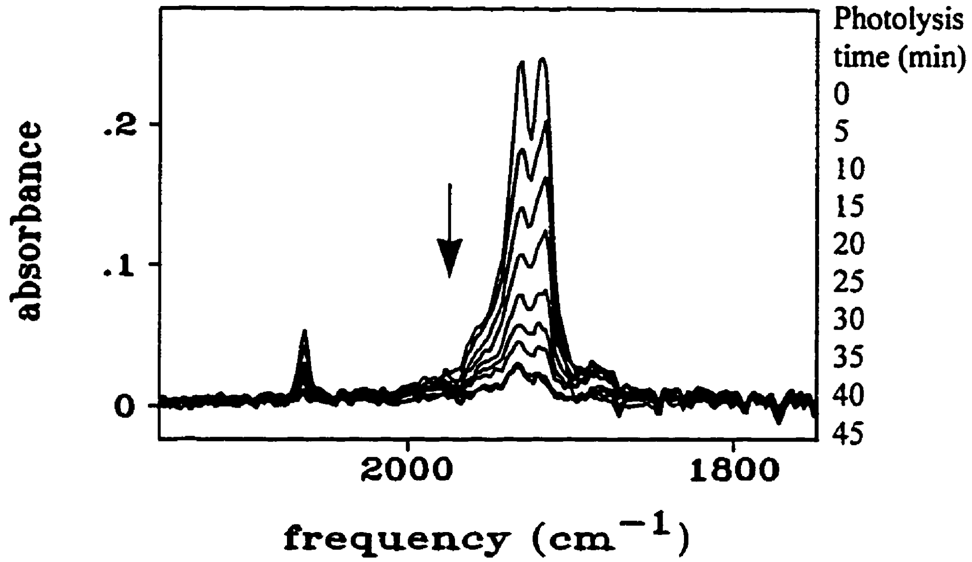

Figure 2.2 FTIR spectra associated with the photolysis of $Cr(CO)_5PPh_3$ as a surface film on silicon substrate at room temperature

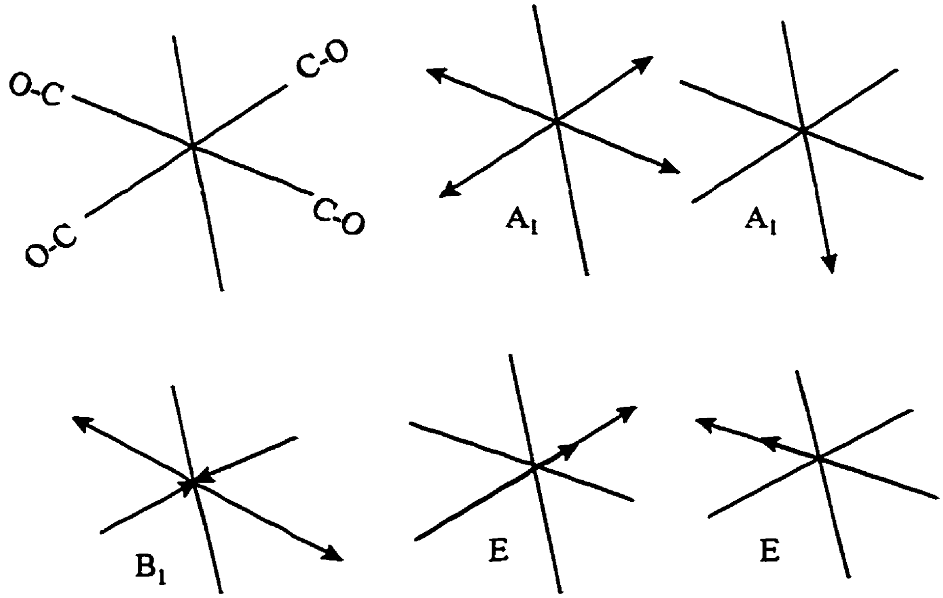

Figure 2.3 CO basis set for carbonyl stretches, and symmetry coordinates for the CO modes in $Cr(CO)_5PPh_3$, where the arrows indicate the direction of dipole moments

All carbonyl stretching fundamentals for the $Cr(CO)_5PPh_3$ in solid state appeared to be approximately at the same frequencies as those in solution. The slight difference between the two vibration energies was assumed to result from the specific interactions in the solid state. Since the chromium complex is surrounded by the solvent molecules in solution and by other chromium complexes in a solid film, the effect of the environment on the energy of the modes may become significant. The investigation was extended to films of $Mo(CO)_5PPh_3$ and $W(CO)_5PPh_3$. The FTIR spectral information of these two complexes in both solution and solid films is summarised in Table 2.1. The general pattern in the FTIR spectra for these two C_{4v} complexes in solution and in solid films is similar to that of the $Cr(CO)_5PPh_3$ (see Figures 2.4 and 2.5) [66 - 69]. These complexes all assumed to have four fundamentals - two A_1 modes, one E mode and one B_1 mode [67 - 69]. The symmetry coordinates for the CO modes in both $Mo(CO)_5PPh_3$ and $W(CO)_5PPh_3$ are the same as $Cr(CO)_5PPh_3$. These CO modes may also be affected by the surroundings in a similar manner. The factors affecting the frequencies of the carbonyl stretching modes are the nature of the metal centre and the ligands [66]. Since these three metal complexes all have the same ligands, their different carbonyl stretching frequencies are a result of the differences in the metal centres. Generally, the larger the electronegativity of the metal, the stronger the ability of the metal to attract electrons. For this reason, the π-back-donation from the metal orbitals to the carbonyls becomes less significant. Since the electronegativity of chromium is smaller than that of molybdenum and tungsten, the carbonyl stretching vibration energy of $Cr(CO)_5PPh_3$ is expected to be smaller than that of $Mo(CO)_5PPh_3$ and $W(CO)_5PPh_3$.

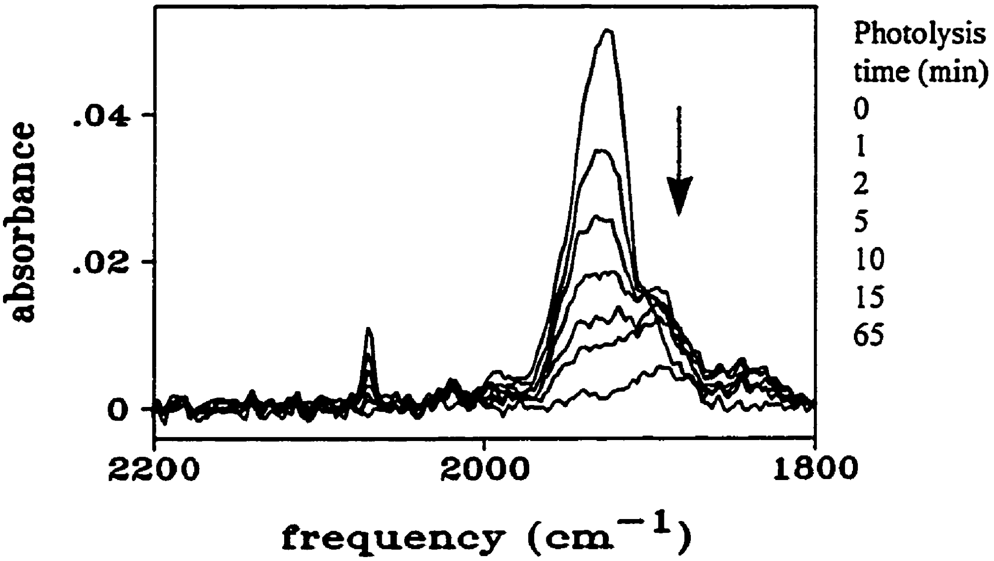

Figure 2.4 FTIR spectra associated withn the photolysis of $Mo(CO)_5PPh_3$ as a surface film on silicon at room temperature.

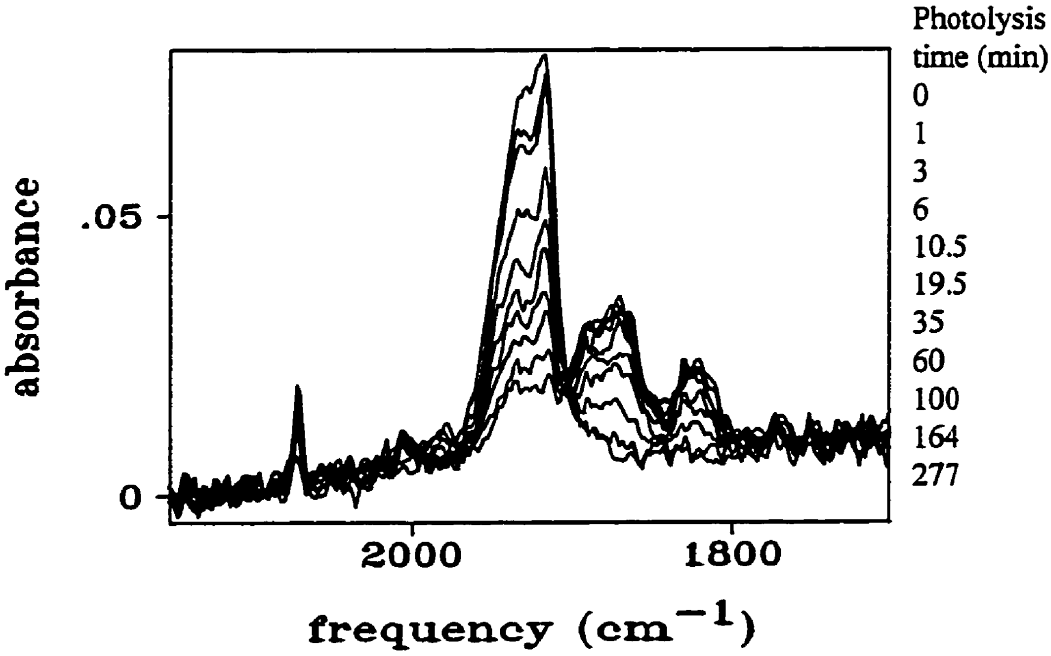

Figure 2.5 FTIR spectra associated with the photolysis of $W(CO)_5PPh_3$ as a surface film on silicon at room temperature

In solid state, the three observed energies of $Cr(CO)_5PPh_3$ were smaller than those of $Mo(CO)_5PPh_3$, which reflected the difference in the electronegativity of these two metals. However, the difference in the observed carbonyl vibration frequencies of $Mo(CO)_5PPh_3$ and $W(CO)_5PPh_3$ was slight. Therefore, there must be some other factors which also influenced the extent of π-back-donation or the carbonyl stretching significantly. For example, the lanthanide contraction on tungsten may lower the ability of the metal to attract electrons [72]. For this reason, the ability of π-back-donation for both molybdenum and tungsten metals may be similar. Therefore, the observed carbonyl vibration frequencies for both metal complexes may appear to be approximately the same. In order to perform an efficient photochemical reaction on these metal complexes, it is necessary to determine electronic spectra of them in solid films. An efficient photochemical process may be achieved by selectively irradiating the metal complexes at energies which corresponding to their electronic transitions. For this reason, electronic spectral assignments for $Cr(CO)_5PPh_3$ in a solid film were recorded and are listed in Table 2.2. The published assignments in solution are also summarised in Table 2.2 [73]. There is only a slight difference in the energy of LF absorptions between the solid films and in solution. Therefore, the lowest energy transition of $Cr(CO)_5PPh_3$ in a solid film was assigned according to the solution assignments as the $^1A_1(e^4b_2^2)$-$^1E(e^3b_2^2a_1^1)$ LF absorption. This LF transition can be achieved by irradiating the complex at 366 nm. The electronic absorptions for $Mo(CO)_5PPh_3$ and $W(CO)_5PPh_3$ in both solid films and solution have also been measured, and the spectral information is summarised in Table 2.2 [68, 74].

Their electronic transitions in solid films have also been assigned according to the corresponding assignments in solution. The lowest energy transition of both $Mo(CO)_5PPh_3$ and $W(CO)_5PPh_3$ in a solid film was assigned as the $^1A_1(e^4b_2^2)$-$^1E(e^3b_2^2a_1^1)$ LF absorption.

Table 2.2 Electronic spectral assignments for $M(CO)_5PPh_3$ (M = Cr, Mo or W)

complex	Absorption band maxima, cm^{-1} [ε, cm^2/mole] (ε, *l*/mole)	Assignment	Reference
$Cr(CO)_5PPh_3$	27,320 [6.5E06]	LF ($^1A_1 \rightarrow {}^1E$)	a solid film [this work]
	27,855 (1.4E03)	LF ($^1A_1 \rightarrow {}^1E$)	in solution [73]
$Mo(CO)_5PPh_3$	27,320 [1.5E06]	LF ($^1A_1 \rightarrow {}^1E$)	a solid film [this work]
	28,990 (~2E03)	LF ($^1A_1 \rightarrow {}^1E$)	in THF [68]
	~32,260[a]		
	32,790 (~6E03)	CT (M →π* CO)	
$W(CO)_5PPh_3$	27,320 [2.1E06]	LF ($^1A_1 \rightarrow {}^1E$)	a solid film [this work]
	27,500 (4E02)	LF ($^1A_1 \rightarrow {}^3E$)	solution [74]
	28,800 (2.2E03)	LF ($^1A_1 \rightarrow {}^1E$)	

[a] Tentative assignment by authors [68]

Therefore, the incident light wavelength chosen for performing the photochemical reaction for these two complexes was also 366 nm. The concentration of the complexes in a solid film was determined by correlating the absorption in UV/VIS spectra to FTIR spectra. The absorbance of $Cr(CO)_5PPh_3$ was plotted against the surface coverage as illustrated in Figure 2.6. The concentration and the absorbance in the UV/VIS spectrum were substituted into Beer's Law in order to calculate the extinction coefficients. These calculated coefficients will be used in a later section for the determination of the quantum yields of the photochemical reaction of $Cr(CO)_5PPh_3$. Similar extinction coefficient calculations were carried out for the molybdenum and the tungsten complexes. Their absorbance/coverage plots are also illustrated in Figure 2.6.

2.2.2 Photochemistry of $M(CO)_5PPh_3$ in a surface film and in a glass (M = Cr, Mo, W)

The photolysis of a thin film of $Cr(CO)_5PPh_3$ was monitored by FTIR spectroscopy at room temperature and the spectra are shown in Figure 2.2. The absorption bands associated with the starting material decrease upon photolysis accompanied by the formation of a broad band centred at 1900 cm^{-1}. Early in the reaction, this band grows in intensity, then reaches a maximum before finally decaying. By subtracting the spectrum of the starting complex from the one obtained during photolysis, the spectrum of this intermediate can be obtained (see Figure 2.7 and Table 2.1).

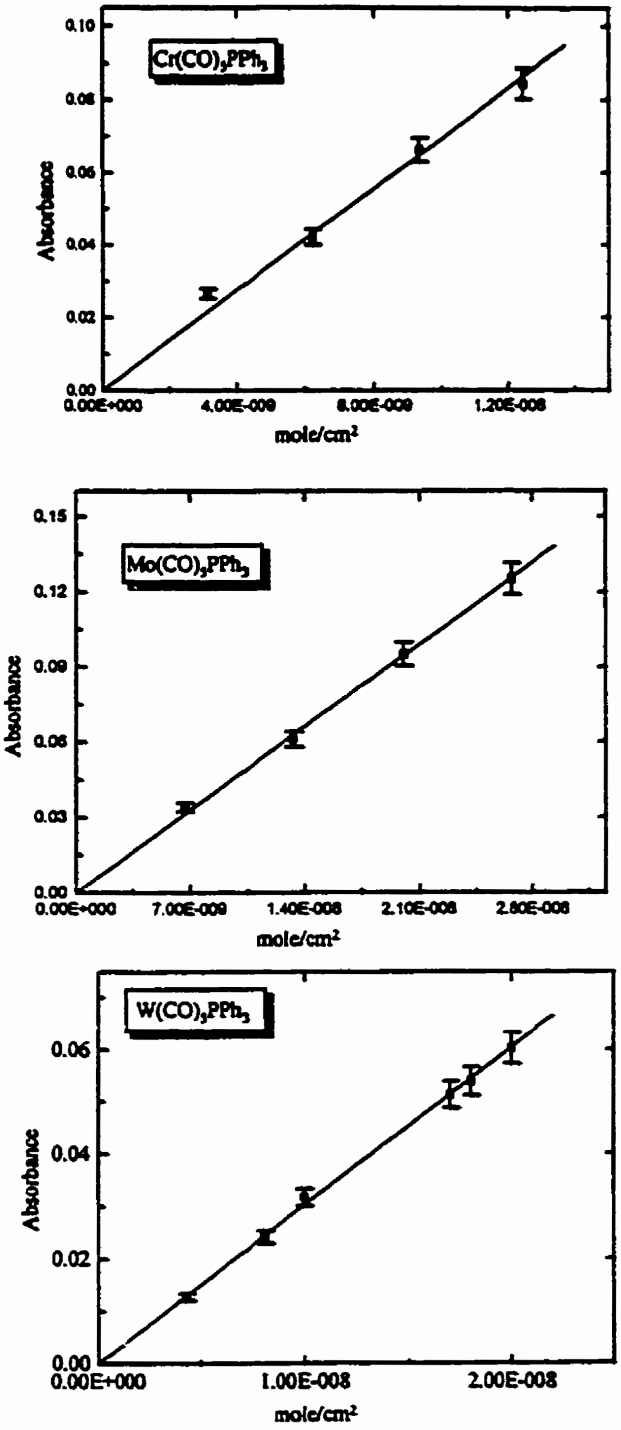

Figure 2.6 absorbance/surface coverage plots for $Cr(CO)_5PPh_3$, $Mo(CO)_5PPh_3$, and $W(CO)_5PPh_3$

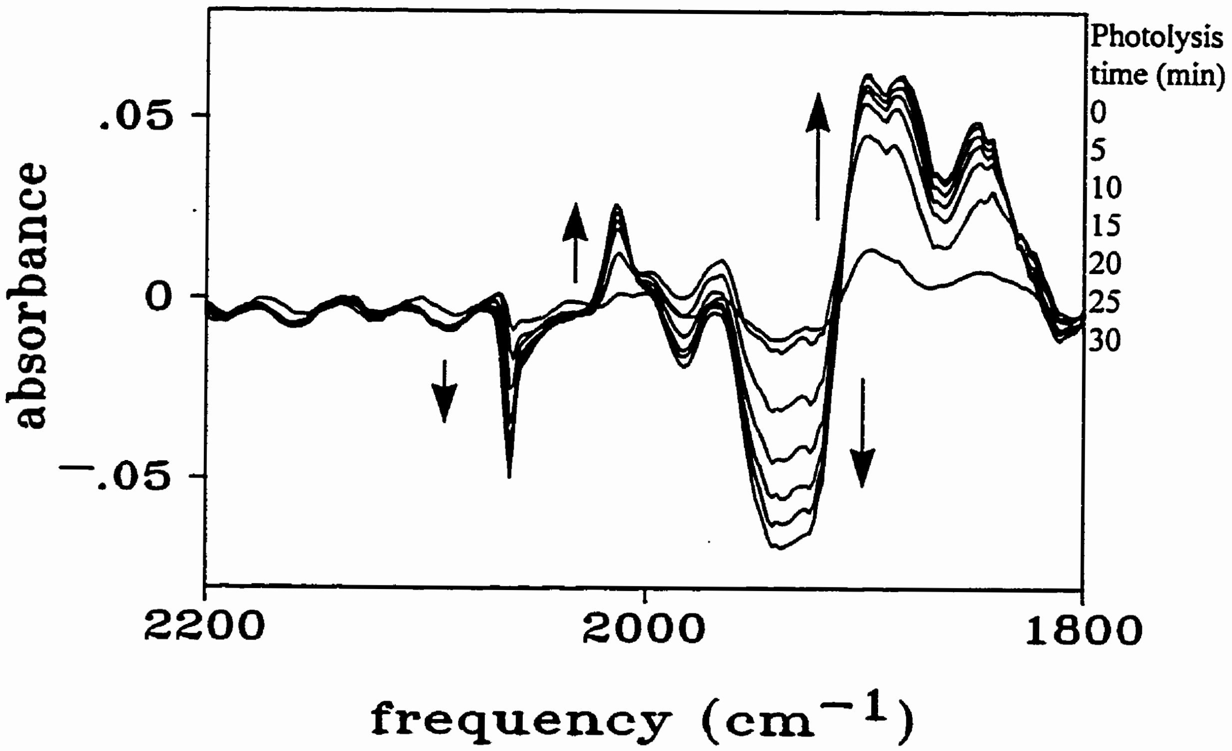

Figure 2.7 FTIR spectral changes associated with the photolysis of $Cr(CO)_5PPh_3$ showing the intermediate absorption bands

This intermediate was observed to be coloured yellow. The most probable intermediate associated with these four CO stretching fundamentals FTIR band which grows in after photolysis was assumed to be $Cr(CO)_4PPh_3$. In order to interpret the photochemical reactions of $Cr(CO)_5PPh_3$, a reaction correlation diagram is illustrated in Figure 2.8. The first molecular orbital diagram represents the d-orbital region of the $Cr(CO)_5PPh_3$ (C_{4v}) molecule in the ground state with one e orbital, one a_1 orbital, one b_1 orbital and one b_2 orbital. Both e and b_2 orbitals are completely filled because Cr(0) has six d electrons. The d-d transitions are expected to be associated with transitions from one of the filled levels into either the b_1 or the a_1 orbital. This will result in the loss of one of the CO's in order to lower the energy of the molecule. There are two CO ligands that could be ejected - the equatorial CO associated with the dx^2-y^2 orbital, and the axial CO associated with the dz^2 orbital. In both cases, a 5-coordinate complex is formed after this one photon process. Further photolysis results in the loss of the remaining ligands, and leaves the metal centres on the substrate. If the ejected CO is at the equatorial position, then there are a few possible symmetries of this 5-coordinate complex (see Figure 2.9). The first possible symmetry of the molecule is Cs, with three CO's at the equatorial positions occupying three of the corners of a square (as before the CO loss). The carbonyl stretching vibrations are expected to be one A'' mode and three A' modes. If the three equatorial CO's rearrange themselves into a triangular plane, then the symmetry is C_{3v}, with one E and two A_1 modes. The third case is if the axial CO joins the equatorial square plane; it then becomes C_{4v} symmetry with one A_1 and one E mode.

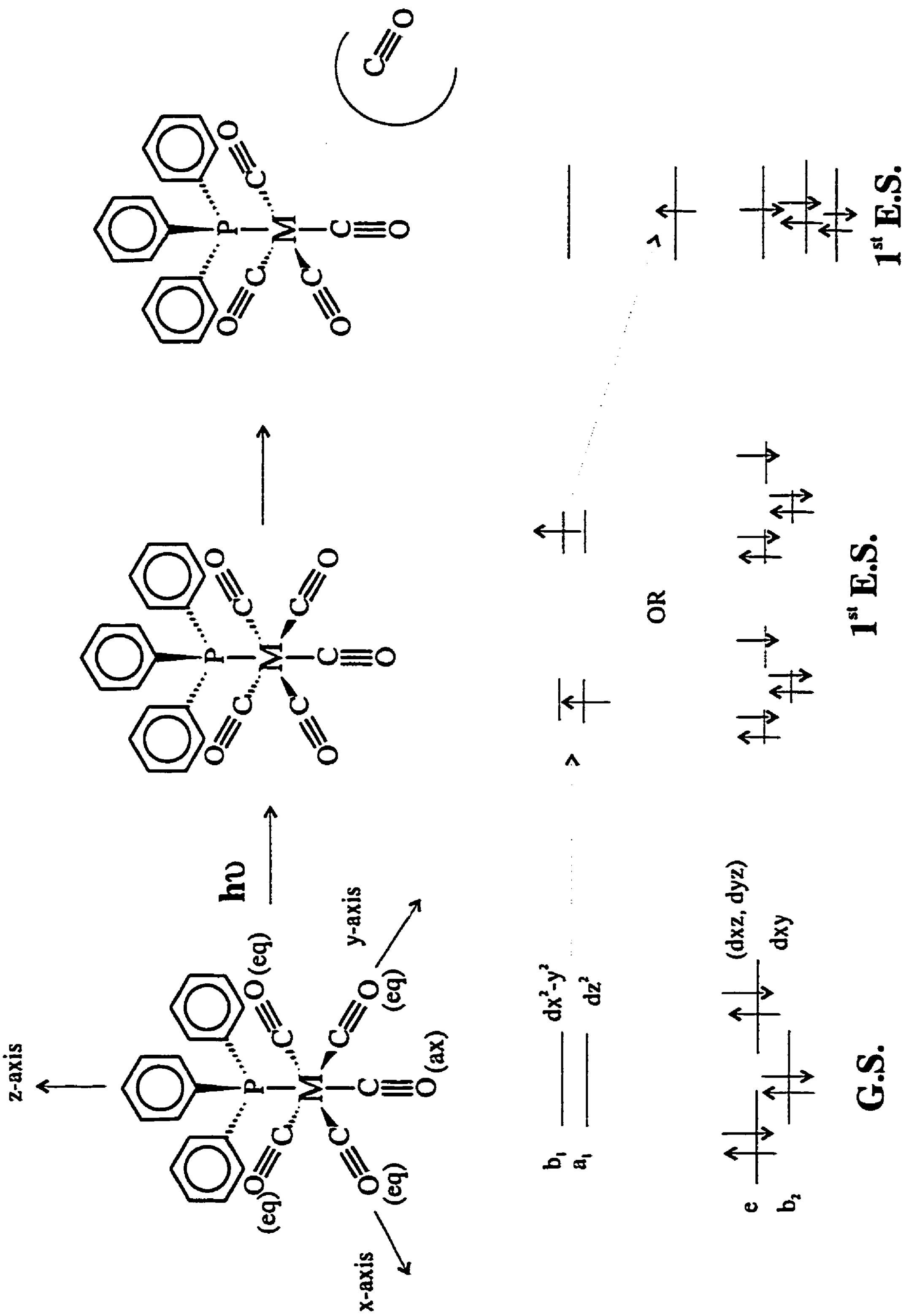

Figure 2.8 Reaction correlation diagram for the photochemical reaction of $Cr(CO)_5PPh_3$, where (eq) = equatorial and (ax) = axial

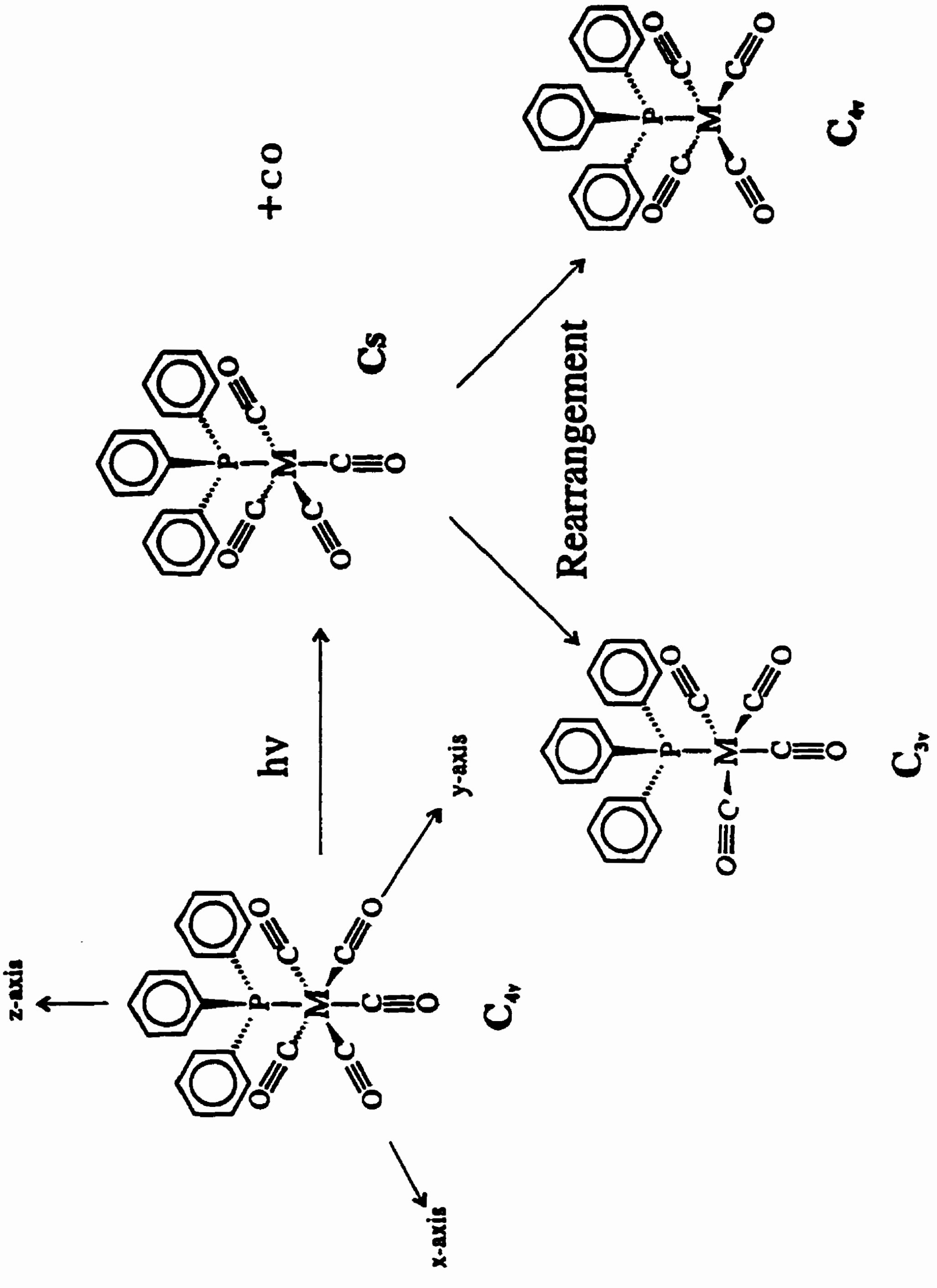

Figure 2.9 Possible structures of the 5-coordinated unsaturated complex after a one photon reaction

In order to determine the proper symmetry for this 5-coordinate intermediate, the FTIR spectrum of it is re-examined (see Figure 2.7). In the spectrum, there are four peaks associated with the complex indicating that there are four carbonyl stretching modes. The symmetry of this complex is not C_{4v} because there should only be two peaks associated with this symmetry. The possibility of having a C_{3v} geometry is eliminated for the same reason. Thus, the intermediate has a Cs symmetry with four CO vibration frequencies [70, 75]. The generation of a coordinatively unsaturated complex has been confirmed by the irradiation of the starting material in a 1,2-epoxyethyl-benzene glass at 77 K. The FTIR spectra provided evidence of the formation of CO at 2143 cm^{-1}[76].

Further photolysis results in the loss of all the carbonyl stretches including the bands associated with the intermediate at both temperatures. Thus, the reactions may be summarised as follows.

$$Cr(CO)_5PPh_3 \xrightarrow{h\nu} Cr(CO)_4PPh_3 + CO \xrightarrow{h\nu} Cr + 5\,CO + PPh_3 \qquad (2.2.1)$$

The photochemistry of films of $Mo(CO)_5PPh_3$ and $W(CO)_5PPh_3$ has also been monitored in a similar manner to films of $Cr(CO)_5PPh_3$. The spectral changes associated with the photolysis of these two complexes are shown in Figures 2.4 and 2.5. Both photolysis resulted in the formation of an intermediate which was also photosensitive and reacted upon further irradiation. Their spectral information is reported in Table 2.1. The photochemical process as well as the symmetry considerations are similar to that described for $Cr(CO)_5PPh_3$. Thus, the same reaction mechanism as delineated for the chromium complex in Equation 2.2.1 may be assumed to apply to the molybdenum and tungsten compounds. Equation 2.2.1 is therefore re-written into a more general form:

$$M(CO)_5(PPh_3) \xrightarrow{h\nu} M(CO)_4(PPh_3) + CO \xrightarrow{h\nu} M + 5\,CO + PPh_3 \qquad (2.2.2)$$

where M = Cr, Mo and W.

2 2.3 Auger Analysis of the film photoproduced from $M(CO)_5PPh_3$, M= Cr, Mo, W

The composition of the film produced by photolysis of $Cr(CO)_5PPh_3$ was analysed by Auger spectrometry (see Table 2.3). The film consisted of chromium (~20 %), oxygen (~6 %), phosphorus (2 %), and carbon (~70 %). The presence of phosphorus indicated that not all of the PPh_3 from the precursors diffused out of the film after photolysis. It was less likely to conclude whether PPh_3 stayed in the final film as PPh_3 or as the intermediate $M(CO)_4PPh_3$ with the available experimental results at this point. The analysis results for $Mo(CO)_5PPh_3$ and $W(CO)_5PPh_3$ are also summarised in Table 2.3. In addition to molybdenum or tungsten in the film, there are oxygen, phosphorus and carbon atoms in it. Because of the prevalent carbon and phosphorus contamination, the calculated composition for all three films can only serve as a qualitative result. The accurate composition of the metal oxide films can only be determined when the amount of impurities in the product films is not significant. In addition, because these impurities would affect the performance of thin film devices, the contamination must be reduced before these films can be used in applications.

Table 2.3 **Auger analysis result for the product film of $M(CO)_5PPh_3$ (M = Cr, Mo, W)**

Precursor	Sputtering time (sec.)	%P	%C	%M	%O	Composition
$Cr(CO)_5PPh_3$	0	1.88	69.89	22.43	5.80	$Cr_{3.9\pm0.3}O$
	10	1.35	71.52	21.19	5.93	$Cr_{3.6\pm0.3}O$
	20	1.33	70.48	20.88	7.31	$Cr_{2.9\pm0.2}O$
	30	2.28	70.40	20.86	6.47	$Cr_{3.2\pm0.2}O$
$Mo(CO)_5PPh_3$	0	3.17	72.71	6.20	17.92	$Mo_{0.35\pm0.03}O$
	10	3.14	74.17	6.13	16.56	$Mo_{0.37\pm0.03}O$
	30	3.09	75.37	5.67	15.87	$Mo_{0.36\pm0.03}O$
	60	4.29	74.79	5.62	15.30	$Mo_{0.37\pm0.03}O$
$W(CO)_5PPh_3$	0	4.1	54.7	12.2	29.0	$W_{0.42\pm0.03}O$
	5	6.0	51.2	15.6	27.1	$W_{0.58\pm0.04}O$
	15	7.4	50.5	15.4	26.7	$W_{0.58\pm0.04}O$

2.2.4 The kinetic equations for a sequential two photon process

As indicated in Equation 2.2.2., the $M(CO)_5PPh_3$ (M = Cr, Mo, W) complexes undergo a two photon process. In order to calculate the quantum yields, a differential equation describing a two photon process was derived.

The absorbance of a sample is related to the light absorbed by Equation 2.1.

$$A = \log\frac{I_o}{I_T} = \log\frac{I_o}{I_o - I_A} \tag{2.1}$$

where A is the absorbance, $\mathbf{I_o}$ is the intensity of the monochromatic light entering the sample, $\mathbf{I_T}$ is the intensity of this light emerging from the sample, and $\mathbf{I_A}$ is the light absorbed by the sample. Equation 2.1 can be rearranged to :

$$10^A = \frac{I_o}{I_o - I_A} \tag{2.2}$$

Thus,

$$I_A = \left(1 - 10^{-A}\right) I_o \tag{2.3}$$

We then assume a one photon reaction, where starting material, S, goes to products, P:

$$S \xrightarrow{h\nu} P$$

The absorbance of the sample at time t, A(*t*), is related to the final absorbance, A(*f*), and the initial absorbance, A(0), through the mole fraction of S, *x*, as shown in Equation 2.4.

$$A(t) = x[A(0) - A(f)] + A(f) \tag{2.4}$$

At any point in time, the absorbance due to the starting material, A^s, and product, A^P, are given by Equations 2.5 and 2.6.

$$A^S = xA(0) \tag{2.5}$$

$$A^P = (1 - x)A(f) \tag{2.6}$$

By combining Equation 2.3 and 2,4, the equation for the light absorbed by the starting materials is obtained.

$$\frac{\partial(h\nu)}{\partial t}=\left[\frac{xA(0)}{xA(0)+(1-x)A(f)}\right]\cdot\left[1-10^{-A(t)}\right]I_o \tag{2.7}$$

Where $$A(t)=xA(0)+(1-x)A(f) \tag{2.8}$$

An approximation for simplifying Equation 2.8 is made (see reference 52)

$$1-10^{-(xA(0)+(1-x)A(f))}=2.303\cdot\left[xA(0)+(1-x)A(f)\right] \tag{2.9}$$

Upon substitution of Equation 2.9 into Equation 2.7 we have

$$\frac{\partial(h\nu)}{\partial t}=2.303\cdot xA(0)I_o \tag{2.10}$$

which can also be written as

$$\frac{\partial(h\nu)}{\partial t}=2.303\cdot\varepsilon_A[S]I_o \tag{2.11}$$

where ε_A is the extinction coefficient at the excitation wavelength in the UV/VIS spectrum and [S] is the concentration of the absorbing species.

If the starting material, S, reacted to form an photosensitive intermediate, B, then the reaction equation would need to be re-written as follows:

$$S \xrightarrow{hv} B \xrightarrow{hv} P$$

Using the same derivation and approximation, the equation for the light absorbed by the intermediate can be written as follows:

$$\frac{\partial(h\upsilon^{B})}{\partial t} = 2.303 \cdot \varepsilon_{B}[B]I_{o} \tag{2.12}$$

where ε_B is the extinction coefficient of B at the excitation wavelength in the UV/VIS spectrum.

The quantum yield ϕ_1 of the starting material, S, can be defined as:

$$\frac{\partial[S]}{\partial t} = -\phi_1 \cdot \frac{\partial h\upsilon^{S}}{\partial t} \tag{2.13}$$

while the quantum yield ϕ_2 of the intermediate is defined in

$$\frac{\partial[B]}{\partial t} = -\phi_2 \cdot \frac{\partial h\upsilon^{B}}{\partial t} + \phi_1 \cdot \frac{\partial h\upsilon^{S}}{\partial t} \tag{2.14}$$

Combining Equation 2.13 with 2.11, we obtain

$$\frac{\partial[S]}{\partial t} = -2.303 \cdot \varepsilon_A \cdot [S] \cdot I_o \cdot \phi_1 \tag{2.15}$$

The following equation can be derived by integrating the concentration of the starting material, S, over time 0 to t.

$$[S] = [S_o] \cdot EXP(-2.303 \cdot \phi_1 \cdot \varepsilon_A \cdot I_o \cdot t) \tag{2.16}$$

where [So] is the initial concentration of the starting material S.

Substituting Equations 2.12, 2.13, and 2.16 into Equation 2.14, we then obtain

$$\frac{\partial[B]}{\partial t} = -2.303\cdot\phi_2\cdot[B]\cdot\varepsilon_B\cdot I_o$$
$$+2.303\cdot\phi_1\cdot\varepsilon_A\cdot I_o\cdot[S_o]\cdot e^{-2.303\cdot\phi_1\cdot\varepsilon_A\cdot I_o\cdot t} \tag{2.17}$$

The above equation can then be re-written for simplification as seen below:

$$\frac{\partial[B]}{\partial t} = -C_2[B]+C_1\cdot[S_o]\cdot EXP(-C_1\cdot t) \tag{2.18}$$

where

$$C_1 = 2.303\cdot\phi_1\cdot\varepsilon_A\cdot I_o \tag{2.19}$$

and

$$C_2 = 2.303\cdot\phi_2\cdot\varepsilon_B\cdot I_o \tag{2.20}$$

Rearranging the equation (2.18), we get:

$$\frac{\partial[B]}{\partial t} + C_2\cdot[B] = C_1\cdot[S_o]\cdot EXP(-C_1\cdot t) \tag{2.21}$$

$[B]$ can then be solved:

$$[B] = \frac{C_1[S_o]}{C_2-C_1}\cdot e^{-C_1\cdot t} + \frac{C_1[S_o]}{C_1-C_2}\cdot e^{-C_2\cdot t} \tag{2.22}$$

Upon substitution of equations 2.19 and 2.20 into 2.22, we then obtain

$$[B]=\frac{\phi_1\cdot\varepsilon_A\cdot[S_o]}{\phi_2\cdot\varepsilon_B-\phi_1\cdot\varepsilon_A}\cdot EXP(-2.303\cdot\phi_1\cdot\varepsilon_A\cdot I_o\cdot t)$$

$$-\frac{\phi_1\cdot\varepsilon_A\cdot[S_o]}{\phi_2\cdot\varepsilon_B-\phi_1\cdot\varepsilon_A}\cdot EXP(-2.303\cdot\phi_2\cdot\varepsilon_B\cdot I_o\cdot t)$$

(2.23)

The absorbance (A^t) at the monitoring wavelength from the IR spectra is due to both the starting material (S), and the intermediate (B). Thus, another equation can be written to relate the relationship between S, B and A^t as follows.

$$A^t=\varepsilon_a\cdot[S]+\varepsilon_b\cdot[B] \tag{2.24}$$

Where ε_a is the extinction coefficient of S, and ε_b is the extinction coefficient of B, and the lower case a and b denote the monitoring wavelength. Equation 2.16 and 2.23 can then be substituted into Equation 2.24 to obtain:

$$A^t=\varepsilon_a\cdot[S_o]\cdot EXP(-2.303\cdot\phi_1\cdot\varepsilon_A\cdot I_o\cdot t)$$

$$+\frac{\varepsilon_b\cdot\phi_1\cdot\varepsilon_A\cdot[S_o]}{\phi_2\cdot\varepsilon_B-\phi_1\cdot\varepsilon_A}\cdot EXP(-2.303\cdot\phi_1\cdot\varepsilon_A\cdot I_o\cdot t)$$

$$-\frac{\varepsilon_b\phi_1\cdot\varepsilon_A\cdot[S_o]}{\phi_2\cdot\varepsilon_B-\phi_1\cdot\varepsilon_A}\cdot EXP(-2.303\cdot\phi_2\cdot\varepsilon_B\cdot I_o\cdot t)$$

(2.25)

Since at time zero, $A^t=A^o=\varepsilon_a\cdot[S_o]$, (2.26)

Equation 2.25 can be re-written as:

$$\frac{A^t}{A^0} = \left(1 + \frac{\varepsilon_b \cdot \phi_1 \cdot \varepsilon_A}{\varepsilon_a(\phi_2 \cdot \varepsilon_B - \phi_1 \cdot \varepsilon_A)}\right) \cdot EXP(-2.303 \cdot \phi_1 \cdot \varepsilon_A \cdot I_o \cdot t)$$

$$- \frac{\varepsilon_b \phi_1 \cdot \varepsilon_A}{\varepsilon_a(\phi_2 \cdot \varepsilon_B - \phi_1 \cdot \varepsilon_A)} \cdot EXP(-2.303 \cdot \phi_2 \cdot \varepsilon_B \cdot I_o \cdot t)$$

(2.27)

where A^t is the absorbance at time t and A^o is the absorbance at time 0.

2.2.5 Quantum Yields for $Cr(CO)_5PPh_3$

Quantum yield measurements were conducted by irradiating the complex on a silicon substrate with UV light of $\lambda = 366$ nm wavelength. Plots of A^t/A^o versus the photolysis time were made, where A^t is the absorbance in the FTIR spectra at time t, and A^o is the absorbance at time zero. Some information from the photolysis experiment was required for Equation 2.27 and this data is listed in Table 2.4. For example, the wavelength of light used for the irradiation was 366 nm, and incident light was found to have an intensity of 2.73 mW/cm^2 and a calculated power (Io) 8.35 x 10^{-9} mole/s cm^2. The extinction coefficient (ε_A) of the starting material, $Cr(CO)_5PPh_3$, was also measured at 366 nm. It was found to be 6.5 x 10^6 mol^{-1} cm^2. The extinction coefficient at 1931 cm^{-1} (ε_a) was measured to be 6.8 x 10^6 mol^{-1}cm^2.

In order to obtain the quantum yield for the first photo-dissociation reaction, an iterative least-squares fit of the absorbance-irradiation time data (A^t/A^o vs. time) was performed. The absorbance, A^t and A^o, at 1931 cm^{-1} was chosen for the calculation because it is the most intense band and therefore gives the biggest signal to noise ratio. Since thicker films of $Cr(CO)_5PPh_3$ have larger values of the absorbance at 1931 cm^{-1} and vise versa, Quantum yields for different thicknesses of $Cr(CO)_5PPh_3$ films have been calculated according to the absorbance at 1931 cm^{-1}. The fitted graphs are illustrated in Figure 2.10, and the quantum yields are reported in Table 2.4. The calculated quantum yields for different film thicknesses were found to be approximately the same. In other words, they are independent of the thickness of the film.

Table 2.4 Quantum yields and fitting parameters for $M(CO)_5PPh_3$ irradiated at 366 nm, where M = Cr, Mo, W.

Metal	Absorbance (1931 cm^{-1})	Φ_1±error	χ^2
Cr	0.296	0.037±0.001	0.00011
	0.199	0.039±0.004	0.00024
	0.086	0.042±0.002	0.00121
	0.050	0.046±0.002	0.00017
	0.035	0.048±0.001	0.00063
Mo	1925 cm^{-1}		
	0.24	0.19±0.01	0.000029
	0.1605	0.20±0.01	0.000033
	0.077	0.23±0.02	0.000049
	0.051	0.29±0.03	0.000602
W	1917 cm^{-1}		
	0.41	0.36±0.03	0.00049
	0.345	0.41±0.03	0.00005
	0.1275	0.40±0.05	0.00179
	0.0676	0.40±0.05	0.00100
	0.033	0.42±0.03	0.00033

χ^2: correlation coefficient

Table 2.4 (continued)

Metal	Absorbance (1931 cm^{-1})	Io (s cm^2 $mole^{-1}$)	ε_A (cm^2 $mole^{-1}$)	ε_a (cm^2 $mole^{-1}$)
Cr	0.296			
	0.199	8.4 x 10^{-9}	6.5 x 10^6	6.8 x 10^6
	0.086			
	0.050			
	0.035			
Mo	1925 cm^{-1}			
	0.24			
	0.1605	7.7 x $^{-9}$	1.5 x 10^6	4.6 x 10^6
	0.077			
	0.051			
W	1917 cm^{-1}			
	0.41	8.3 x 10^{-10}	2.1 x 10^6	3.1 x 10^6
	0.345	8.3 x 10^{-10}		
	0.1275	8.3 x 10^{-10}		
	0.0676	8.3 x 10^{-10}		
	0.033	9.6 x 10^{-9}		

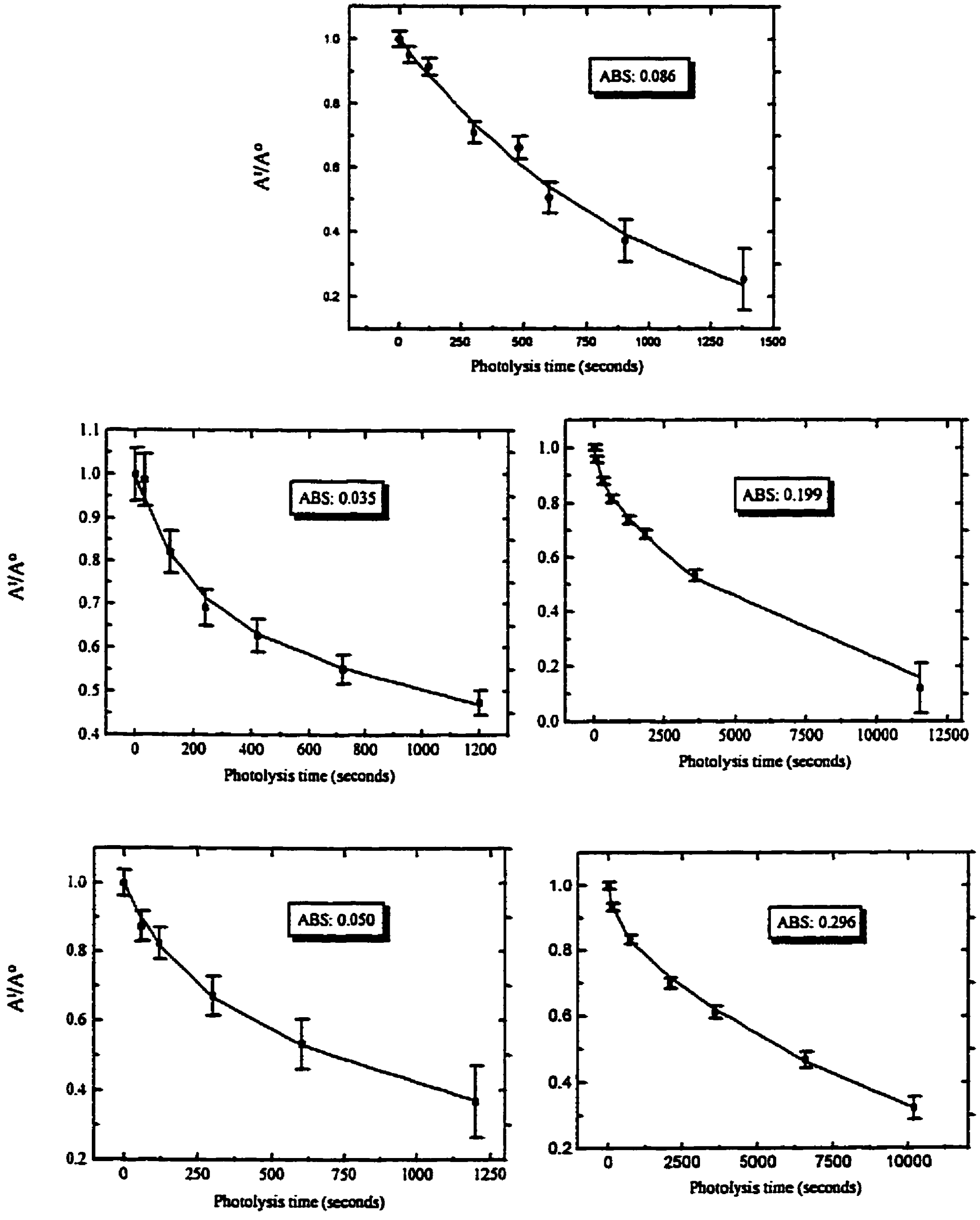

Figure 2.10 Plots of A^t/A^o vs. photolysis time of $Cr(CO)_5PPh_3$ (ABS = absorbance at 1931 cm^{-1})

2.2.6 The quantum yield calculations for the photochemistry of $Mo(CO)_5PPh_3$ and $W(CO)_5PPh_3$ and the discussion for $M(CO)_5PPh_3$ (M = Cr, Mo, W)

The quantum yields for $Mo(CO)_5PPh_3$ and $W(CO)_5PPh_3$ were calculated in a similar manner to those for $Cr(CO)_5PPh_3$. The parameters used for the quantum yield calculations are listed in Table 2.4. The fitted curves are plotted in Figures 2.11 and 2.12, and the quantum yields for different thicknesses of films are summarised in Table 2.4. The quantum yields for $Mo(CO)_5PPh_3$ were calculated to be ~0.25 whereas the ones for $W(CO)_5PPh_3$ were found to be 0.4. The quantum yields for all three complexes are independent of the thickness of the film. A comparison of the quantum yields indicates that $W(CO)_5PPh_3$ has the largest quantum yield, that is, its photochemical reactions are the most efficient among the three. The first step in the photochemical reactions of $M(CO)_5PPh_3$ is the excitation of one of the electrons in the lower e orbitals to the upper a_1 orbital, which has been described in Section 2.2.2. The first excited state of $M(CO)_5PPh_3$ consists with five electrons in e and b_2 orbitals, and one electron in upper a_1 orbital. Ideally, a more electron negative metal centre results a higher energy upper a_1 orbital. For this reason, the upper a_1 orbital in the tungsten complex will be the most strongly antibonding among the three complexes because tungsten atom is more electronegative than molybdenum atom and chromium atom. As a result, the first excited state of $W(CO)_5PPh_3$ will be the least stable among them. Hence, the quantum yield for the tungsten complex is the largest among these three complexes.

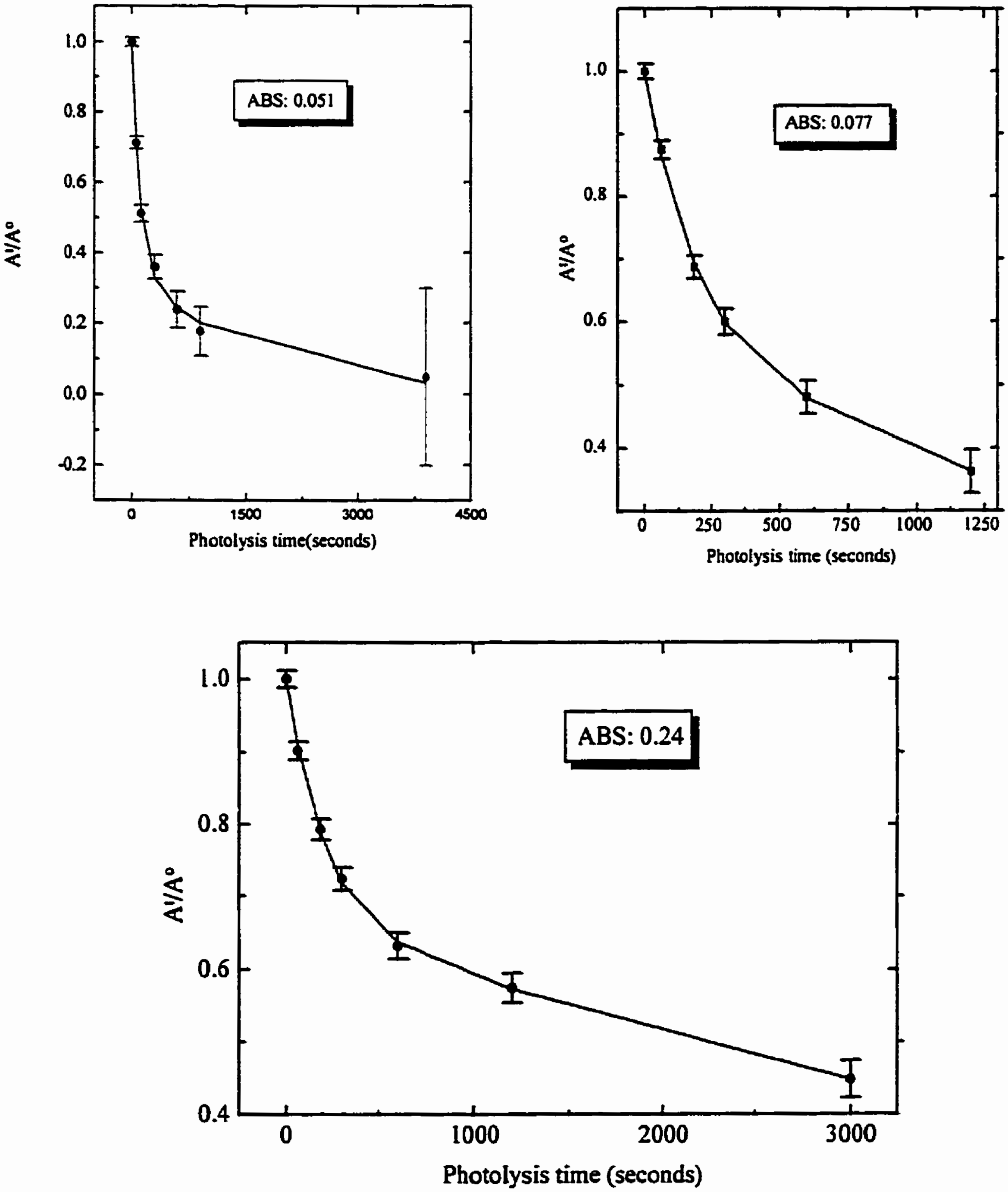

Figure 2.11 Plots of A^t/A^o vs. photolysis time for $Mo(CO)_5PPh_3$
(ABS = absorbance at 1925 cm^{-1})

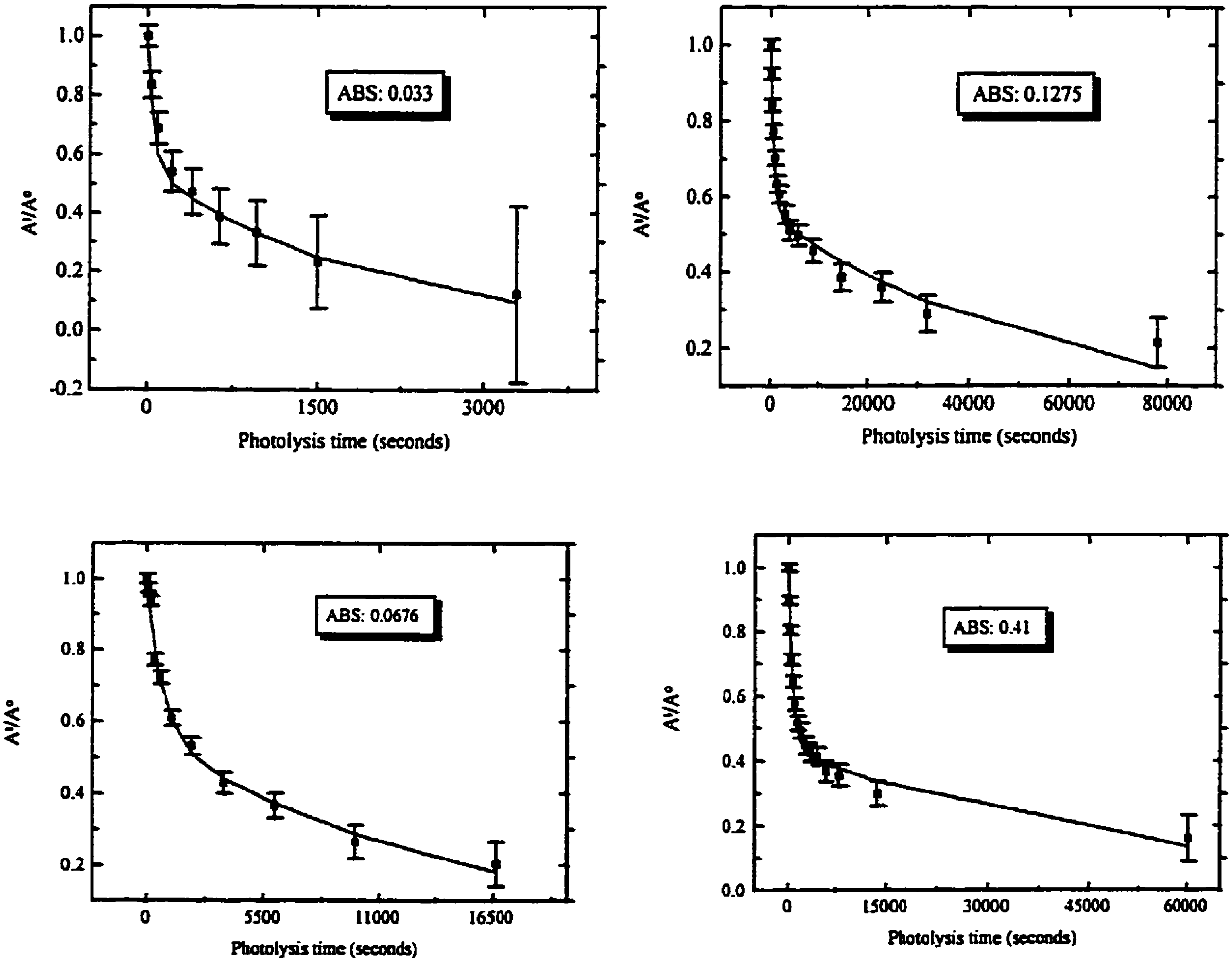

Figure 2.12 Plots of A^t/A^o vs. photolysis time for $W(CO)_5PPh_3$ (ABS = absorbance at 1917 cm^{-1})

2.3. Conclusion

The solid state photochemistry of $Cr(CO)_5PPh_3$, $Mo(CO)_5PPh_3$, and $W(CO)_5PPh_3$ complexes as films on silicon has been investigated. The complexes were proposed to undergo the photochemical process outlined by Equation 2.2.2:

$$M(CO)_5(PPh_3) \xrightarrow{h\nu} M(CO)_4(PPh_3) + CO \xrightarrow{h\nu} M + 5\ CO + PPh_3 \qquad (2.2.2)$$

where M = Cr, Mo and W.

The first photochemical reaction generated a five coordinate intermediate which decomposed upon further photolysis because it is also photosensitive. The final film consisted of the metals with carbon and phosphorus contaminations. An orbital correlation for the $M(CO)_5PPh_3$ molecules was used to interpret the photochemical reactions. There are two possible lowest singlet excited states which resulted from the $^1A_1(e^4b_2^2)$-$E_1(e^3b_2^2a_1^1)$ LF absorption and the $^1A_1(e^4b_2^2)$-$E_1(e^3b_2^2b_1^1)$ LF absorption. They both lead to the loss of one of the carbonyls and forming a five coordinate intermediate whose symmetry was determined to be Cs by its FTIR spectra. A kinetic equation was derived in order to calculate quantum yields for a two sequential photochemical process. The quantum yields for the first step of the photo-decomposition were calculated at different thicknesses for all three complexes. Their quantum yields are not dependent on the film thickness, and the relative order is W > Mo >> Cr. The differences in quantum yields between these three complexes are the result of their different stabilities in the first excited states. The difference in the stabilities of the first excited states arises because of the differences in electronegativity among the three metals. Even though the photochemical processes of the three complexes are all very efficient, it is impossible to use them in any practical device fabrication because of the contamination in the final films. While this system is not in itself useful, it does serve to demonstrate the concept. In order to improve this system, there are two problems which need to be solved. The first is the presence of the intermediate and the second is the purity of the film. If the initial photoproduct is $M(CO)_4PPh_3$ (after the exclusion of one CO), then designing a system where the initial photoproduct is less stable may eliminate the problem associated with a thermally stable intermediate. This intermediate must be de-stabilised so that rapid thermal decomposition occurs prior to any subsequent reaction. In order to generate a primary photoproduct which is less stable, poor π acceptor ligands will be used in place of PPh_3 and one CO. These poor π acceptor ligands have less ability to stabilise low oxidation state molecules such as the intermediate. In the following chapter, ligands based on ethylenediamine are used to replace one CO and the PPh_3 ligand on metal centres. These metal complexes will be investigated in a similar manner to that used for the $M(CO)_5PPh_3$ molecules. Finally, whether or not this proposal is the solution to the above two problems will be discussed.

2.4 Experimental

2.4.1 Materials selection

The silicon wafers were obtained from Pacific Microelectronics Centre, Canada. The Si(111) surface was used in these studies and the wafers were p-type silicon with tolerances and specifications as per SEMI Standard M1.1.STD.5 and were cut to the approximate dimensions of 1 cm x 1.5 cm in house. The CaF_2 crystals were obtained from Wilmad Glass Co. Inc..

Using a Bomem Michelson 120 FTIR spectrophotometer, FTIR spectra with 4 cm^{-1} resolution were obtained. The samples were held in an aluminium sample mount within NaCl or CaF_2 faced vacuum dewars. The photolysis beam was a 100 W high pressure Hg lamp in an Oriel housing equipped with condenser lenses and filtered through a 10 cm water filter with Pyrex optics. Auger electron spectra were obtained using a PHI double pass CMA at 0.85 eV resolution at the Surface Physics Laboratory, Dept. of Physics, Simon Fraser University.

2.4.2 Preparation of $M(CO)_5PPh_3$ (M= Cr, Mo, W)

The complexes $M(CO)_5PPh_3$ (M= Cr, Mo, W) were all prepared by the literature method [66] and characterised by FTIR and elemental analysis.

Table 2.5 Elemental analysis for $M(CO)_5PPh_3$ (M = Cr, Mo, W)

Complex	%C	%H	
$Cr(CO)_5PPh_3$	60.80	3.30	calc.
	60.60	3.40	found
$Mo(CO)_5PPh_3$	55.50	3.00	calc.
	55.41	3.15	found
$W(CO)_5PPh_3$	47.20	2.60	calc.
	47.00	2.65	found

2.4.3 Calibration of absorption on surface

A stock solution of $Cr(CO)_5PPh_3$ (0.0060 g) was prepared in CH_2Cl_2 (20.0 ml). A drop (0.0037 ml) of this solution was then deposited on the surface of a Si wafer. The solvent was allowed to evaporate and the FTIR spectrum was obtained. The area of the drop was found to be 0.785 cm^2. This corresponds to a coverage of 3.1×10^{-9} molecules per cm^2. This process was repeated several times and the corresponding calibration curve of absorbance versus mole/cm^2 of $Cr(CO)_5PPh_3$ is shown in Figure 2.2. Similar experiments were conducted with solutions of $Mo(CO)_5PPh_3$ and $W(CO)_5PPh_3$ in CH_2Cl_2. The curves obtained are shown in Figure 2.2 and 2.3.

2.4.4 Photolysis of the complexes as films on silicon surfaces

All photolysis experiments were completed in the same manner. A typical experiment is described in this section. Approximately 5 mg of $Cr(CO)_5PPh_3$ was dissolved in 2 mL CH_2Cl_2 to make a stock solution. A drop of the stock solution was spin cast on a silicon chip. This resulted in the formation of a smooth, uniform coating of the chip. The chip was then transferred to a vacuum dewar in which the FTIR spectrum was recorded. The pressure of the vacuum dewar is 1×10^{-4} torr. Another FTIR spectrum was recorded after the sample was irradiated for 5 seconds. This procedure was repeated for the following (accumulated) photolysis times: 10, 15, 20, and 240 seconds. The sample was then transferred to the Auger spectrometer for an elemental analysis of the surface. Similar experiments were conducted with $Mo(CO)_5PPh_3$ and $W(CO)_5PPh_3$.

CHAPTER 3

Solid state photochemistry of $M(CO)_4(L\text{-}L)$ (M= Cr (L-L = en, Me_2-en, Et_2-en), Mo (L-L = Me_2-en, Et_2-en), W (L-L = Et_2-en))

3.1 Introduction

Metal oxide films of chromium, molybdenum and tungsten have been deposited from the $M(CO)_5PPh_3$ molecules via the room temperature photochemical process. The design, process and the film quality have been discussed in the last chapter. These films contain too much phosphorus and carbon to be used in practical device fabrications. In addition, the presence of the intermediates, $M(CO)_4PPh_3$, decreases the efficiency of the photochemical process. The resolution of these two problems is therefore the objective of this chapter. It was reported both in the last chapter and publications that After photolysis, the phosphorus ligands were assumed to remain as PPh_3 which is a solid at room temperature with melting point at 88°C [68, 70]. The contamination problem which arose from using $M(CO)_5PPh_3$ precursors was assumed to result from the relatively heavy and stable PPh_3 has difficulty diffusing out of the films after photolysis. For this reason, a series of ethylenediamine ligands were chosen to replace the phosphorus ligands. The ethylenediamine ligands may leave the film more easily after photolysis because the molecular weight of ethylenediamine is about half of the weight of PPh_3. Moreover, these ethylenediamine ligands are poor π acceptors making them less able to stabilise low oxidation state molecules such as the intermediate. As a result, the photochemistry of the nitrogen donor complex may proceed without the formation of a thermally stable intermediate. Recall from the discussion in the last chapter that the intermediate of the photochemical reaction of $M(CO)_5PPh_3$ is $M(CO)_4PPh_3$. If the possibility of forming a thermally stable intermediate containing ethylenediamine can be eliminated, then the possibility of having contaminations from the ligands in the starting material will be decreased. It has been reported that the photolysis of the metal complexes containing ethylenediamine ligands resulted in an extrusion of the ethylenediamine ligands [77]. Since ethylenediamine ligands are in liquid form at room temperature, these ligands have high vapour pressure and thus making them easier to be removed after photolysis comparing to PPh_3. Thus, an improved deposition process may be expected if the ethylenediamine containing complexes were used as precursors. Complexes of the $M(CO)_4(L\text{-}L)$ type were made for this study, where M= Cr, Mo, W and L-L = en, Me_2-en Et_2-en (en = ethylenediamine, Me_2-en = *N,N'*-dimethyl ethylenediamine, Et_2-en = *N,N*-diethyl ethylenediamine) (see Figure 3.1). This chapter has been divided into the following sections: discussions on the quality of the amorphous films, comparisons of the symmetry of the complexes, discussions on the photochemistry of the complexes, and comparisons of the photoefficiency of their reactions. Finally, whether or not the substitution of nitrogen donor for phosphorus donor ligands has solved the problems that arose in Chapter 2 will be discussed.

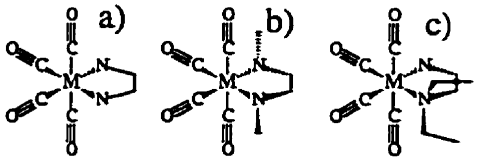

Figure 3.1 Structure of $M(CO)_4(L\text{-}L)$, where a) LL = en, b) LL = Me_2-en, and c) LL = Et_2-en (M = Cr, Mo, W).

3.2 Results and Discussion

3.2.1 Quality of $M(CO)_4(L\text{-}L)$ (M= Cr, Mo, W and L-L = en, Me_2-en, Et_2-en) films

Films of the $M(CO)_4(L\text{-}L)$ complexes were made by spin coating, and their film quality was found to be dependent on both the identity of the metal and the ligands. All of the chromium complexes, $Cr(CO)_4(en)$, $Cr(CO)_4(Me_2\text{-}en)$ and $Cr(CO)_4(Et_2\text{-}en)$, could be cast into thin precursor films. The quality of the film depends on both the ease of forming an amorphous precursor film and the uniformity of the film (inspected under microscope). The relative order of the quality of amorphous film is $Cr(CO)_4(Et_2\text{-}en) > Cr(CO)_4(Me_2\text{-}en) > Cr(CO)_4(en)$. This order is in agreement with the idea that larger organic substituents on the nitrogen render the molecule less symmetric. It has been discussed in Chapter 2 that lower symmetry metal complexes form amorphous films instead of crystalline films upon spin coating. Films of $Mo(CO)_4(en)$ formed by spin coating were crystalline; however, $Mo(CO)_4(Me_2\text{-}en)$ and $Mo(CO)_4(Et_2\text{-}en)$ were reliably cast as amorphous films. The fact that only the two larger substituted molybdenum complexes formed amorphous films upon spin coating indicates that the ligand size effect on the molybdenum complex is larger than on the chromium complex. Since a chromium atom is smaller than a molybdenum atom, the ligands on the molybdenum must be larger in order to affect the packing of the molecule significantly. In the tungsten case, only the most heavily substituted compound, $W(CO)_4(Et_2\text{-}en)$, formed amorphous films reproducibly. Tungsten is similar in size to molybdenum indicating that other effects (i.e., dipole) are also important. The room temperature photochemical process can only be usefully applied to amorphous films because the back reaction between the extruded ligand and the metal centre in a crystalline film is enhanced by the lattice energy. Thus, solid state photochemistry was only studied on the complexes that formed amorphous films upon spin coating.

3.2.2 Symmetry considerations and spectroscopy of solid state $M(CO)_4(L\text{-}L)$ ($M=$ Cr, Mo, W and L-L = en, Me_2-en, Et_2-en)

The FTIR spectral information associated with a spin cast film containing $Cr(CO)_4(en)$ is summarised in Table 3.1. This complex can be approximated to have a C_{2v} conformation by considering only the metal, the carbonyls and the two nitrogens. A C_{2v} molecule has four carbonyl stretching fundamentals: one B_1, one B_2 and two A_1 modes. The frequencies of these four vibrations in solid films are similar to those found in solution (see Table 3.1) [78]. The carbonyl stretching frequencies of the remaining $M(CO)_4(L\text{-}L)$ complexes in the solid state are also reported in Table 3.1. Because these complexes can also have approximate C_{2v} symmetry as $Cr(CO)_4(en)$, their carbonyl stretching fundamentals were assigned according to the assignments in the spectrum of $Cr(CO)_4(en)$. The spectra of these compounds exhibited absorption bands in approximately the same region. Thus, the influence of the organic substituents as well as the identity of the metals on the energy of the carbonyl stretching vibration was not too significant. The electronic absorption spectrum for $Cr(CO)_4(en)$ in solid state was recorded, and the spectral data are listed in Table 3.2.

Table 3.1 **FTIR spectral information for $M(CO)_4(L\text{-}L)$ (M= Cr, Mo, W and L-L = en, Me_2-en, Et_2-en) as solid films and in solution**

Compound	A_1	B_1	A_1	B_2	Reference
units	cm^{-1}	cm^{-1}	cm^{-1}	cm^{-1}	cm^{-1}
$Cr(CO)_4(en)$	2002	1871	1861	1778	as a solid film [this work]
	2000w	1870vs	1860s,sh	1823s	in dimethoxyethane [78]
	2004	1873	1855	1810	in CH_3NO_2 [79]
$Cr(CO)_4(Me_2$-en)	2004	1898	1856	1786	as a solid film [this work]
$Cr(CO)_4(Et_2$-en)	2004	1873	1848	1784	as a solid film [this work]
$Mo(CO)_4(en)$	2005	1880	1855	1755	as a solid film [this work]
	2005w	1880vs	1865s,sh	1825s	in dimethoxyethane [78]
	2015	1890	1864	1818	in CH_3NO_2 [79]
$Mo(CO)_4(Me_2$-en)	2016	1908	1861	1784	as a solid film [this work]
$Mo(CO)(Et_2$-en)	2012	1871	1852	1804	as a solid film [this work]
$W(CO)_4(en)$	2006	1867	1857	1757	as a solid film [this work]
	2000w	1864vs	1850s,sh	1818	in dimethoxyethane[78]
	2006	1867	1852	1809	in CH_3NO_2 [79]
$W(CO)_4(Me_2$-en)	2000	1892	1842	1788	as a solid film [this work]
$W(CO)_4(Et_2$-en)	2004	1873	1852	1805	as a solid film [this work]

vs = very strong; s = strong; w = weak; ; sh = shoulder

Table 3.2 **Spectral features of $M(CO)_4(L\text{-}L)$ (M= Cr , Mo, W and L-L = en, Me_2-en, Et_2-en) as solid films and in solution**

Complexes	Bands, cm^{-1} (ε, cm^2/mole) or [ε, *l*/mole]	Assignment	Reference
$Cr(CO)_4(en)$	23810(8.1×10^5)	LF ($^1A_1 \rightarrow {}^1A_1$, $^1B_2$)	as a solid film [this work]
	29240(1.7×10^6)		
	38462(3.6×10^6)	$M \rightarrow \pi^*CO$ CT + LF	
	43478(3.5×10^6)	$M \rightarrow \pi^*CO$ CT + LF	
	50000(2.8×10^6)	$M \rightarrow \pi^*CO$ CT + LF	
	23,600[1.3×10^3]	LF ($^1A_1 \rightarrow {}^1A_1$, $^1B_2$)	in methanol [80]
	29,700 [5.4×10^3]		
	35,500 [6.3×10^3]	$M \rightarrow \pi^*CO$ CT + LF	
	40,300 [1.8×10^4]	$M \rightarrow \pi^*CO$ CT + LF	
	46,200 [2.2×10^4]	$M \rightarrow \pi^*CO$ CT + LF	
$Cr(CO)_4(Me_2\text{-}en)$	22,727(1.7×10^6)	LF ($^1A_1 \rightarrow {}^1A_1$, $^1B_2$)	a solid film [this work]
	28,571(3.6×10^6)		
	38,461(6.5×10^6)	$M \rightarrow \pi^*CO$ CT + LF	
	43,478(7.0×10^6)	$M \rightarrow \pi^*CO$ CT + LF	
	50,000(6.9×10^6)	$M \rightarrow \pi^*CO$ CT + LF	
$Cr(CO)_4(Et_2\text{-}en)$	22,727[8.8×10^5]	LF ($^1A_1 \rightarrow {}^1A_1$, $^1B_2$)	a solid film [this work]
	29,411[2.2×10^6]		
	38,461[5.7×10^6]	$M \rightarrow \pi^*CO$ CT + LF	
	43,478[5.7×10^6]	$M \rightarrow \pi^*CO$ CT + LF	
	50,000[3.0×10^6]	$M \rightarrow \pi^*CO$ CT + LF	

Table 3.2 (Continued)

$Mo(CO)_4(en)$	25,300 [1.7 x 10^3]	LF ($^1A_1 \rightarrow {}^1A_1, {}^1B_2$)	in methanol [80]
	32,700 [1.0 x 10^4]	$M \rightarrow \pi^*$CO CT + LF	
	38,300 [2.0 x 10^4]	$M \rightarrow \pi^*$CO CT + LF	
	43,400 [2.0 x 10^4]	$M \rightarrow \pi^*$CO CT + LF	
$Mo(CO)_4(Me_2\text{-}en)$	25,000(4.5 x 10^6)	LF ($^1A_1 \rightarrow {}^1A_1, {}^1B_2$)	a solid film [this work]
	30,303(7.0 x 10^6)	$M \rightarrow \pi^*$CO CT + LF	
	37,037(6.5 x 10^6)	$M \rightarrow \pi^*$CO CT + LF	
	43,478(5.4 x 10^6)	$M \rightarrow \pi^*$CO CT + LF	
$Mo(CO)_4(Et_2\text{-}en)$	25,641(2.2 x 10^6)	LF ($^1A_1 \rightarrow {}^1A_1, {}^1B_2$)	a solid film [this work]
	32,258(4.3 x 10^6)	$M \rightarrow \pi^*$CO CT + LF	
	38,461(5.2 x 10^6)	$M \rightarrow \pi^*$CO CT + LF	
	47,619(5.4 x 10^6)	$M \rightarrow \pi^*$CO CT + LF	
$W(CO)_4(en)$	22,200[4.0 x 10^2]	LF ($^1A_1 \rightarrow {}^3A_1, {}^3B_2$)	in methanol [80]
	25,200 [1.4 x 10^3]	LF ($^1A_1 \rightarrow {}^1A_1, {}^1B_2$)	
	33,200 [8.3 x 10^3]	$M \rightarrow \pi^*$CO CT + LF	
	39,200 [2.8 x 10^4]	$M \rightarrow \pi^*$CO CT + LF	
	45,000 [2.8 x 10^4]	$M \rightarrow \pi^*$CO CT + LF	
$W(CO)_4(Et_2\text{-}en)$	22,727(3.9 x 10^6)	LF ($^1A_1 \rightarrow {}^3A_1, {}^3B_2$)	a solid film [this work]
	26,315(6.2 x 10^6)	LF ($^1A_1 \rightarrow {}^1A_1, {}^1B_2$)	
	33,333(1.7 x 10^7)	$M \rightarrow \pi^*$CO CT + LF	
	38,461(2.3 x 10^7)	$M \rightarrow \pi^*$CO CT + LF	
	45,454(2.0 x 10^7)	$M \rightarrow \pi^*$CO CT + LF	

In general, the band position was sensitive to the nature of the metal, the nature of the ligand, and the medium in which the spectra were measured [66]. However, because of the similarity between the spectra in solution and in solid films, the assignments of the spectra in solid films were made according to the published assignments in solution [80]. The lowest energy absorption band is the LF ($^1A_1 \rightarrow {}^1A_1, {}^1B_2$) transition [80, 81]. The electronic absorption spectra of the remaining $M(CO)_4(L\text{-}L)$ complexes in the solid state were recorded, and the spectral data are also listed in Table 3.2. Their spectral assignments were made according to the assignments in solution because of the strong spectral similarity between them. The extinction coefficients were calculated by substituting the absorbance maximum in the UV/VIS spectra and the concentration into Beer's Law [47, 48]. The concentration used for the solid film was determined by correlating the coverage of the complex on the surface to the absorbance in FTIR. These absorption/coverage plots are shown in Figures 3.2 and 3.3.

3.2.3 Photochemistry of $M(CO)_4(L\text{-}L)$ (M= Cr (L-L = en, Me_2-en, Et_2-en), Mo (L-L = Me_2-en, Et_2-en), W (L-L = Et_2-en)) as solid films

In order to perform the lowest energy LF ($^1A_1 \rightarrow {}^1A_1, {}^1B_2$) transition, a film of $Cr(CO)_4(en)$ was irradiated at $\lambda = 366$ nm (2.7×10^{-3} cm^{-1}). This photolysis results in the loss of all vibrational bands in FTIR spectra. No additional band which may be attributed to an intermediate was observed. Apparently, the initially formed intermediate has insufficient thermal stability to be detected on the time scale of this experiment. These results are consistent with an initial ligand loss, generating an intermediate which is not thermally stable and rapidly loses all its remaining ligands.

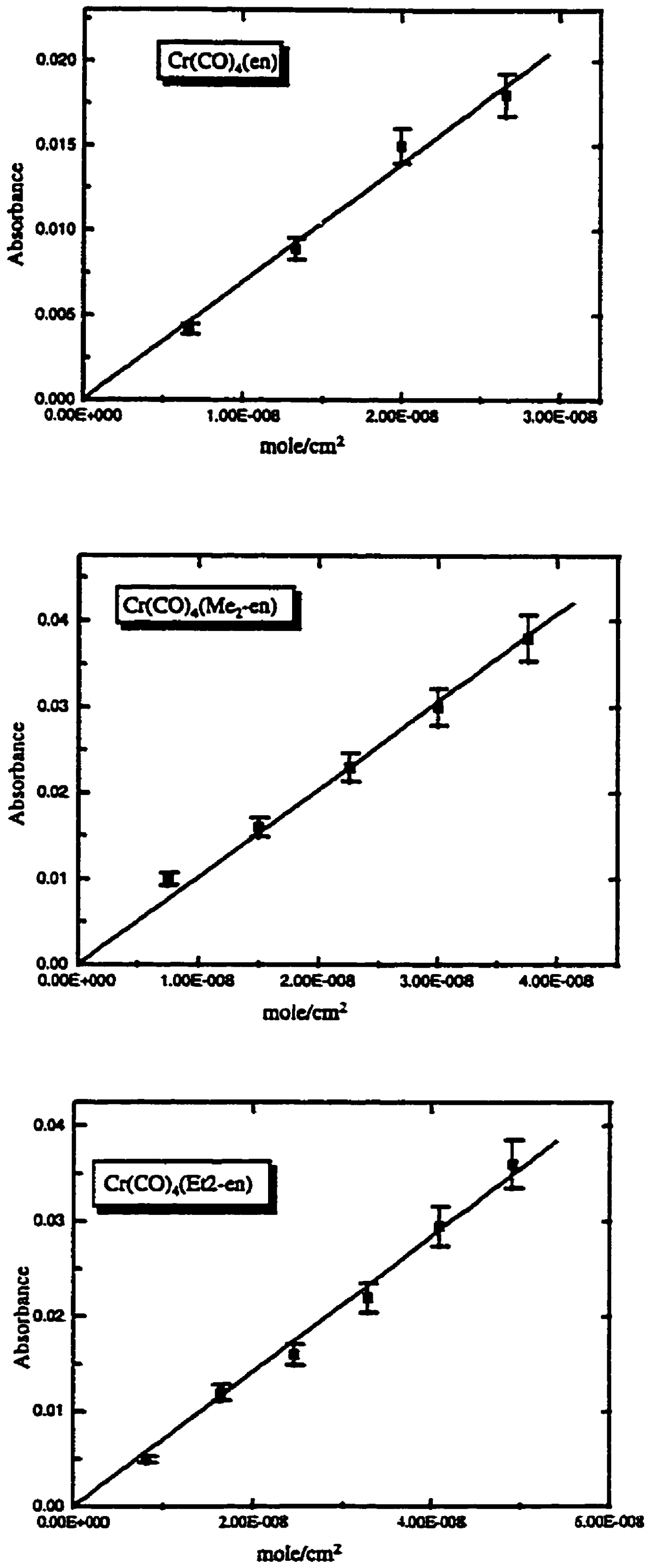

Figure 3.2 Plots of absorption vs. surface coverage for Cr(CO)$_4$(L-L)

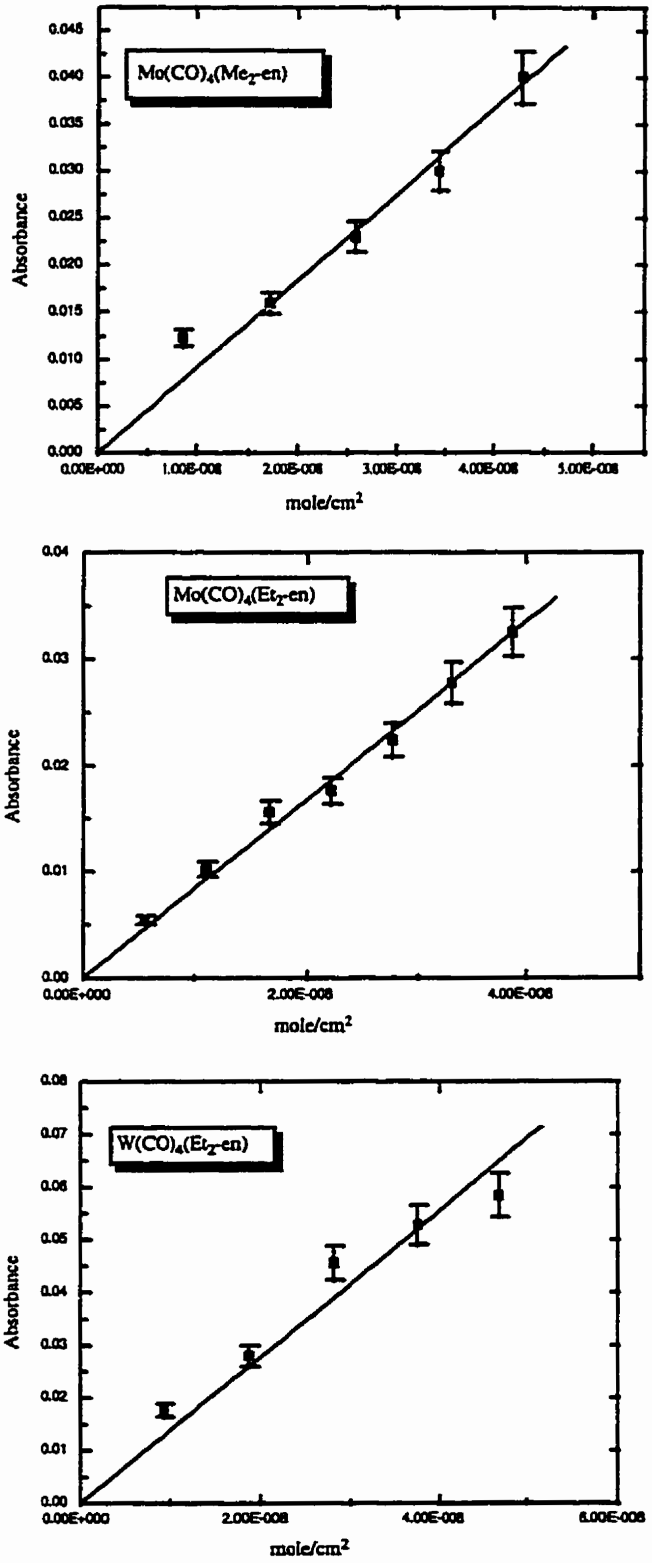

Figure 3.3 Plots of absorption vs. surface coverage for $Mo(CO)_4(L\text{-}L)$ and $W(CO)_4(L\text{-}L)$

Photolysis of the remaining $M(CO)_4(L\text{-}L)$ complexes resulted in the loss of the absorption bands of the starting material with no detectable intermediate. Their photochemical reactions can be summarised as follows.

$$M(CO)_4(L\text{-}L) \xrightarrow{h\nu} M(CO)_3(L\text{-}L) + CO \longrightarrow M + 4\,CO + L\text{-}L \qquad (3.1)$$

or

$$M(CO)_4(\eta^2\text{-}L\text{-}L) \xrightarrow{h\nu} M(CO)_4(\eta^1\text{-}L\text{-}L) \longrightarrow M + 4\,CO + L\text{-}L \qquad (3.2)$$

M= Cr, Mo, and W, L-L = en, Me_2-en, and Et_2-en

This substitution of PPh_3 with nitrogen ligands has clearly solved the problem associated with the thermally stable intermediate observed in the photolysis of $M(CO)_5PPh_3$.

In order to interpret the photochemical reactions of these C_{2v} complexes, an orbital correlation diagram is illustrated in Figure 3.4. The first molecular orbital diagram represents the ground state of $Cr(CO)_4(en)$ with six d-electrons occupying the lower a_1, b_1, and a_2 orbitals leaving the upper a_1 and b_2 orbitals empty. The first excited state of this complex is illustrated in the second molecular orbital diagram, where an electron from the a_1 orbital is excited into either the upper a_1 ($dx^2\text{-}y^2$) orbital or b_2 (d_{yz}) orbital after the absorption of a photon. Population of the ($a_2{}^2b_1{}^2a_1{}^2 \rightarrow a_2{}^2b_1{}^2a_1{}^1a_1{}^1$) level strongly labilizes one of the CO's on the x-axis. This results in a cleavage of this axial CO in order to lower the energy of the molecule. Alternatively, population of the ($a_2{}^2b_1{}^2a_1{}^2 \rightarrow a_2{}^2b_1{}^2a_1{}^1b_2{}^1$) level results in the labilization of the equatorial ligands (the M-$CO_{(eq)}$ or the M-$N_{(eq)}$ bond). This results in the loss of either the M-$CO_{(eq)}$ or the M-$N_{(eq)}$ bond.

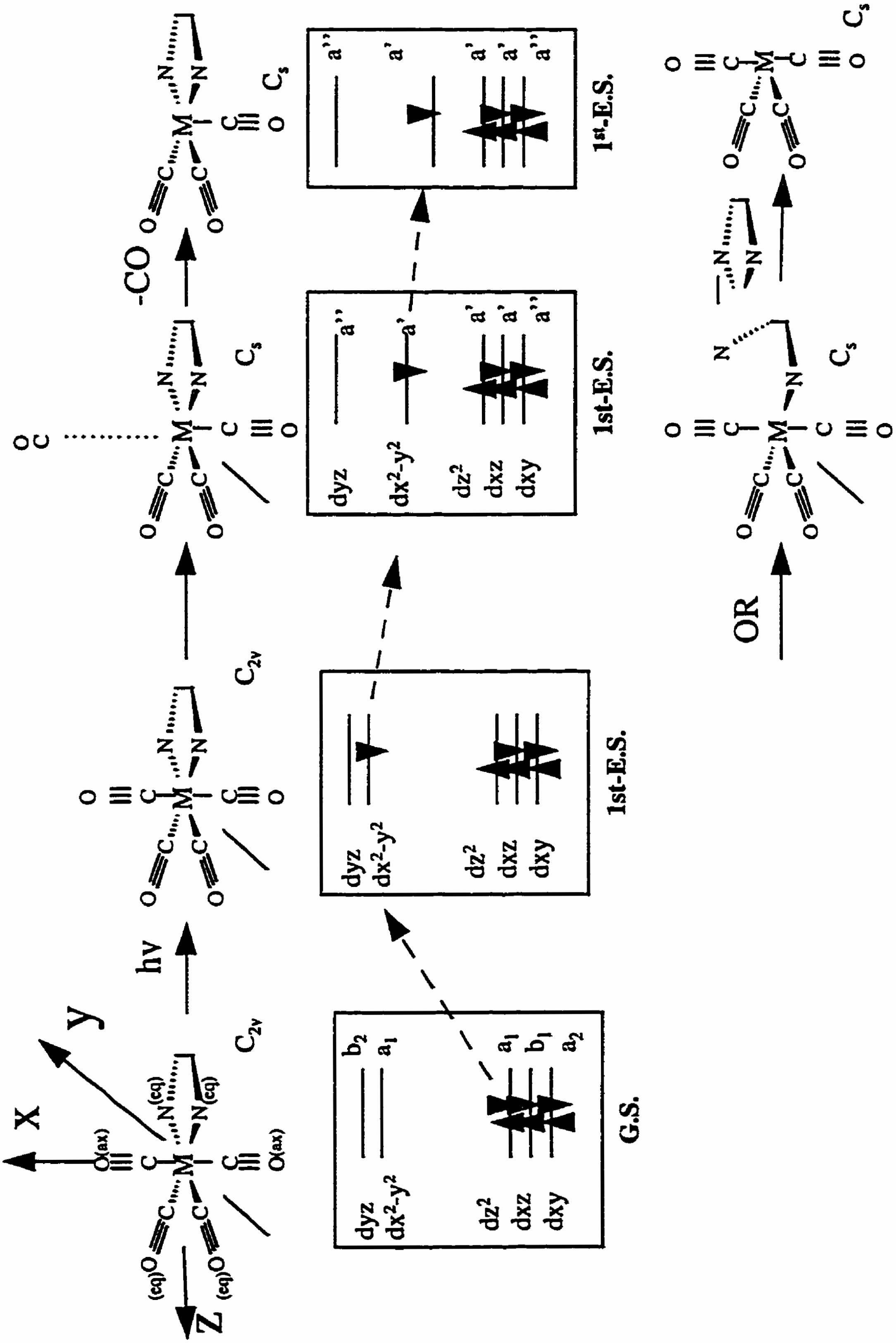

Figure 3.4 Orbital correlation diagram for the photochemical reaction of $Cr(CO)_4(en)$, where (eq) = equatorial (ax) = axial

The third molecular orbital diagram shows the electron in the a_1 orbital is at lower energy following the loss of a CO, or a breaking of a M-N bond. This relaxation provides the driving force for the reaction. Presumably, the resultant complex does not have enough thermal stability and hence loses all the remaining ligands because there is no intermediate observed in the photochemical reaction. It has been reported that dissociation occurs for the M-N bond when the wavelength of light used is 366 nm, even though both M-CO and M-N lability are enhanced in the excited state [77]. This selectivity is due to the higher lability of the M-N bond than the M-CO bond in the ground state. Thus, the photochemical reactions of the $M(CO)_4(L\text{-}L)$ complexes were assumed to proceed via Equation 3.2. The overall photochemical reaction for both proposed reaction routes is the loss of all ligands and leaving only metals on the substrate. In addition, since there is no detectable intermediate, the photochemical reaction is a first order reaction.

3.2.4 Quantum yields for the reactions of $M(CO)_4(L\text{-}L)$ (M= Cr (L-L = en, Me_2-en, Et_2-en), Mo (L-L = Me_2-en, Et_2-en), W (L-L = Et_2-en)) as solid films

In order to determine the photoefficiency of the reaction, quantum yields were calculated. The quantum yield for the first order photochemical reaction was determined via Equation 1.4. The parameters used for the calculation are summarised in Table 3.3. For example, the intensity of the incident light, Io, used for the photochemical reaction of $Cr(CO)_4(en)$ was 3.18×10^{-9} $mole^{-1}$ s cm^2. The extinction coefficient, ε_A, at 366 nm was found to be 9.20 x 10^5 mol^{-1} cm^2. After entering all these parameters to Equation 1.4 and performing the least-squares fit of the absorption-irradiation time data, the quantum yield for the photo-decomposition was calculated to be (4.3±0.4) x 10^{-3}. The quantum yield is reported in Table 3.3, while the fitted graph and the FTIR spectral changes are illustrated in Figure 3.5. The quantum yields for the remaining chromium complexes as well as the molybdenum and the tungsten complexes were calculated in an analogous way. The quantum yields and the parameters used for this calculation are all summarised in Table 3.3. The FTIR spectra associated with the photolysis of these compounds and the fitted graphs are shown in Figures 3.6 to 3.10.

Table 3.3 Quantum yields and fitting data for $M(CO)_4(L\text{-}L)$ (M= Cr (L-L = en, Me_2-en, Et_2-en), Mo (L-L = Me_2-en, Et_2-en), W (L-L = Et_2-en)) irradiated at 366 nm

Complexes	Φ_{366}	χ^2	Io (s cm^2 $mole^{-1}$)	ε_A (cm^2 $mole^{-1}$)	ε_a (cm^2 $mole^{-1}$)
$Cr(CO)_4(en)$	(4.3±0.4) x 10^{-3}	0.98	3.18 x 10^{-9}	9.20 x 10^5	6.80 x 10^5
$Cr(CO)_4(Me_2\text{-en})$	(4.3±0.3) x 10^{-3}	0.96	5.02 x 10^{-9}	2.82 x 10^6	1.02 x 10^6
$Cr(CO)_4(Et_2\text{-en})$	(1.3±0.059)x 10^{-2}	0.97	5.02 x 10^{-9}	1.20 x 10^6	6.84 x 10^5
$Mo(CO)_4(Me_2\text{-en})$	(6.1±0.72) x 10^{-4}	0.97	5.20 x 10^{-9}	3.08 x 10^6	9.06 x 10^5
$Mo(CO)_4(Et_2\text{-en})$	(4.2±0.45) x 10^{-3}	0.96	5.20 x 10^{-9}	2.31 x 10^6	8.70 x 10^5
$W(CO)_4(Et_2\text{-en})$	(1.6±0.08) x 10^{-4}	0.99	4.44 x 10^{-9}	6.55 x 10^6	1.50 x 10^6

χ^2: correlation coefficient

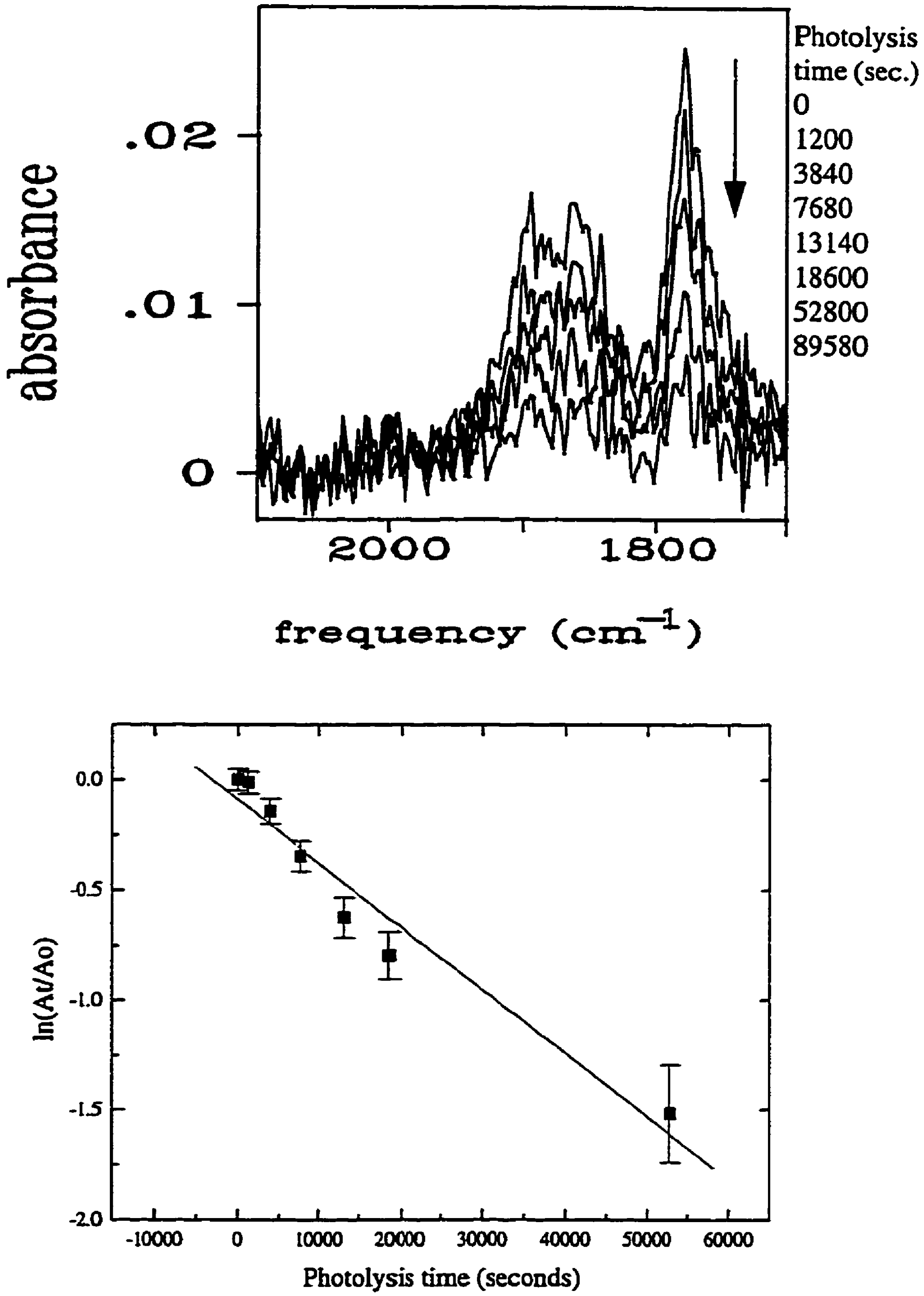

Figure 3.5 FTIR spectra associated with the photolysis of $Cr(CO)_4(en)$ and plots of $\ln(A^t/A^o)$ vs. photolysis time

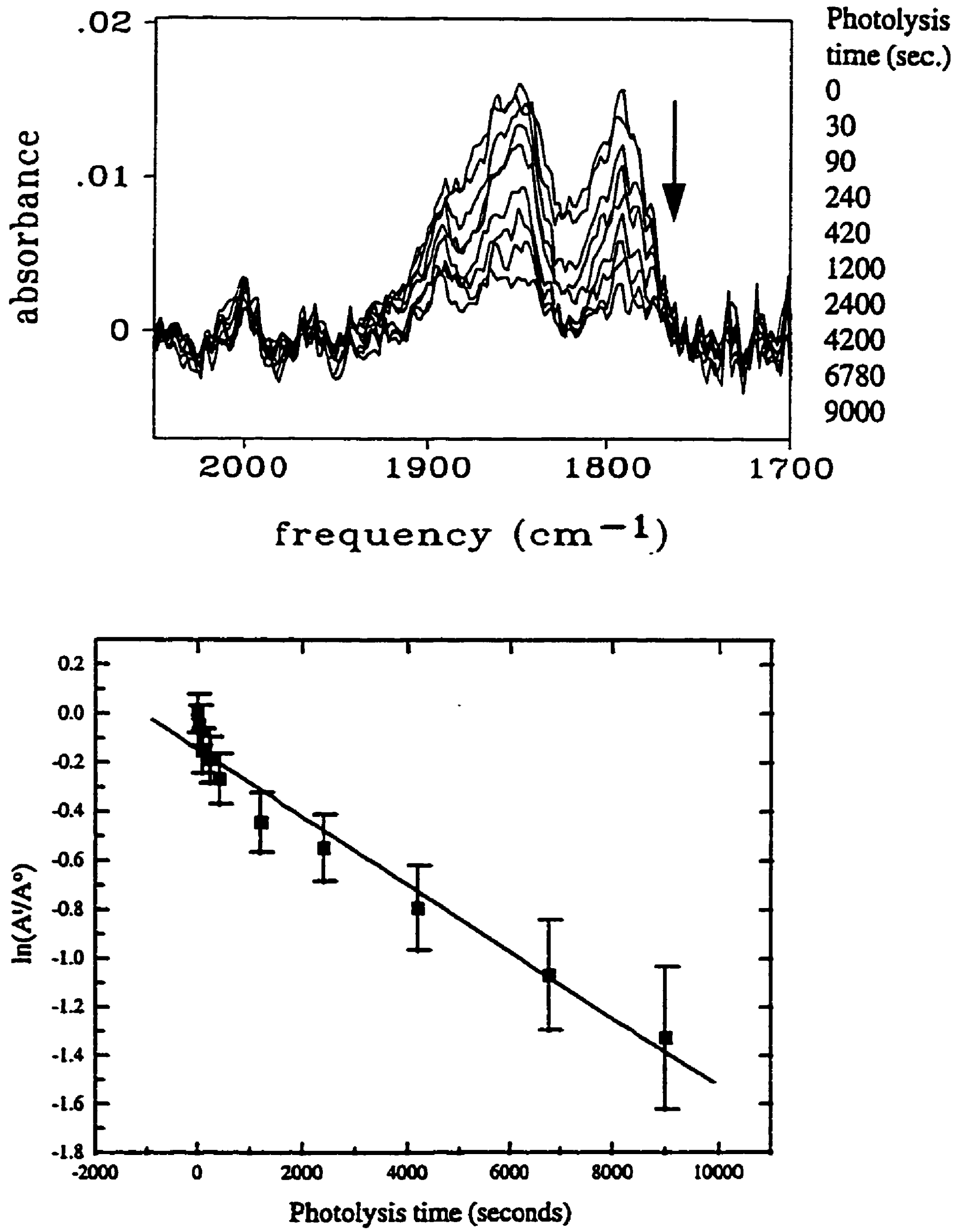

Figure 3.6 FTIR spectra associated with the photolysis of $Cr(CO)_4(Me_2\text{-en})$ and plots of $\ln(A^t/A^o)$ vs. photolysis time

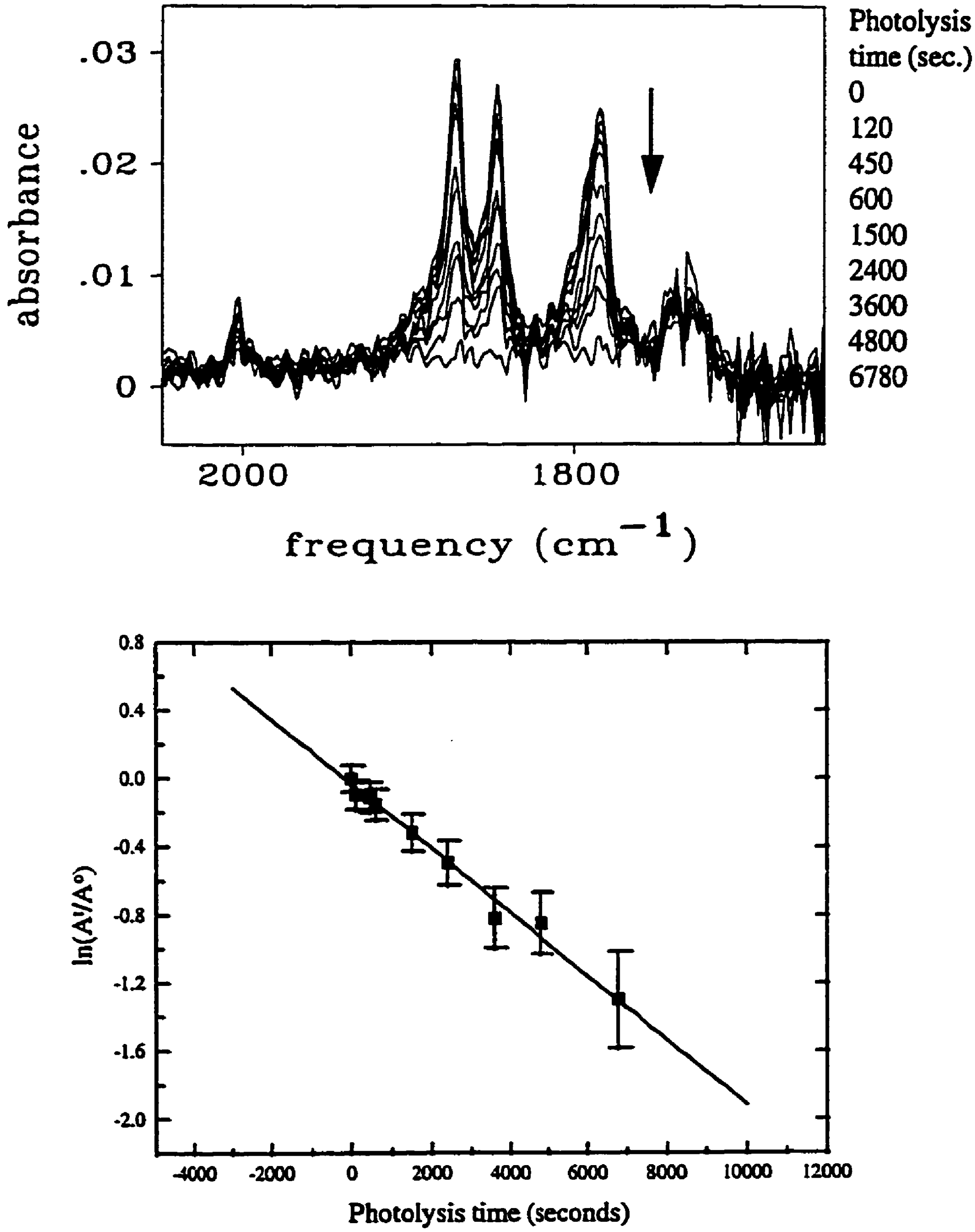

Figure 3.7 FTIR spectra associated with the photolysis of $Cr(CO)_4(Et_2\text{-en})$ and plots of $\ln(A^t/A^o)$ vs. photolysis time

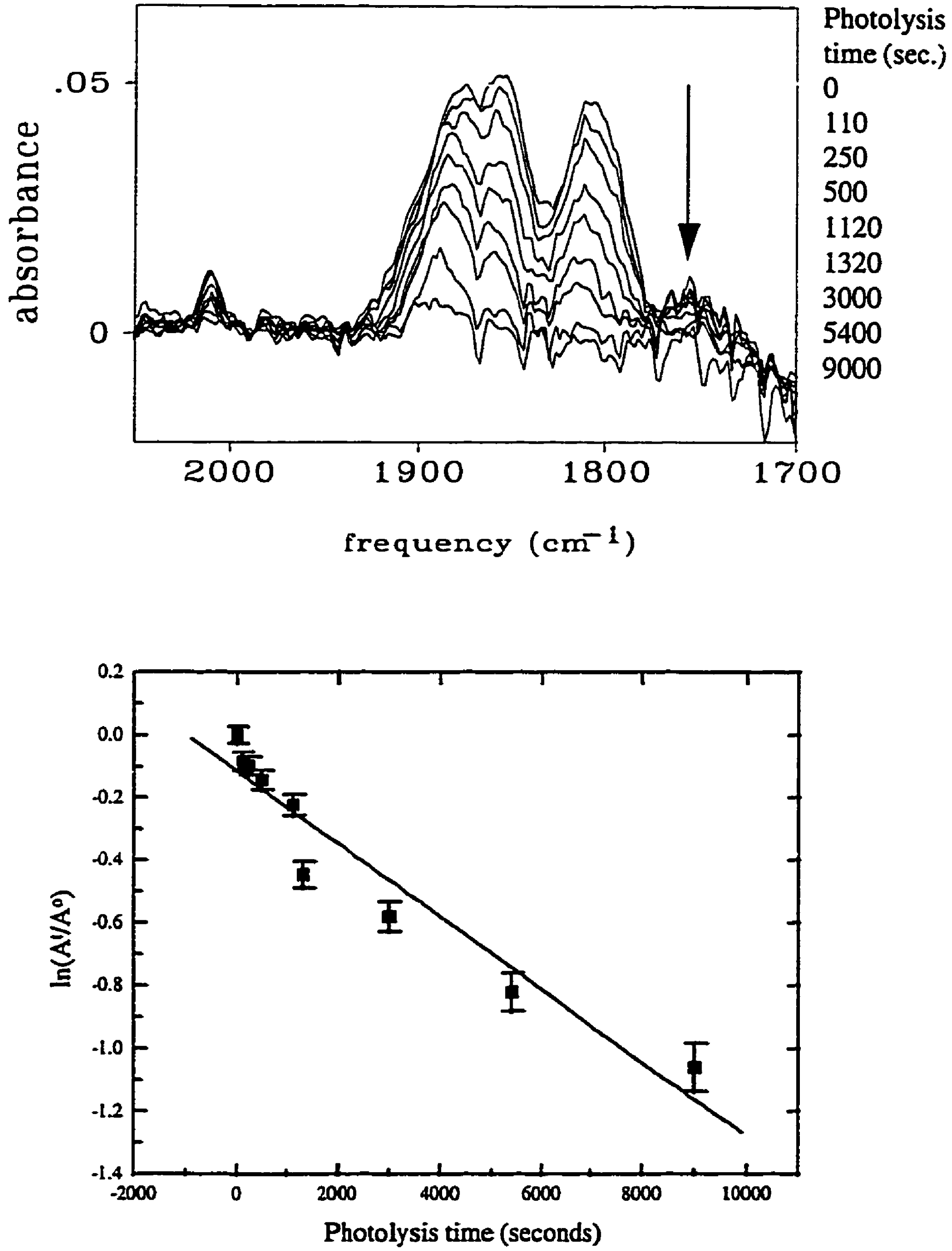

Figure 3.8 FTIR spectra associated with the photolysis of $Mo(CO)_4(Me_2\text{-en})$ and plots of $\ln(A^t/A^o)$ vs. photolysis time

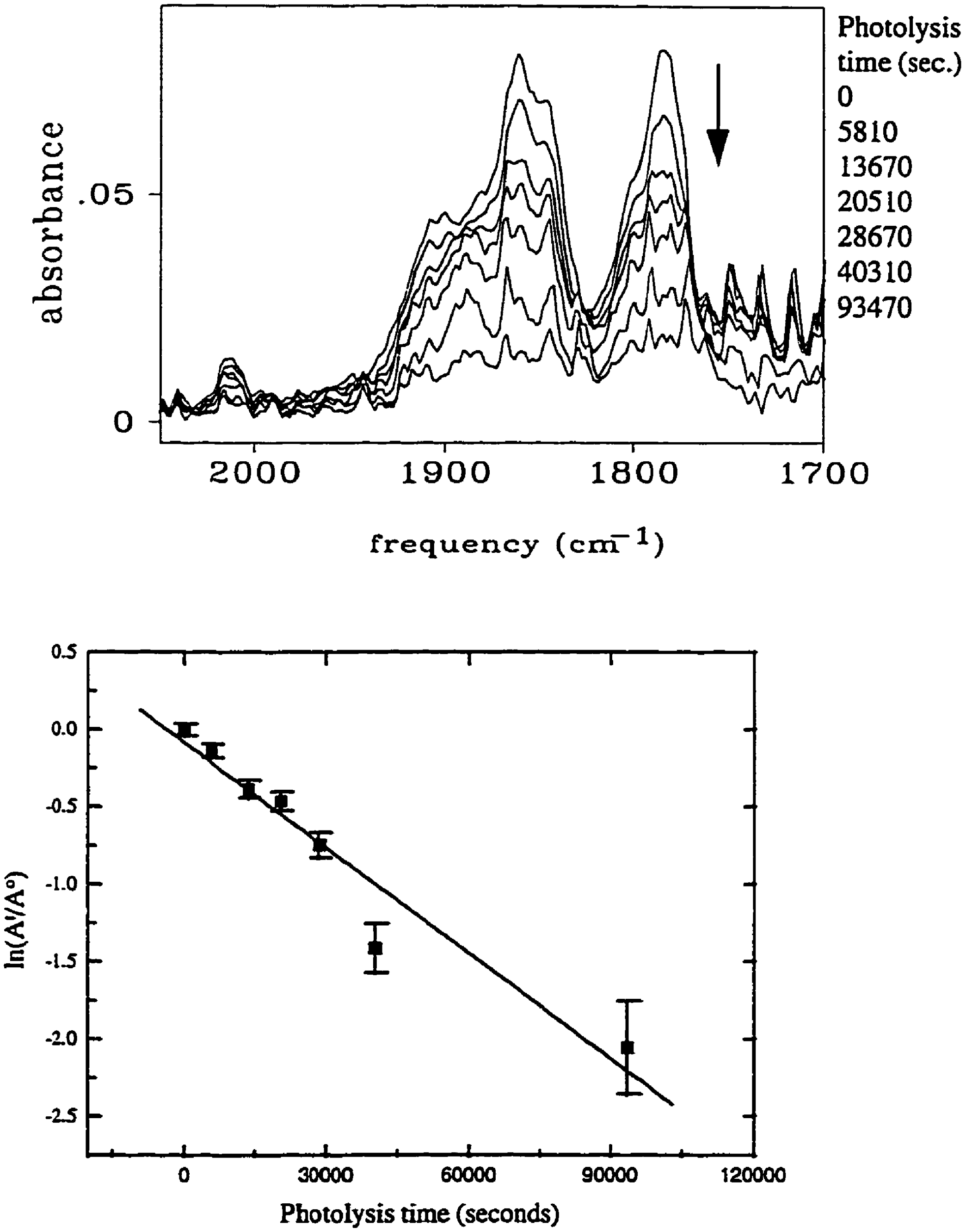

Figure 3.9 FTIR spectra associated with the photolysis of $Mo(CO)_4(Et_2\text{-en})$ and plots of $\ln(A^t/A^o)$ vs. photolysis time

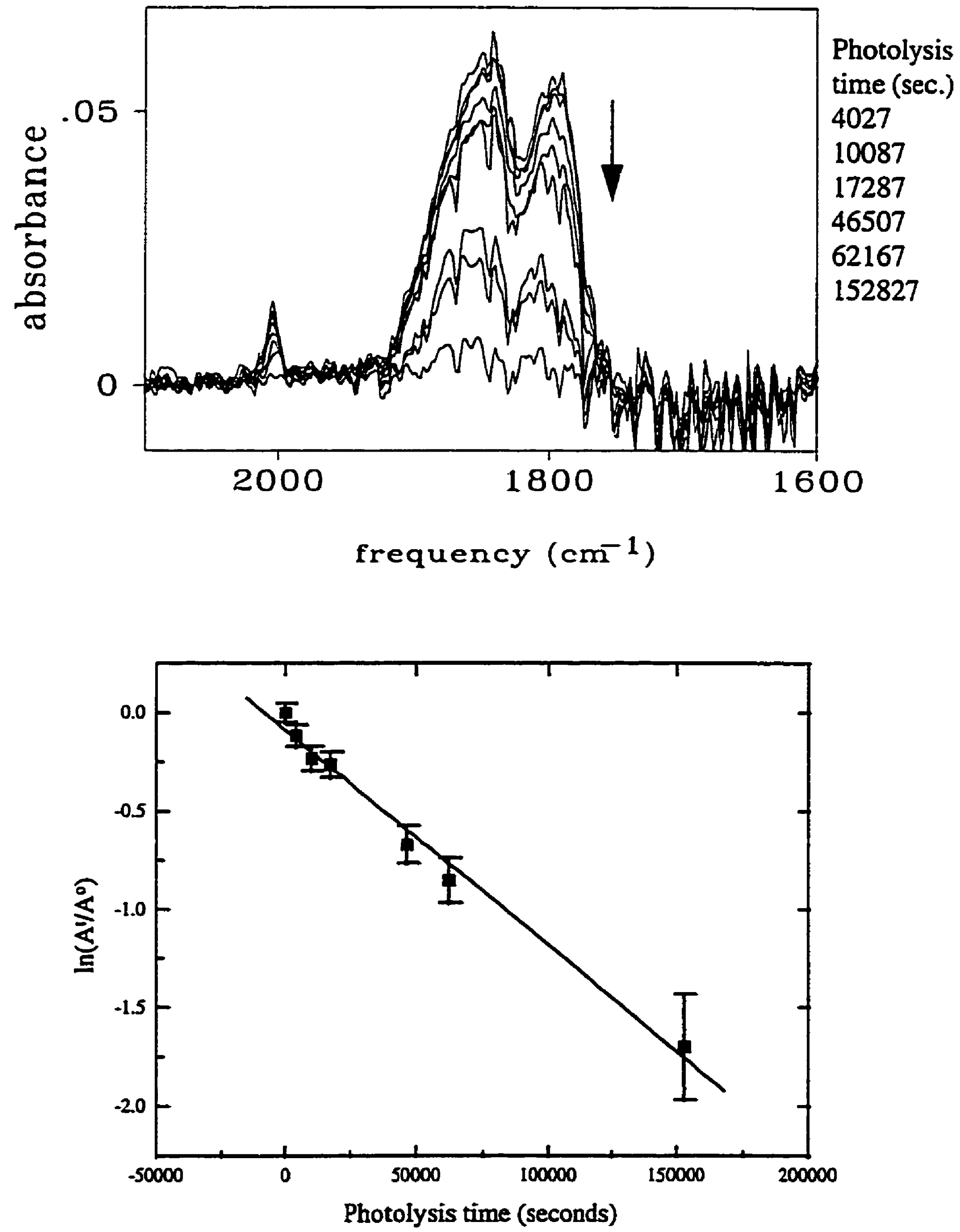

Figure 3.10 FTIR spectra associated with the photolysis of $W(CO)_4(Et_2\text{-en})$ and plots of $\ln(A^t/A^o)$ vs. photolysis time

The most efficient photochemical reaction amongst the chromium complexes is the reaction of $Cr(CO)_4(Et_2\text{-}en)$ whose quantum yield was found to be one order of magnitude larger than those of the other two chromium complexes. The quantum yield of $Mo(CO)_4(Et_2\text{-}en)$ was also found to be one order of magnitude larger than that of the $Mo(CO)_4(Me_2\text{-}en)$ complex. This is due to the different organic substituents on the nitrogen ligand. The ethyl group is usually assumed to have more electron withdrawing ability than methyl and hydrogen. For this reason, Et_2-en has the least capability to donate electrons to the metal. Since the bonding between the nitrogens and the metal is formed by the donation of electrons from the nitrogens to the metal, weaker M-N bonds allow a faster extrusion of the nitrogen ligands. It was mentioned previously that the lability of the M-N bond is largely enhanced at the excited state. This results in an extrusion of this ethylenediamine ligand. Hence, the highest quantum yield for the photodissociation of these metal complexes is the ones containing Et_2-en ligand. This supports the conclusion that the reaction occurs via Equation 3.2.

3.2.5 Auger spectroscopy

The resultant films from photolysis (as described above) were subjected to analysis by Auger electron spectroscopy. Films produced from $Cr(CO)_4(en)$ were found to be composed of chromium, oxygen, and carbon (see Table 3.4). No nitrogen was evident in the film, which is indicative of a loss of the nitrogen containing ligand from the surface. The carbon contaminations were, however, quite substantial in the films produced under vacuum. It has been reported that films are generally suffer from adventitious contaminations if they are not prepared under carefully controlled atmospheres [82]. For example, films would have carbon contaminations originated from pump oil if the experiment was conducted in instruments with oil diffusion pump [82]. Therefore, the carbon impurities found in the final films were assumed to be resulted from conducting the photolysis under vacuum. Photolysis of $Cr(CO)_4(en)$ was then operated in air in order to avoid the contaminations from the pump oil. The FTIR spectral changes of $Cr(CO)_4(en)$ irradiated in air were indistinguishable from those in Figure 3.5; however, Auger analysis presented a substantially different picture. Auger analysis indicated the formation of $Cr_{0.65}O$ with no contamination from carbon, except on the outer surface. This observation supported the proposed suggestions that the presence of carbon contaminations were originated from pump oil. The remaining complexes containing nitrogen donor ligans were irradiated in both air and vacuum to further examine whether or not the proposed carbon contamination source was valid. Carbon's were found in the films produced in vacuum for all remaining complexes. Pure films of molybdenum oxides and tungsten oxides were made in air and their compositions were found to be $Mo_{0.27}O$ and WO (see Table 3.4). The observation of the contamination free metal oxide films produced in air supported that the contamination source was the pump oil. These contamination free metal oxide films can therefore be used for the production of functional devices. The reported composition in Table 3.4 includes only the metals and the oxygen's because the carbon's have been assumed to be contaminations.

Table 3.4 **Auger analysis for the product film of $M(CO)_4(L\text{-}L)$ (M= Cr (L-L = en, Me_2-en, Et_2-en), Mo (L-L = Me_2-en, Et_2-en), W (L-L = Et_2-en))**

Precursor [condition]	Sputtering time (sec.)	N	C	Cr	O	Composition (moles)
$Cr(CO)_4(en)$ [vac]	0	0	0.54	0.18	0.28	$Cr_{0.65\pm0.05}O$
	5	0	0.48	0.21	0.31	$Cr_{0.68\pm0.05}O$
	20	0	0.43	0.24	0.33	$Cr_{0.74\pm0.05}O$
[air]	0	0	0.28	0.28	0.43	$Cr_{0.65\pm0.05}O$
	5	0	0	0.40	0.60	$Cr_{0.65\pm0.05}O$
	20	0	0	0.40	0.60	$Cr_{0.68\pm0.05}O$

Table 3.4 (continued)

$Cr(CO)_4(Me_2\text{-}en)$ [vac]	0	0	0.75	0.07	0.19	$Cr_{(0.35\pm0.03)}O$
	10	0	0.49	0.22	0.30	$Cr_{(0.72\pm0.05)}O$
	20	0	0.40	0.25	0.35	$Cr_{(0.73\pm0.05)}O$
[air]	0	0	0.28	0.28	0.43	$Cr_{(0.65\pm0.05)}O$
	5	0	0	0.40	0.60	$Cr_{(0.68\pm0.05)}O$
	20	0	0	0.41	0.59	$Cr_{(0.69\pm0.05)}O$
$Cr(CO)_4(Et_2\text{-}en)$ [vac]	0	0	0.51	0.14	0.35	$Cr_{(0.41\pm0.03)}O$
	5	0	0.37	0.25	0.38	$Cr_{(0.65\pm0.05)}O$
	15	0	0.24	0.33	0.43	$Cr_{(0.77\pm0.06)}O$
[air]	0	0	0.25	0.30	0.45	$Cr_{(0.65\pm0.05)}O$
	5	0	0	0.40	0.60	$Cr_{(0.65\pm0.05)}O$
	15	0	0	0.40	0.60	$Cr_{(0.65\pm0.05)}O$
$Mo(CO)_4(Me_2\text{-}en)$ [vac]	0	0	0.64	0.08	0.29	$Mo_{(0.26\pm0.02)}O$
	5	0	0.50	0.20	0.30	$Mo_{(0.68\pm0.05)}O$
	15	0	0.41	0.25	0.34	$Mo_{(0.74\pm0.05)}O$
[air]	0	0	0	0.26	0.37	$Mo_{(0.69\pm0.05)}O$
	5	0	0	0.57	0.74	$Mo_{(0.74\pm0.05)}O$
	15	0	0	0.56	0.79	$Mo_{(0.79\pm0.06)}O$

Table 3.4 (continued)

$Mo(CO)_4(Et_2\text{-en})$ [vac]	0	0	0.35	0.30	0.35	$Mo_{(0.85\pm0.06)}O$
	5	0	0.25	0.35	0.40	$Mo_{(0.87\pm0.06)}O$
	15	0	0.17	0.38	0.45	$Mo_{(0.85\pm0.06)}O$
[air]	0	0	0	0.20	0.80	$Mo_{(0.24\pm0.02)}O$
	5	0	0	0.23	0.77	$Mo_{(0.30\pm0.02)}O$
$W(CO)_4(Et_2\text{-en})$ [vac]	0	0	0.65	0.12	0.24	$W_{(0.51\pm0.04)}O$
	5	0	0.45	0.23	0.32	$W_{(0.73\pm0.05)}O$
	15	0	0.28	0.34	0.37	$W_{(0.92\pm0.07)}O$
[air]	0	0	0	0.37	0.63	$W_{(0.58\pm0.04)}O$
	5	0	0	0.54	0.46	$W_{(1.15\pm0.09)}O$
	15	0	0	0.47	0.53	$W_{(0.88\pm0.07)}O$

3.3 Conclusion

Metal oxide films of chromium, molybdenum and tungsten have been made via the room temperature photochemical process. These films produced from $M(CO)_4(L\text{-}L)$ M= Cr (L-L = en, Me_2-en, Et_2-en), Mo (L-L = Me_2-en, Et_2-en), W (L-L = Et_2-en) were found to be contamination free if photolysed in air. It was also found that ability of the compound to form an amorphous film upon spin coating depends on both the identity of metal and the ligands. All three chromium complexes, $Cr(CO)_4(en)$, $Cr(CO)_4(Me_2\text{-en})$ and $Cr(CO)_4(Et_2\text{-en})$, formed amorphous films; however, only $Mo(CO)_4(Me_2\text{-en})$, $Mo(CO)_4(Et_2\text{-en})$ and $W(CO)_4(Et_2\text{-en})$ formed amorphous films. Since the Et_2-en ligand is larger than either the Me_2-en or the en ligand, the symmetry of the complex is lower when its nitrogen ligand is the Et_2-en group. Lower symmetry of the complexes increases the possibility of forming randomly oriented amorphous films. Thus, the complexes containing the Et_2-en ligands were found to be the best candidate for forming an amorphous film. Solid state photochemistry only studied on the complexes formed amorphous films, because the ones formed crystalline films have difficulty inducing the photo-dissociation due to their high lattice energy.

All of the $M(CO)_4(L\text{-}L)$ complexes have approximate C_{2v} symmetry with four carbonyl stretching fundamentals: one B_1, one B_2 and two A_1 modes. Their stretching absorptions in the solid state were found to be at approximately the same energy as the ones found in solution. Hence, the difference in the organic substituents on the nitrogen as well as the differences in the metal centres did not influence the carbonyl stretching frequencies significantly. Owing to the similarity of the electronic absorption spectra in solution and in solid films, the absorption bands in solid state for all the complexes studied were assigned according to the ones found in solution.

The photochemistry of $M(CO)_4(L\text{-}L)$ (M= Cr (L-L = en, Me_2-en), Mo (L-L = Me_2-en, Et_2-en), W (L-L = Et_2-en)) as solid films has been explored. Their photochemical mechanism is similar and has been discussed using molecular orbital approach. It was concluded that the population of the ($a_2^2b_1^2a_1^2 \rightarrow a_2^2b_1^2a_1^1b_2^1$) level results in the enhancement of the labilization on one of the M-N bonds. For this reason, the dissociation occurs on the M-N bond. The overall photochemical reaction is the loss of all ligands leaving only metals on the substrate. Their photochemical process was found to proceed via a one photon process, and can be summarised as follows.

$$M(CO)_4(\eta^2\text{-}L\text{-}L) \xrightarrow{h\nu} M(CO)_4(\eta^1\text{-}L\text{-}L) \longrightarrow M + 4\,CO + L\text{-}L \qquad (3.2)$$

M= Cr, Mo, and W, L-L = en, Me_2-en, and Et_2-en

The first goal in this project has been achieved which is to eliminate the possibility of forming an intermediate after photolysis. It was mentioned previously that the presence of this intermediate slows down the photochemical process. Thus, the substitution of the poor π-acceptor nitrogen ligands on the metals for the phosphorus ligands has decreased the thermal stability of the intermediate. The quantum yields for all complexes have been measured and calculated according to Equation 1.4. The relative order of the quantum yields was found to be: $Cr(CO)_4(Et_2\text{-en}) > Cr(CO)_4(Me_2\text{-en}) \cong Cr(CO)_4(en)$ and

$Mo(CO)_4(Et_2\text{-}en) > Mo(CO)_4(Me_2\text{-}en)$. The difference arose from the electron donating ability of the organic substituents on the nitrogen ligand.

There was no detectable nitrogen or carbon contamination inside the metal oxide films produced in air. Therefore, all the photo-extruded ligands diffused out of the films after photolysis. To substitute a lighter ethylenediamine ligand with higher vapour pressure for the heavier phosphorus ligand with lower vapour pressure has solved the purity problem associated with the PPh_3 ligand in the final film. The films produced in vacuum were found to contain carbon; however, the ones produced in air were carbon free. This was assumed to due to the film produced in vacuum was contaminated by the hydrocarbons from the pump oil, and the ones produced in air was reacted with the oxygen in the air to form metal oxides without contaminations from the vacuum pump.

Contamination free metal oxide films of chromium, molybdenum and tungsten have been deposited via the efficient photochemical process. More complicated materials should be able to be produced via the same method. Since deposition of the precursor film is accomplished by spin coating, it should be possible to co-deposit mixture of different metals. This may be achieved by spin coating with a solution containing two or more precursors. If the photochemistry is unaffected by the presence of other compounds then the deposition of mixed metal oxides should be achieved via this method. Having produced pure metal oxide films with high efficiency, the next step is to fabricate metal oxide sensors via this efficient photochemical process. The next chapter will be devoted to the fabrication of these sensor materials and the design of the reactor for testing them. Both sensors constructed from single metal oxide as well as mixed metal oxides will be reported and discussed in Chapters 4 and 5, respectively.

3.4 Experimental

The organometallic complexes $M(CO)_4(LL)$ (M= Cr, Mo, W; LL= $H(CH_3)NCH_2CH_2NH(CH_3)$ ≡ (Me_2-en), $H_2NCH_2CH_2N(C_2H_5)_2$ ≡ (Et_2-en), $H_2NCH_2CH_2NH_2$ ≡ (en)) were synthesised by literature methods [79]. All these complexes are yellow and were characterised by FTIR spectroscopy, and elemental analysis (see Table 3.5). Please refer to the experimental section in Chapter 2 for the calibration of absorption on surface and the photolysis of complexes as films on silicon surfaces.

Table 3.5 Elemental analysis of M(CO)$_4$(L-L) (M= Cr, Mo, W and L-L = en, Me$_2$-en Et$_2$-en)

complex	% C	% H	% N	
Cr(CO)$_4$(en)	32.15	3.59	12.50	calculation
	32.00	3.85	12.34	found
Cr(CO)$_4$(Me$_2$-en)	38.10	4.60	11.11	calculation
	38.40	5.01	11.03	found
Cr(CO)$_4$(Et$_2$-en)	42.86	5.75	9.99	calculation
	41.35	5.74	9.59	found
Mo(CO)$_4$(en)	26.88	3.01	10.45	calculation
	26.70	2.99	10.40	found
Mo(CO)$_4$(Me$_2$-en)	32.40	4.08	9.46	calculation
	32.14	4.20	9.50	found
Mo(CO)$_4$(Et$_2$-en)	37.00	4.97	8.64	calculation
	37.10	4.98	8.60	found
W(CO)$_4$(en)	20.24	2.27	7.87	calculation
	20.20	2.25	7.85	found
W(CO)$_4$(Me$_2$-en)	25.02	3.15	7.29	calculation
	24.99	3.05	7.05	found
W(CO)$_4$(Et$_2$-en)	29.15	3.91	6.80	calculation
	29.00	3.89	6.70	found

CHAPTER 4

Amorphous WO_3 based sensors made photochemically for detecting sub-ppm NO_x

4.1 Introduction

It has been reported in Section 1.7 that there are three air pollutants of nitrogen oxides released from automobile exhausts usually referred as NO_x (NO, NO_2, N_2O) [61]. NO converts to NO_2 with the presence of sun light, and NO_2 converts to NO with the presence of ozone [1]. Although, most modern cars have been equipped with a catalytic converter which decomposes NOx to N_2 and O_2, a large amount of NO_x is still released into the atmosphere [83]. NO_x sensors are therefore needed for air quality, emission and industrial process control. In addition, because NO_x is highly toxic, the sensitivity required for detection is less than 1 ppm [1]. For this reason, highly sensitive NO_x sensors were planned to be fabricated to be monitored in daily life. Since in a normal day, the concentration of ozone as well as the intensity of sun light varies, from the practical point of view, it is best to be able to fabricate sensors that can detect various concentrations of NO_x (NO to NO_2 ratio depends on the concentration of ozone and the intensity of light) [1]. In early days, tungsten oxides have been reported to show response to nitrogen oxides; however, they were also reported to be lacking reproducibility and with poor sensitivity [84]. Only recently, with the improvement on the fabrication technology, tungsten oxides were re-investigated and were reported to show higher sensitivity to nitrogen oxides [33-39]. However, not only the properties of these tungsten oxides varied with the preparation methods as well as the types of sensor devices, but also these sensors suffered from long response time as well as costly and complicate preparation method. Therefore, an improvement on the fabrication process of tungsten oxides as well as the design of a better sensor device was desirable. Since tungsten oxides have been produced via the efficient room temperature photochemical process with $W(CO)_4(Et_2\text{-en})$ as precursor (see Chapter 3), this precursors as well as the process was used to fabricate sensor devices. Tungsten oxides were not deposited on silicon substrates, instead, they were deposited on devices with interdigitated metal electrodes. The interdigitated type of devices were designed to use as substrate, because the current of the device increased if the electrode-material-electrode sandwich was connected in series. Moreover, if the fabricated tungsten oxides via the room temperature photochemical process showed response to nitrogen oxides, then the sensitivity would increase since the interdigitated devices contained lots of small sensors (electrode-sensing material-electrode) connected in series. Hence, a comb shaped structure (the interdigitated structure) was designed using a computer aided drawing tool to produce a defined width, length, and spacing of the electrodes accurately. An oven system was designed to monitor the sensor. Since the properties of tungsten oxides varied with the preparation methods, it remained unclear whether or not tungsten oxides produced via the room temperature photochemical process would respond to nitrogen oxides. Therefore, the fabricated tungsten oxides on interdigitated electrodes were tested to see whether they can respond to the presence of nitrogen oxides. Moreover, a systematic study on the sensor devices by varying the applied voltages, the temperatures, the thicknesses of the thin films, and the concentrations of nitrogen oxides was needed to be carried out in order to identify the optimised bias voltages, temperatures and the thicknesses of the sensor. A sensing mechanism was suggested according to the properties of the materials and the changes of the conductivity of the sensor devices. This sensing mechanism suggested can only serve as a qualitative interpretation, because this study was directed to the design and fabrication of sensor devices as well as looking for the optimised operation temperatures, thicknesses and applied biases for the sensor. A detailed mechanistic study needed to be performed with a few more spectroscopic characterisation which are described in Chapter 6.

This chapter is divided into six main sections. The first section describes the design of both the interdigitated aluminium devices and the gas chamber. The aluminium devices were made as substrates for the deposition of the sensing material, and the gas chamber was built for testing the performance of the sensors. In the second section, the fabrication sequences for making the interdigitated devices and the sensor devices are shown. A general fabrication sequence for the production of metal oxide films is illustrated in Figure 1.5. In the third section, the characterisation of the material of these sensors is discussed. Although this sensing material, tungsten oxide, has been discussed in Chapter 3, there are some additional details which are presented in this chapter. In the next section, the electrical characterisation of the sensors and the determination of their electron transport mechanism is discussed. Finally, the response of these metal oxide sensors at various operating temperatures to different concentrations of NO_x were reported. They were found to respond to less than 1 ppm of NO_x at ~200°C

4.2 Design

4.2.1 Mask design

A device with electrodes is required in order to measure the electrical properties of the tungsten oxide based sensing element. One way of measuring the conductivity of the sensing material is by depositing it between two electrodes, and determining the current through the material under an applied bias voltage. Since the current of the device increases if the electrode-material-electrode sandwich is connected in series, a comb shaped structure was designed (see Figure 4.1). The black lines in Figure 4.1 will be aluminium electrodes on the actual device while sensing material will be deposited in between these electrodes. The measurement will be conducted by probing the two square pads.

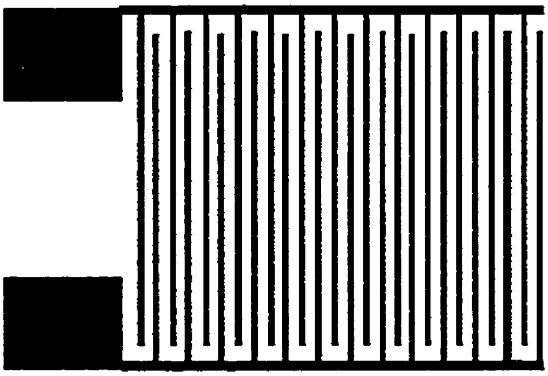

Figure 4.1 Interdigitated pattern for producing the mask

This pattern has a length of 1160 μm while the width of the electrodes and the spacing between the electrodes are both 15 μm. The pattern was designed using *drafix* (a computer aided design tool) in order to define the width, length and spacing of the electrodes as well as the size of the device accurately. Since the fabrication method used for the production of the devices involves standard lithographic techniques, a mask with the desired features is required in these techniques to produce devices. The lithographic sequence will be described in the fabrication section 4.3.1. In any case, after the pattern has been produced in the computer, the design is printed onto an acetate paper. This paper is used as a negative to develop photoplates (masks) in the darkroom. In doing so, identical patterns are transferred to the mask. The size of a single device is 2 x 3 mm^2, and there are 500 device patterns on one mask (10 x 10 cm^2).

4.2.2 Design of the oven system

An oven system was designed to provide an environment to monitor the sensor. The system provided the following features: a temperature control, a flow control system and access for electrical probes for the measurement of conductivity. The oven system was designed to meet all the requirements mentioned above (see Figure 4.2). The base of the oven was constructed from a 7 x 4 x 5 cm^3 aluminium block. There are two cylindrical holes for the heat cartridge and the thermocouple. The main chamber is for the socket which is made from a machinable ceramic and designed to fit a 24 pin ceramic package. There are two holes on each side of the oven for gas to flow through. The flow controller is connected to the gas inlet by copper pipes.

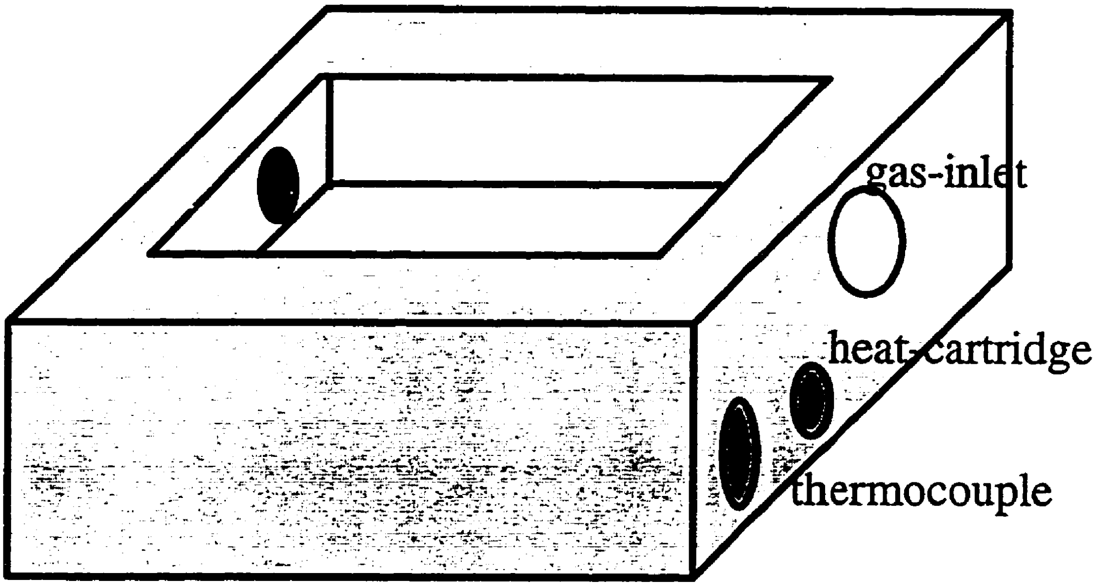

Figure 4.2 Oven control system

4.3 Fabrication

4.3.1 Fabrication of interdigitated devices

A standard photolithographic technique was used for the production of devices. As the initial step in the fabrication process, the wafers were subjected to standard RCA cleaning. Figure 4.3 illustrates the fabrication sequence. After inspection for cleanliness, wafers were placed in the furnace in order to grow a 5 µm oxide layer for electrical insulation. A layer of aluminium was then sputtered onto the silicon dioxide. A photoresist was spin cast onto the silicon wafer, and then the wafers were transferred to the mask aligner for contact printing. The exposed area was developed and rinsed away when a positive photoresist was used. The unwanted aluminium portion was then etched with aluminium etchant. Finally, the remaining photoresist was removed by acetone and leaving the aluminium electrodes on the silicon dioxide.

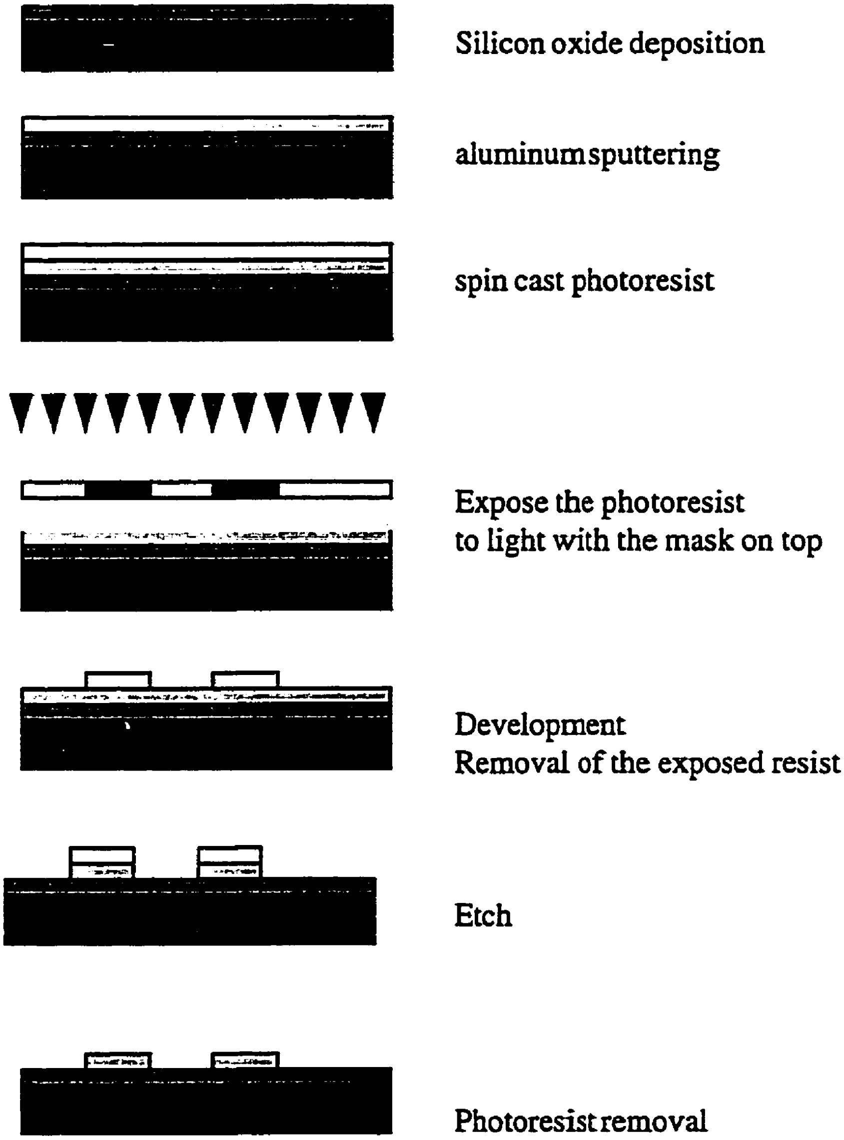

Figure 4.3 Fabrication scheme for interdigitated aluminum on silicon

4.3.2 Fabrication of the sensor devices

A general fabrication of the sensor devices via the room temperature photochemical process is illustrated in Figure 4.4. A known amount of CH_2Cl_2 precursor solution containing $W(CO)_4(Et_2\text{-}en)$ was placed onto a spinning interdigitated device to make an amorphous film. The fabrication of the interdigitated device has been described in the previous section (4.3.1). The metal oxide sensor was made by exposing the precursor device to a 254 nm UV lamp for a specific time. Films of different thicknesses were made by repeating the coating and photolysing procedures several times to obtain the required thickness. Polycrystalline films were produced by annealing the photolysed films at 500°C in air for two hours.

4.4 Measurement of electrical properties of sensors

In this section, the general measurement scheme is presented (see Figure 4.5). The sensor device is plugged into the 24-pin ceramic socket which is connected to the voltmeter and the power supply. The socket is inside the oven where the temperature can be adjusted. The current-voltage characteristics were measured in the temperature range from 17°C to 350°C. A known amount of NO_x was injected into the air hose under conditions of constant voltages and flow rates. The conductivity change with respect to the various concentrations of NO_x was monitored at different temperatures.

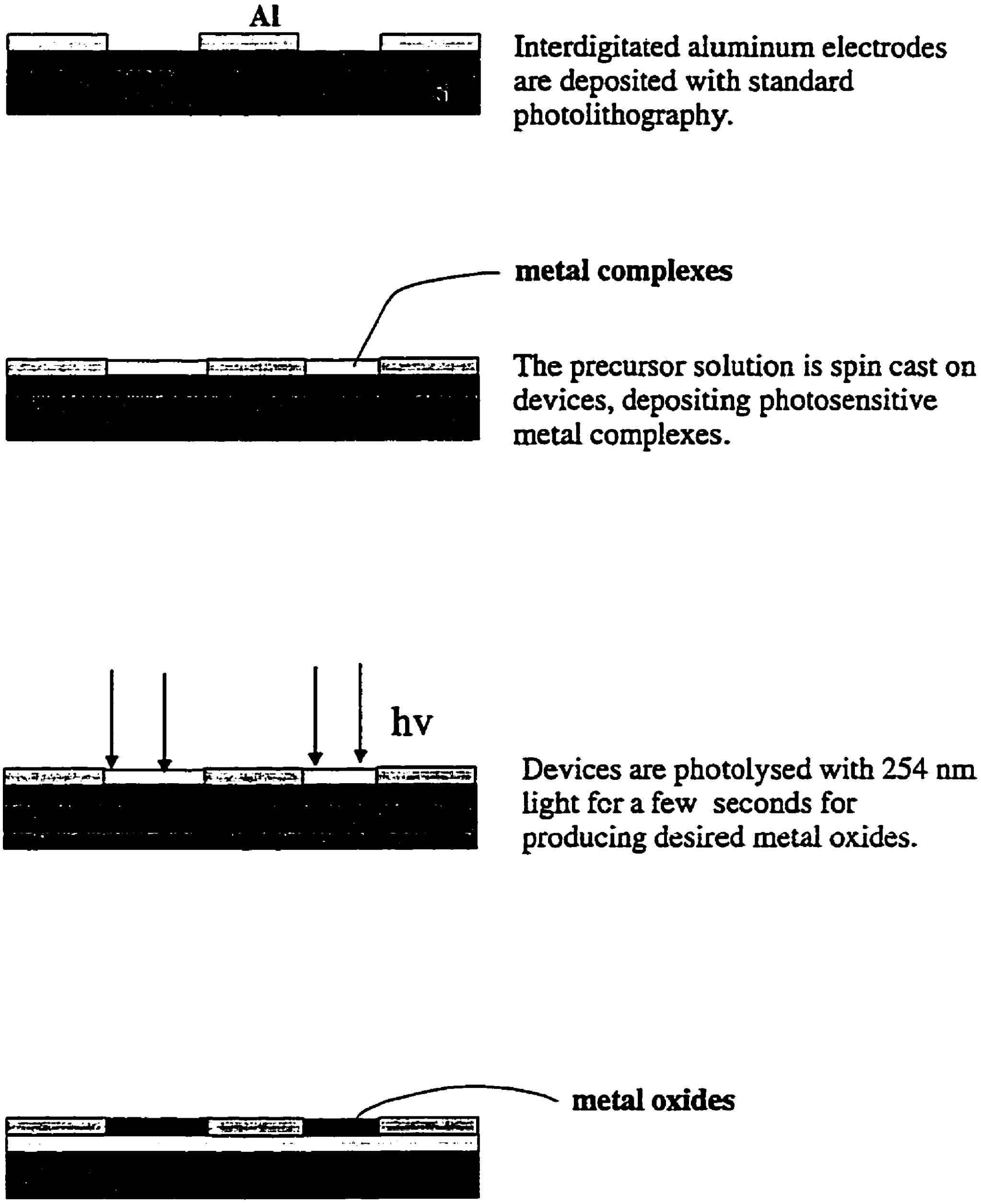

Interdigitated aluminum electrodes are deposited with standard photolithography.

The precursor solution is spin cast on devices, depositing photosensitive metal complexes.

Devices are photolysed with 254 nm light for a few seconds for producing desired metal oxides.

Figure 4.4 Fabrication sequence for the production of metal oxide thin film devices

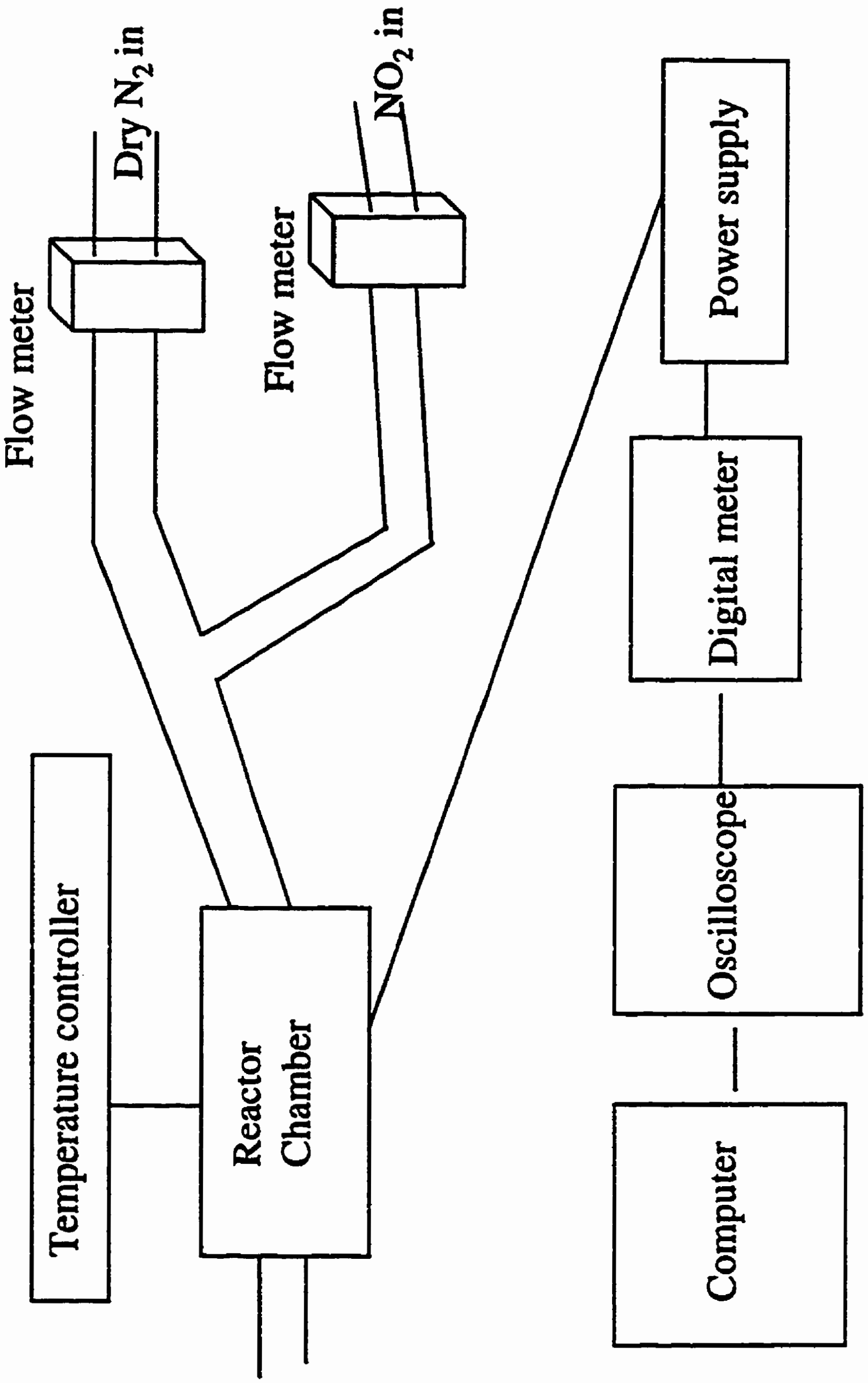

Figure 4.5 Scheme of the experimental design

4.5 Results and Discussion

4.5.1 Materials characterisation

The syntheses and general processes for making the amorphous films of $W(CO)_4(Et_2\text{-en})$ have previously been described in Chapter 3. The processes for producing the films with required thickness have been modified slightly and are presented in this section. In order to improve the efficiency of the fabrication, the light source was changed from a 366 nm UV lamp with 3.0 mW/cm^2 output to a 254 nm UV lamp with 70.0 mW/cm^2 output. A saturated solution of $W(CO)_4(Et_2\text{-en})$ in CH_2Cl_2 was made and filtered. This precursor solution was spin cast onto the comb-shaped device to form an amorphous film. Another amorphous film was deposited on a silicon substrate with no electrodes under identical conditions for reference. The precursor film photochemistry (under the output of a 254 nm UV lamp) was monitored with the FTIR spectrometer only on the film deposited on the no electrode substrate because the highly conducting electrodes scatter photons. Figure 4.6 shows the changes in the infrared spectra of the precursor film upon irradiation under 254 nm UV lamp in air. It can be seen from the spectra that no absorbance bands consistent with the starting materials were observed after 5 seconds. This reflects that the starting materials reacted within 5 seconds, and the photoproducts reacted with oxygen in air to form stable metal oxides.

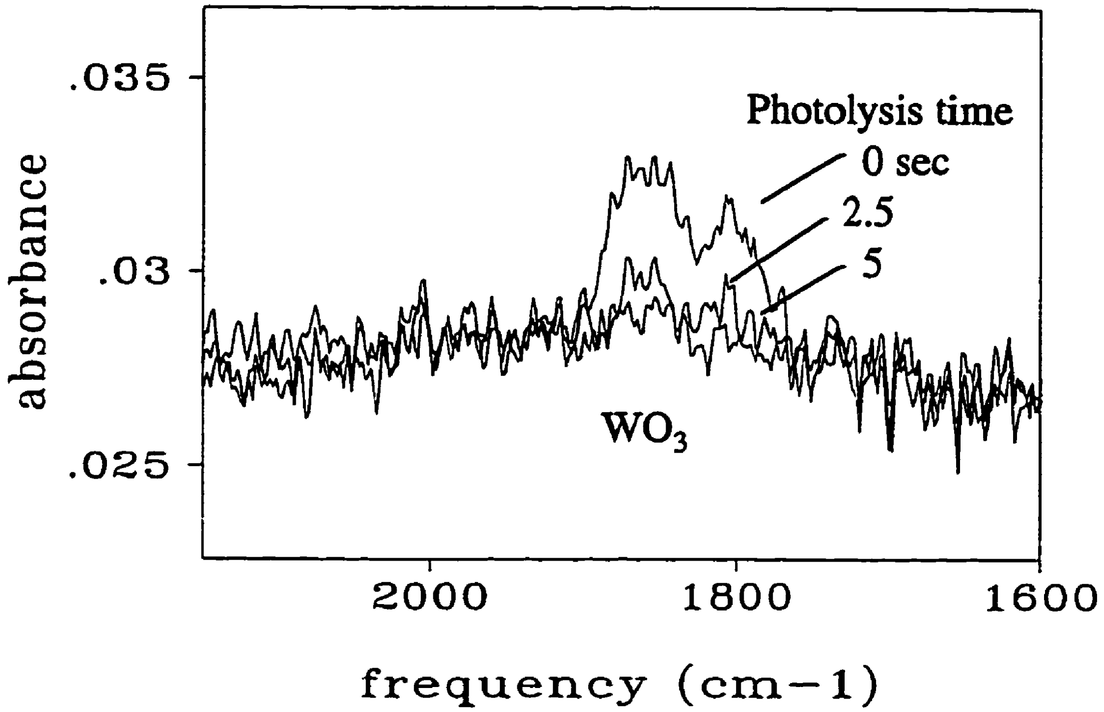

Figure 4.6 FTIR spectra associated with the photolysis of $W(CO)_4(Et_2\text{-}en)$ as a surface film on silicon at room temperature

The photoproduced film was transferred to the Auger electron spectrometer in order to determine the composition (see Table 4.1). The average composition of the film was found to be $WO_{2.0}$. In some devices, the amorphous film was annealed at 500°C for 2 hours in air to form the polycrystalline film whose composition was analysed by Auger electron spectroscopy to be $WO_{2.6}$ (see Table 4.1). The oxygen content in the amorphous films is lower than in the polycrystalline films. This oxygen deficiency has profound effects on the conductivity of the device [59-60, 62, 85, 86].

Table 4.1 Auger analysis of films produced by the photolysis films of $W(CO)_4(Et_2\text{-en})$ with 254 nm light

Precursor film	sputter time(sec.)	W	O	composition(calc.)
amorphous	0	0.28	0.72	$WO_{(2.6 \pm 0.04)}$
	5	0.41	0.59	$WO_{(1.45 \pm 0.05)}$
	10	0.34	0.66	$WO_{(1.96 \pm 0.07)}$
polycrystalline	0	0.24	0.76	$WO_{(3.1 \pm 0.04)}$
	10	0.28	0.71	$WO_{(2.5 \pm 0.09)}$
	30	0.30	0.70	$WO_{(2.3 \pm 0.07)}$

4.5.2 Structural characterisation

The amorphous film deposited on silicon chip with no electrodes was transferred to the X-ray diffraction spectrometer. The XRD patterns of the as-deposited film of tungsten oxides shows no reflection peaks, which indicates that the films are amorphous (see Figure 4.7). After annealing of an amorphous film, the XRD spectrum of the resultant film was recorded (see Figure 4.7). There are two peaks present after annealing indicated the formation of a crystal. The peak centred at $2\theta = 44.37°$ had been interpreted to correspond to the reflection from the (211) plane of WO_3, and the one at $2\theta = 37.64°$ is the reflection from the (210) plane of WO_3 [86].

The lattice structure of WO_3 is known to be the ReO_3 type as mentioned previously [86, 87]. Figure 4.8 illustrates the lattice structure of WO_3, where each tungsten atom is connected to six oxygens and each oxygen is shared by two tungsten atoms. A simplified band structure for WO_3 is shown beside the lattice structure in Figure 4.8. The π, π^*, σ, and σ^* molecular orbitals are formed from the combination of the p-orbitals on oxygen and d-orbitals on the metal. Since tungsten (in the oxidation state six) donates all six d-electrons to the oxygens surrounding it, there are no electrons remaining to occupy the π^* orbital. The band gap separates the π and π^* orbitals. The analysis from the Auger electron spectra indicates that there were some oxygen defect sites in the material. In the case of a oxygen defect, not all of the d-electrons are transferred to oxygen. Figure 4.9 illustrates the vacant oxygen site in the WO_3.

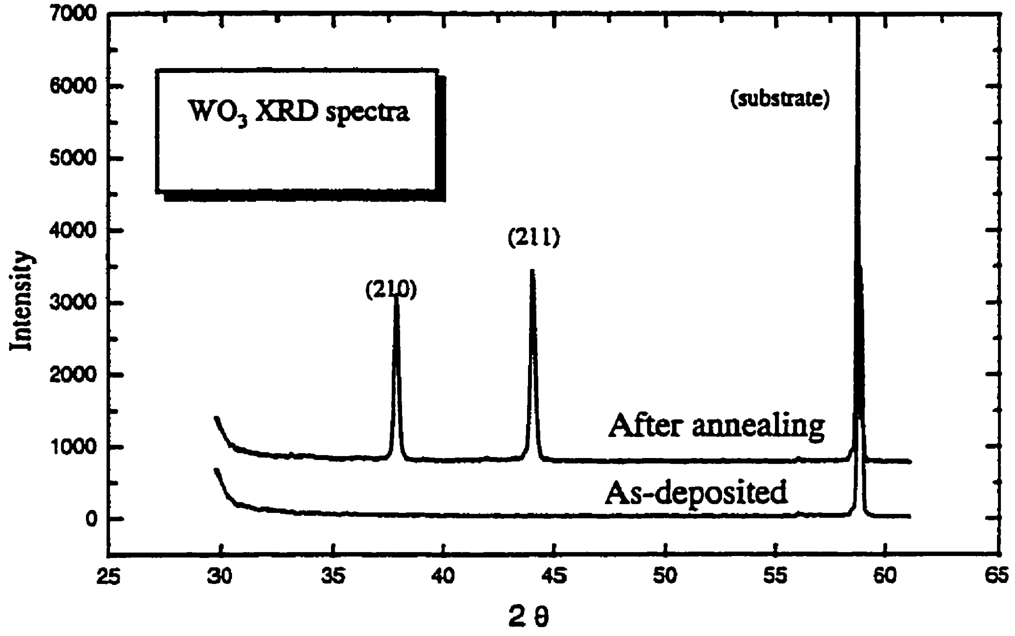

Figure 4.7 XRD pattern of the as-deposited and annealed WO$_3$ after 500°C

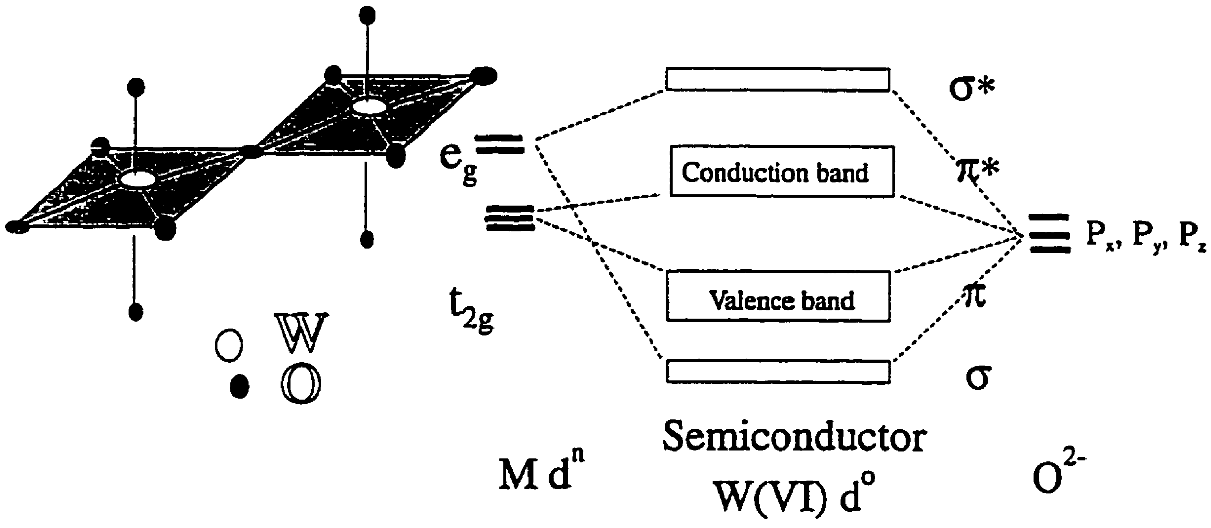

Figure 4.8 The lattice and band structure of WO_3

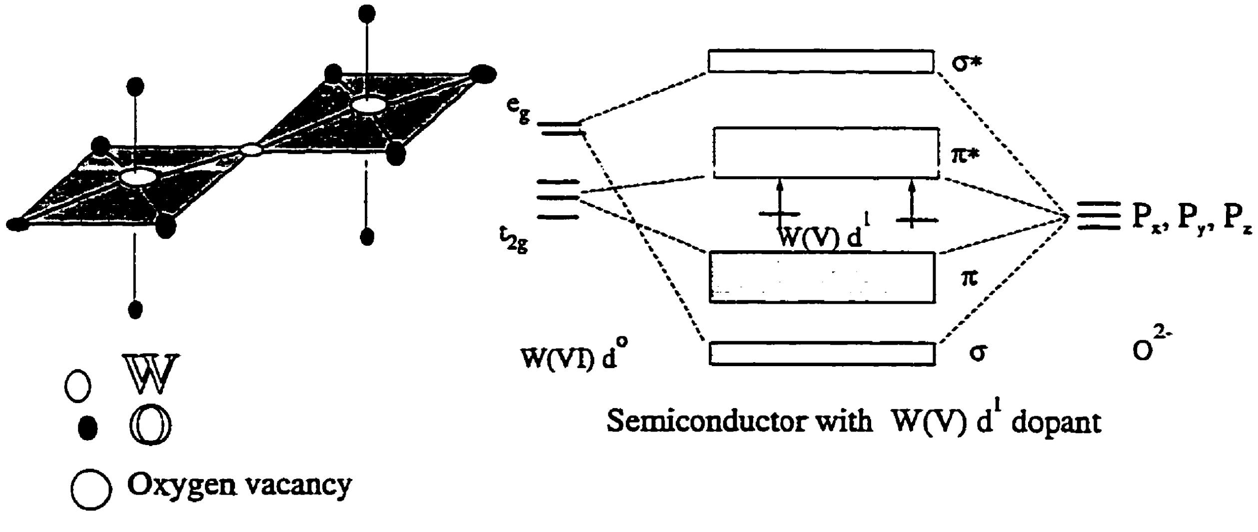

Figure 4.9 The lattice and band structure of doped WO_3

The band structure for WO_3 with W(V) dopants is also shown beside the lattice structure in Figure 4.9. The electrons in the W(V) occupy states within the band gap. At temperatures above 0 K, these electrons may occupy the conduction band and become the majority carriers. This interpretation is supported by examining the WO_3 film using the hot-probe method which indicated that it was a n-type semiconductor [95].

4.5.3 Electrical characteristics

4.5.3.1 The current-voltage behaviour of amorphous WO_3 films

Metal oxide devices were fabricated by depositing and photolysing the precursor films on the interdigitated electrodes. The electrical properties of the Al-WO_3-Al sensor can therefore be measured by electrical probing with the aluminum electrodes. The general method of fabrication was described in Section 4.3. Different thicknesses of WO_3 films may result in different resistances and hence different sensitivity to the surroundings. Therefore, the WO_3 films of 250 and 500 nm thickness have been deposited between the 500 nm thickness aluminum electrodes. The films were examined under microscope and assumed to be uniform. The conductivities of these sensors have been measured at various temperatures, and monitored periodically for a year. It was found that the conductivities of the sensors stayed constant for that period of time. The current of the 500 nm thick WO_3 film was measured from an applied bias of 0 to 20 V and temperature of 223°C to 293°C. I-V curves for this device are illustrated in Figure 4.10. The current of the sensors increased with increasing voltages and temperatures.

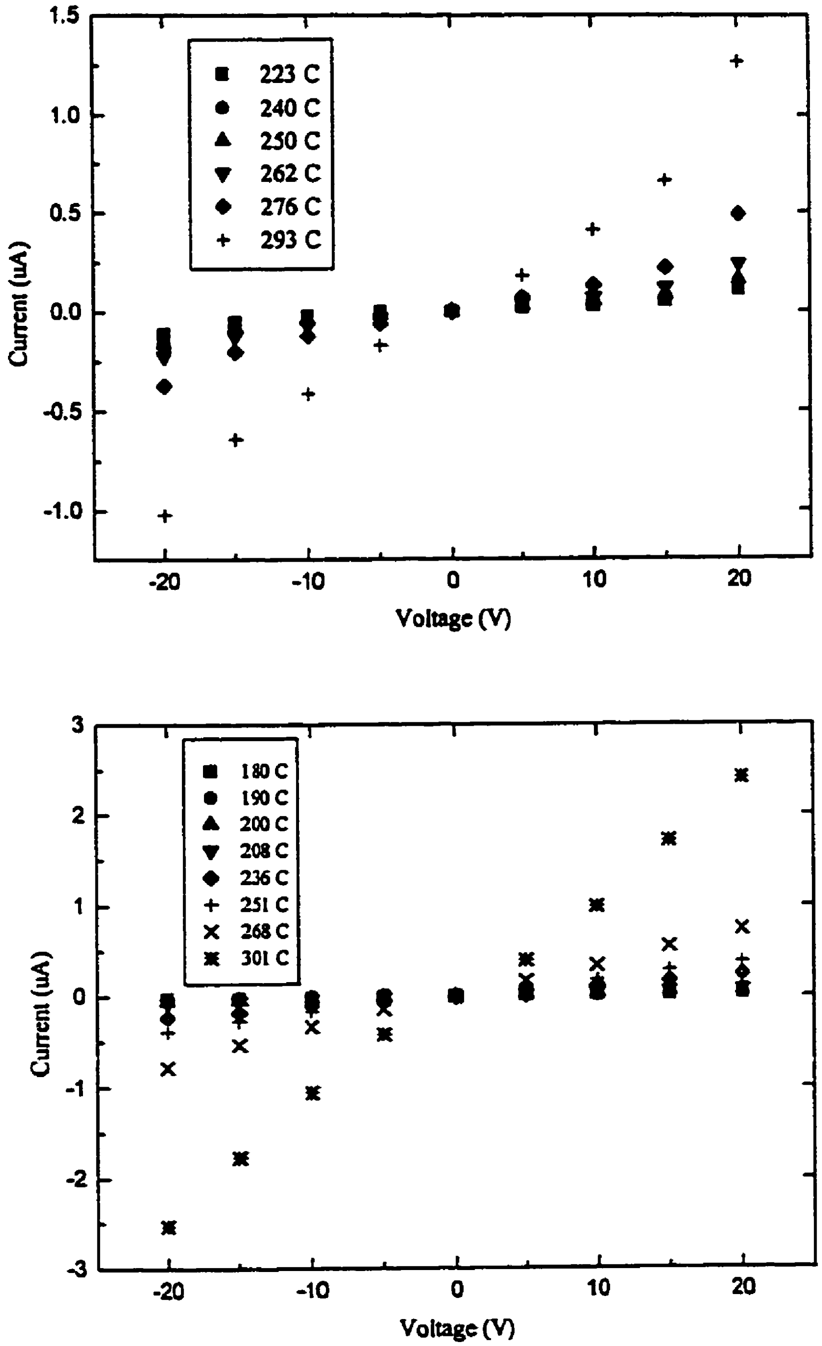

Figure 4.10 IV characteristics of devices based on amorphous WO_3 of 250 and 500 nm thickness

The I-V curves measured at different temperatures for the 250 nm thick amorphous WO_3 film are also illustrated in Figure 4.10. The current of the films also increased with increasing temperatures and voltages. Furthermore, the resistance of the 250 nm thick material was found to be higher than that of the 500 nm thick films. This relationship can be interpreted by the Equation 1.7: $\rho = ZV/Il$, where ρ is the resistivity, l is the distance between the two points at which the voltage is measured and Z is the cross-sectional area perpendicular to the direction of the current. Since the resistivity is independent of specimen geometry, a reduction in the thickness of the film results in an increase in its resistance. The conductivity of both devices was found to be sensitive to the operating temperatures. Their resistance decreased with increasing temperatures. Because of instrumental limitations on the multi-meter, the current of the sensor could not be obtained at lower voltage ranges when the temperature was below 180°C for the 500 nm thick material, and 223°C for the 250 nm thick material.

4.5.3.2 Current-voltage behaviour of 250 and 500 nm thick polycrystalline WO_3 films

The conductivities of the polycrystalline films at different thicknesses have been measured at various temperatures (see Figure 4.11). The current-voltage relationship for these films did not follow Ohm's law. Instead, the current increased exponentially with increasing bias. The resistance of the 500 nm thick films was lower than that of the 250 nm thick films.

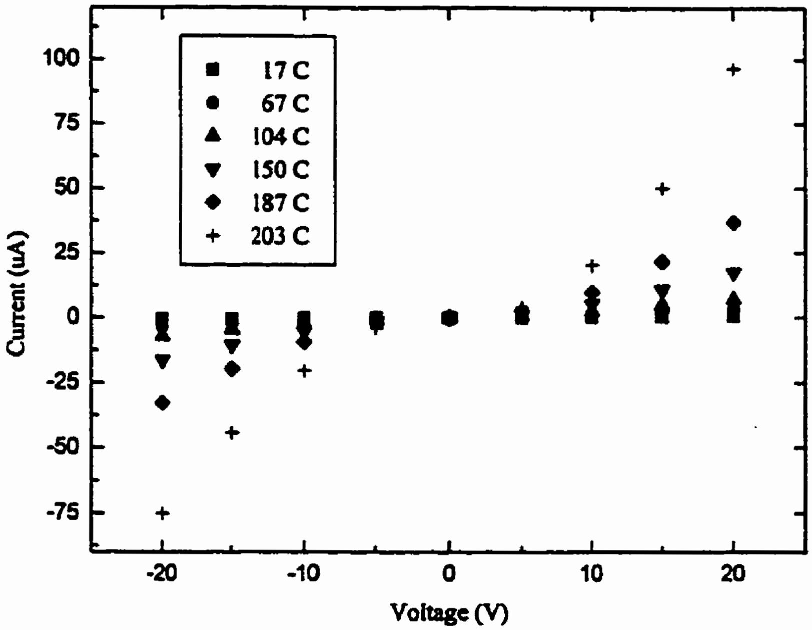

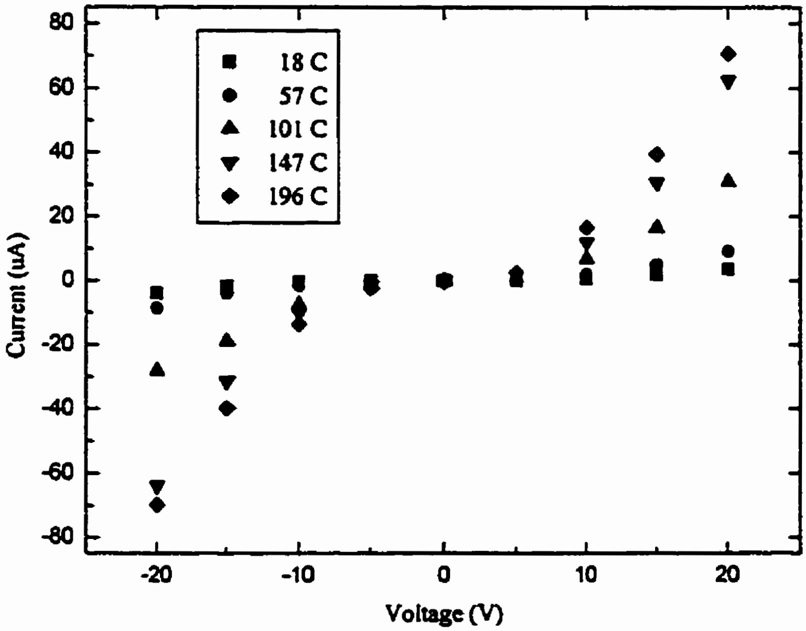

Figure 4.11 IV characteristics of devices based on polycrystalline WO_3 of 250 and 500 nm thickness

This agrees with the relationship defined by Equation 1.5, where an increase in resistance of the film was due to a reduction in its thickness. The conductivity of the devices was very sensitive to the operating temperatures, and was found to increase with increasing temperatures. The resistance of the polycrystalline films was lower than those of the amorphous ones. The difference arose from the heat treatment that the polycrystalline devices underwent. The amorphous films were crystallised after being annealing at 500°C for two hours [88].

4.5.3.3 Electron transport in amorphous materials

The measurements of the current-voltage characteristics of the amorphous films indicate that the current is very sensitive to applied voltages and temperatures. In order to accurately determine the electron transport mechanism in amorphous solids, there are three transport mechanisms which must be considered: variable-range hopping conduction, single electron hopping conduction, and ohmic conduction [57, 88]. The electrical data were fitted into three equations representing the three types of electron transport. The best fit of the three equations determined the transport mechanism for the electrons in amorphous films. Variable range hopping conduction usually takes place when there is a relatively high density of localised or defect states in the energy gap. Figure 4.12 illustrates the possible defect states in the energy gap. If there is an electron with enough energy to move from the initial state to either A or B state through hopping conduction, then the mechanism for the current transport is that of variable range hopping.

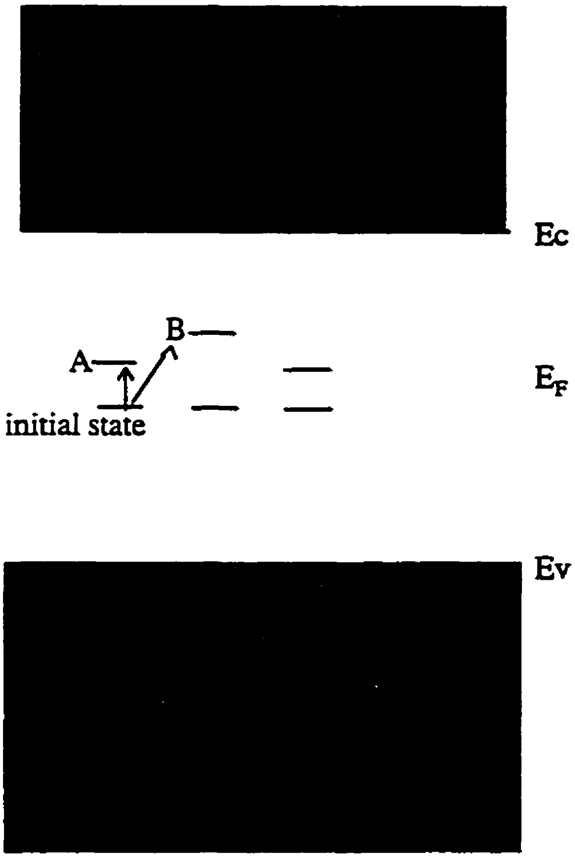

Figure 4.12 Illustration of variable range hopping transport, where A and B are two possible final states for an electron with excess energy to move to.

When variable range hopping conduction takes place, there is more than one barrier height between the potential initial and final states. It is therefore impossible to determine them individually. The equation for variable range hopping conduction is as follows [89]:

$$\sigma = \sigma_0 \, \mathrm{EXP}(- \alpha T^{-1/4}) \qquad (4.1)$$

where σ is the conductivity of the material, σ_0 and α are constants, and T is the temperature. The conductivity can be substituted by the conductance G, since G is linearly proportional to conductivity. Therefore,

$$G = Go \, \mathrm{EXP}(- \alpha T^{-1/4}) \qquad (4.2)$$

A straight line with a slope of ln(Go) and intercept of α should be obtained, if G is plotted against $T^{-1/4}$.

If the electron moves through the solid via a fixed barrier and a fixed hopping distance, then the transport mechanism is single electron conduction. In the case of single electron transport, there is only one accessible localised state in the energy gap and a single barrier height can therefore be determined. The equation used for single electron hopping conduction is

$$J_h = J_o \, \mathrm{EXP}(-Ea/kT) \qquad (4.3)$$

where J_h is the current density multiplied by the temperature, Ea is the activation energy, T is the temperature, and k is Boltzman's constant [90]. Since there is only one accessible final energy state for the electron, the activation energy can therefore be calculated. If ln(J) is plotted against 1/kT, then the slope is the barrier height between the initial and the final state.

It is possible that the electron transport follows ohmic conduction. The equation for ohmic conduction is:

$$J = F\,\mathrm{EXP}(-Ea/kT) \tag{4.4}$$

where J is the current density, F is the electric field, and Ea is the activation energy.

The current-voltage information (taken at different temperatures) of the 500 nm thick amorphous WO_3 films was fitted to equations 4.2 - 4.4. These three fitted curves are shown in Figure 4.13. The slopes and intercepts of the fitted lines are tabulated in Table 4.2. In order to determine which mechanism best fits the data, both the graphs and the data must be further examined. The first graph in Figure 4.13 illustrates the fitting for single electron transport. If single electron hopping transport is the mechanism for conduction, then the barrier height of conduction will be given by the slope of the fitted line. Since there is only one barrier height, the calculated barrier heights reported in Table 4.2 should approximately be the same. However, the calculated slopes were found to be very different from each other. Therefore, it is unlikely that electrons follow the single electron hopping mechanism. The second graph shows the fit to ohmic conduction. If ohmic conduction is the mechanism for electron flow in the 500 nm thick films, then these four lines should be approximately parallel to each other. The slopes of these fitted lines reported in Table 4.2 show that the activation energies (slopes of the lines) were very different from each other. Therefore, the possibility of the electron conduction via ohmic conduction transport can be eliminated.

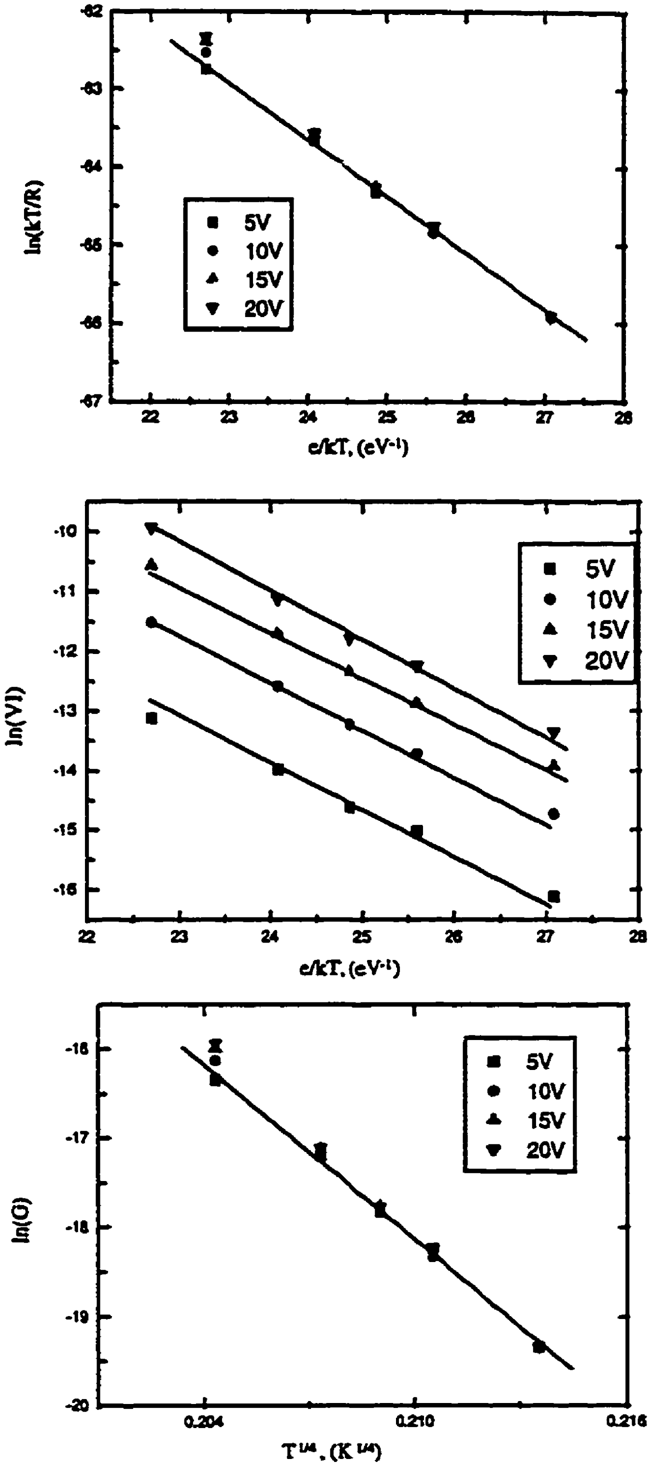

Figure 4.13 Plots of ln(kT/R) vs. (e/kT) for single electron hopping conduction, ln(VI) vs. (e/kT) for ohmic conduction, and ln(G) vs. $T^{1/4}$ for variable range hopping (500 nm amorphous WO_3 based devices)

The third graph represents the fit of the data to the equation for variable range hopping conduction. The slope of the line represents a few of the possible barrier heights - making it impossible to single them out. However, it can be seen from the graph that the line includes almost all the data points. Therefore, it is the most convincing result of the three mechanisms considered. Thus, the electron flow in the 500 nm thick WO_3 films was consist with variable range hopping conduction.

Similar fitting calculations have also been carried out for the 250 nm thick amorphous WO_3 films. Both the data and the graphs support conduction via variable range hopping (see Figure 4.14 and Table 4.2).

Table 4.2 Fitted data for different electron transport mechanisms in amorphous WO_3

Thickness	electron transport mechanism	bias voltage (V)	activation energy (eV)	Intercept
500 nm	single electron hopping	5	0.72±0.02	46.27±0.43
		10	0.77±0.02	45.04±0.47
		15	0.80±0.02	44.18±0.51
		20	0.81±0.03	43.96±0.64

Table 4.2 (continue)

	ohmic conduction	5	0.68±0.02	2.43±0.43
		10	0.73±0.02	5.05±0.46
		15	0.76±0.02	6.72±0.49
		20	0.77±0.03	7.51±0.63
	variable range hopping	5	324.78±10.31	50.07±0.86
		10	348.43±4.57	55.04±0.96
		15	363.61±4.92	58.27±1.03
		20	367.43±8.08	59.09±1.69
250 nm	single electron hopping	5	0.93±0.09	42.22±2.14
		10	1.00±0.14	40.57±3.14
		15	0.99±0.14	40.92±3.34
		20	0.97±0.13	40.94±3.23
	ohmic conduction	5	0.89±0.09	6.46±2.13
		10	0.96±0.14	9.50±3.40
		15	0.94±0.14	9.96±3.33
		20	0.93±0.13	10.52±3.22
	variable range hopping	5	416.69±38.01	68.14±7.90
		10	449.79±61.80	74.97±12.84
		15	441.07±60.45	73.26±12.56
		20	432.26±62.33	71.866±10.54

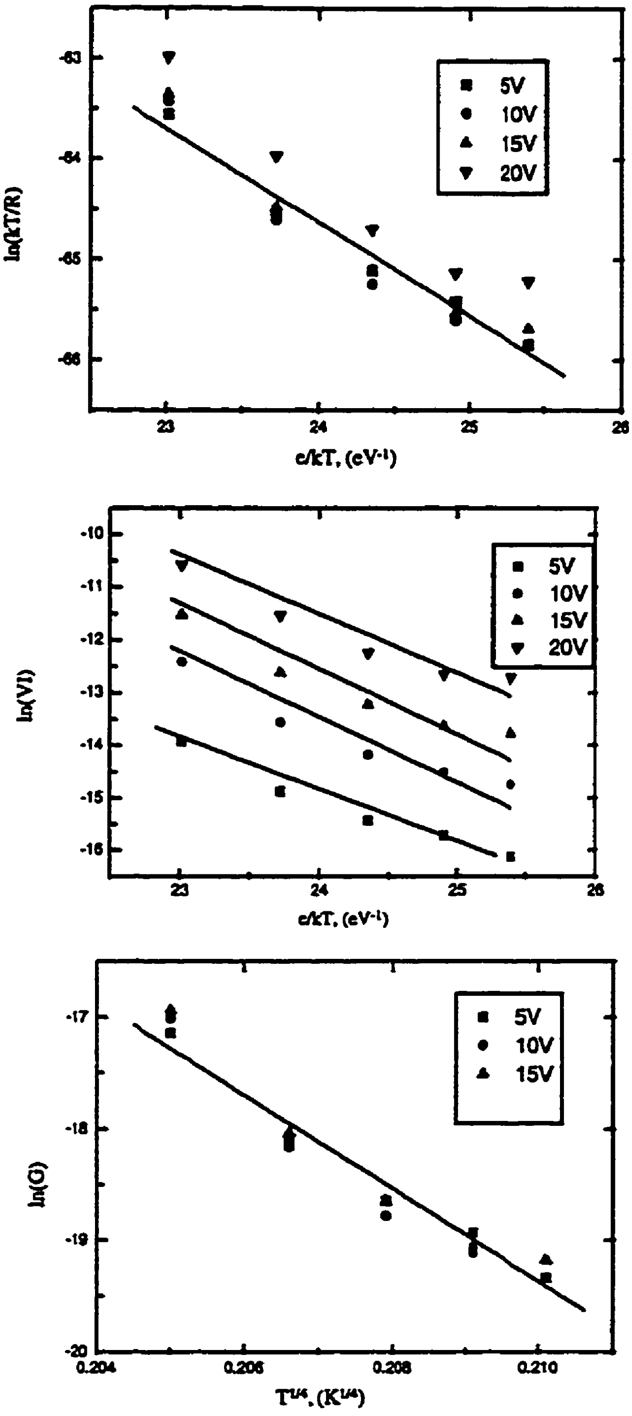

Figure 4.14 Plots of ln(kT/R) vs. (e/kT) for single electron hopping conduction, ln(VI) vs. (e/kT) for ohmic conduction, and ln(G) vs. $T^{1/4}$ for variable range hopping (250 nm amorphous WO_3 based devices)

4.5.3.4 Electron transport in polycrystalline materials

The electron transport mechanism for the polycrystalline materials was determined in a similar manner as outlined for the amorphous solids. However, the possible transport mechanisms for polycrystalline solids are different from those for amorphous materials. One of the most common mechanisms for electron transport in polycrystalline materials is thermionic emission [88]. Polycrystalline solids are formed from grains of various sizes, and the electrical conduction within a single grain is different from the conduction between grains [85-87, 91-93]. It has been proposed that the electrical conduction in materials containing different grains may be controlled by the conduction between the grains. Therefore, the resistance of the material is dominated by grain boundaries. The electrical data for the polycrystalline devices was fitted to thermionic emission conduction in order to determine the barrier height. If the electrons pass through the solid via thermionic emission conduction, then the current is described by the following equation:

$$I = cT^2 * EXP\left(\frac{-q\phi_B}{kT}\right)\left(\frac{qV}{kT}\right) \tag{4.5}$$

where I is the current, c is a constant, T is the absolute temperature, $q\phi_B$ is the barrier height and V is the applied bias [88]. The thermionic emission activation energies for these two polycrystalline WO_3 based devices are reported in Table 4.3. The fitted curves are plotted in Figures 4.15 and 4.16. The average calculated activation energy for the 500 nm thick polycrystalline WO_3 film is 0.14 eV whereas the activation energies for 250 nm thick films vary between 0.14 and 0.20 eV. Since the activation energy for conduction depends very much on the size of the grains and therefore the thickness of the film, the widely varying activation energies of the 250 nm thick indicate that the film is too thin for an accurate determination of the conductance.

Table 4.3 Fitted data for thermionic emission conduction in polycrystalline WO_3

Thickness (nm)	electron transport mechanism	bias voltage (V)	activation energy (eV)	Intercept
500 nm	thermionic emission	5	0.14±0.02	21.12±0.60
		10	0.14±0.02	19.29±0.64
		15	0.13±0.02	18.52±0.64
		20	0.13±0.02	17.88±0.73
250 nm	thermionic emission	5	0.14±0.01	21.05±0.39
		10	0.18±0.01	18.62±0.49
		15	0.20±0.02	17.22±0.59
		20	0.21±0.02	16.33±0.72

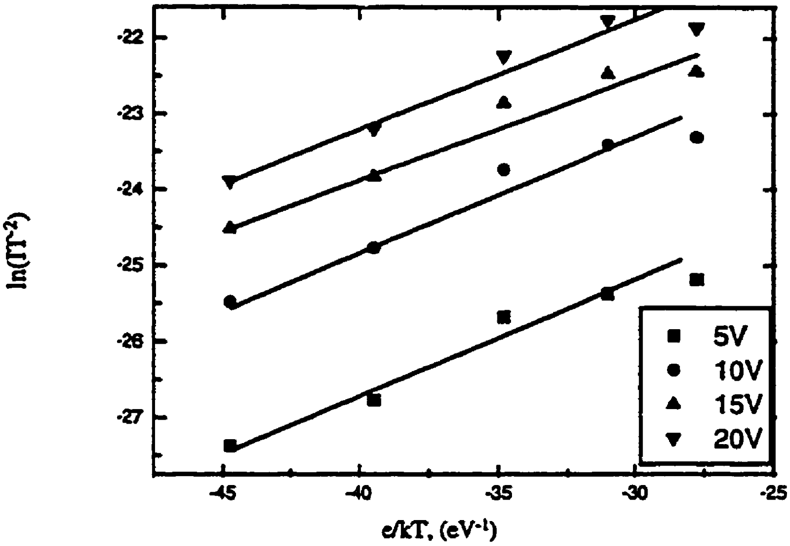

Figure 4.15 Plot of $\ln(I*T^{-2})$ vs. e/kT for thermionic emission conduction (500 nm polycrystalline WO_3 based devices)

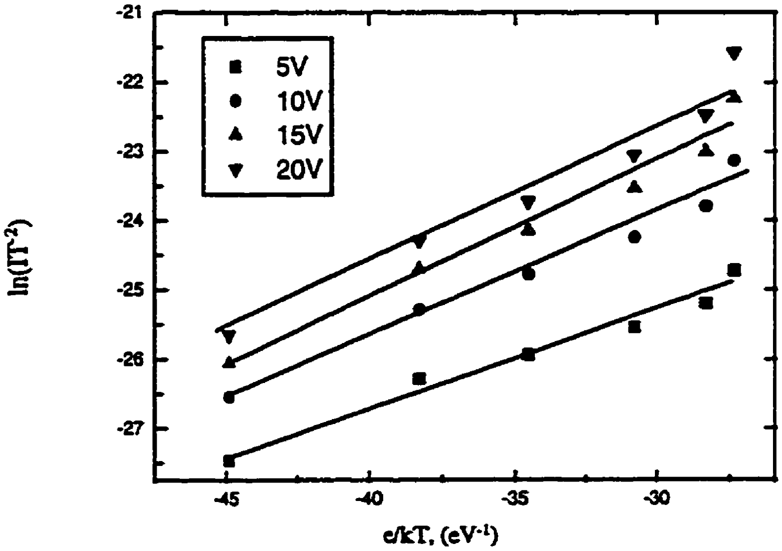

Figure 4.16 Plot of $\ln(I*T^{-2})$ vs. e/kT for thermionic emission conduction (250 nm polycrystalline WO_3 based devices)

4.5.4 Sensor response

4.5.4.1 Amorphous sensors

The sensors were exposed to various concentrations of NO_x gas at different temperatures. The temperature range used was 17°C to 300°C. Figures 4.17-21 show the changes in the electrical current through the 500 nm amorphous WO_3 film before and after it was exposed to various concentrations of NO_2 while maintaining the temperature at 242°C and the bias voltage at 1.53 V. The current of the sensor decreased from 15.5 to 13 nA after exposure to 0.1 ppm NO_2, but it dropped to a half upon introduction of 1.0 ppm NO_x. Thus, a larger current change was induced by increasing the amount of NO_x in the system. The sensor was also investigated at a temperature of 251°C (see Figures 4.22-24). The initial current (16 nA) increased to 22 nA, upon increasing the temperature to 251°C. The concentration of the NO_x used for exposure was 0.1, 0.5 and 1.0 ppm. The degree of the current change depended on the concentration of NO_x. Although the magnitude of the current deflection at 251°C and 242°C was similar, the recovery time was shorter when the sensor was operating at the higher temperature. The response of sensor to 1.0 ppm NO_x at different working temperatures is plotted in Figure 4.25. Upon exposure to 1.0 ppm NO_x at 251°C, it only took 5 seconds for the sensor to recover - half of the time required for the same sensor operated at 242°C. Thus, a higher operating temperature results in a higher current through the sensor and a faster recovery time. The data obtained for the sensor response is summarised in Table 4.4.

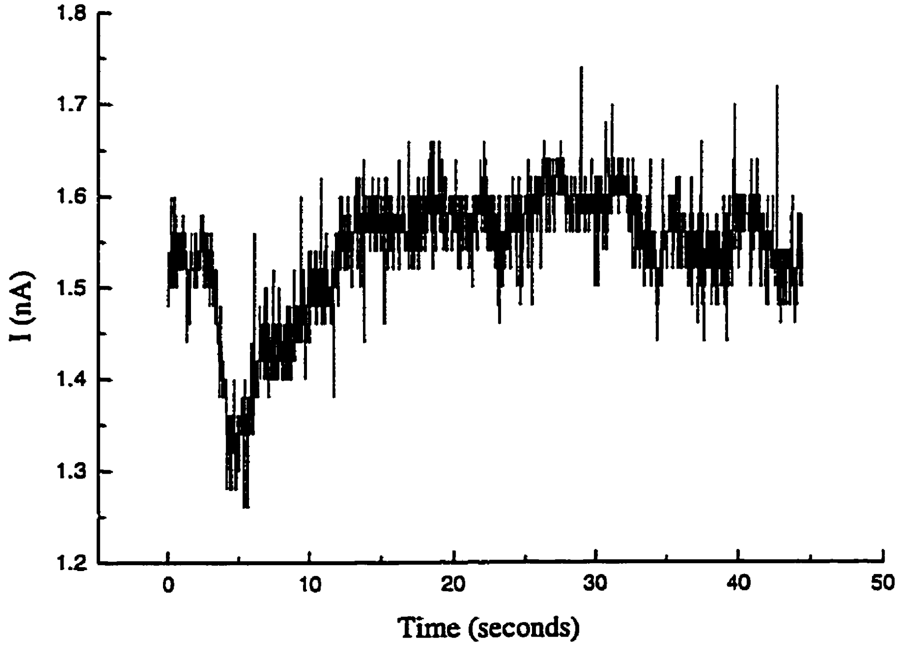

Figure 4.17 Plot of current vs. time for an amorphous WO_3 based sensor exposed to 0.1 ppm NO_x at 242°C (500 nm)

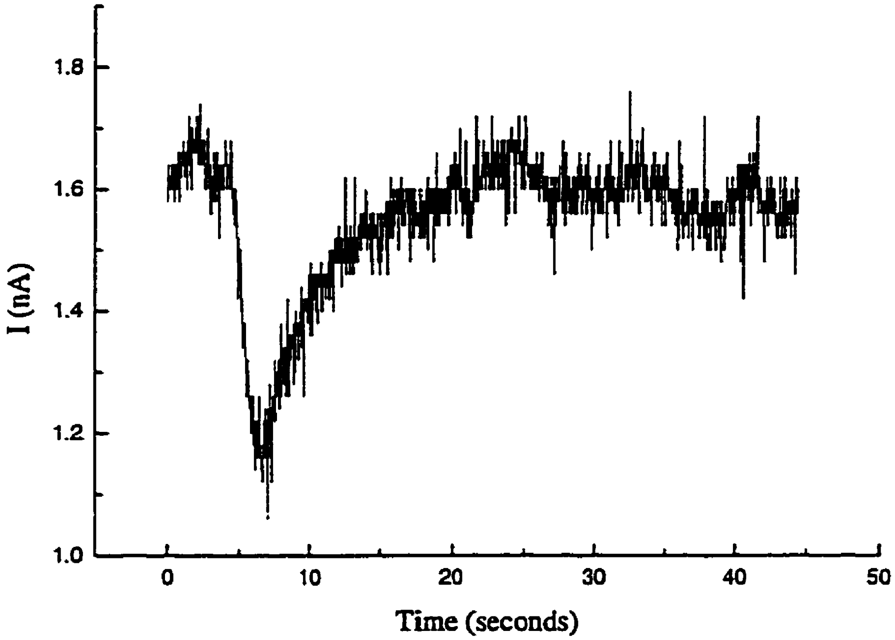

Figure 4.18 Plot of current vs. time for an amorphous WO_3 based sensor exposed to 0.2 ppm NO_x at 242°C (500 nm)

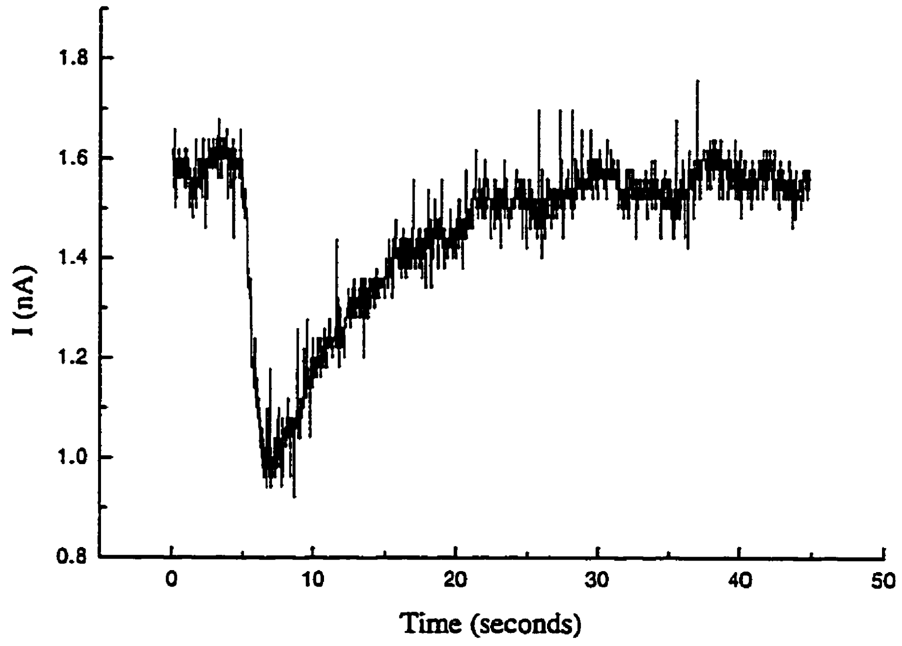

Figure 4.19 Plot of current vs. time for an amorphous WO_3 based sensor exposed to 0.5 ppm NO_x at 242°C (500 nm)

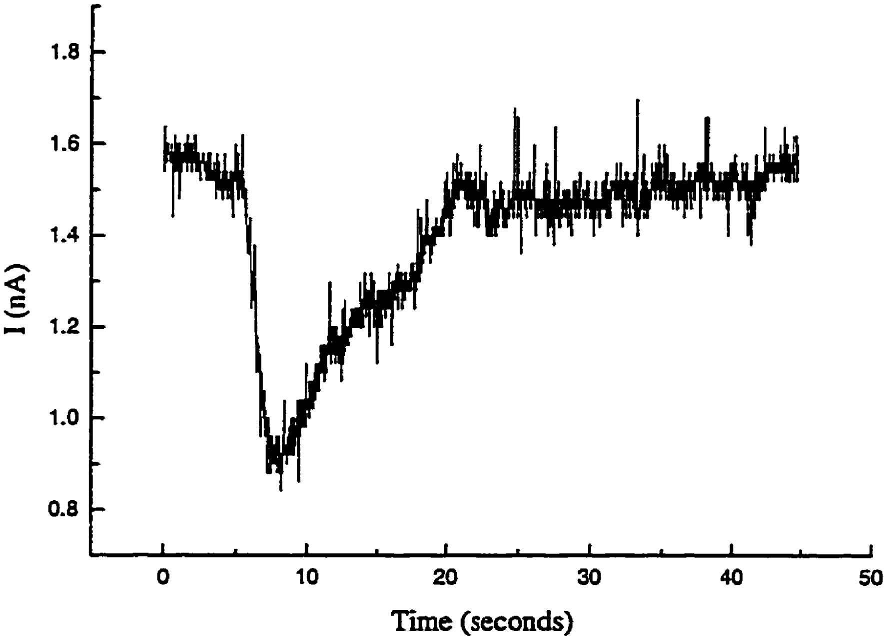

Figure 4.20 Plot of current vs. time for an amorphous WO_3 based sensor exposed to 1.0 ppm NO_x at 242°C (500 nm)

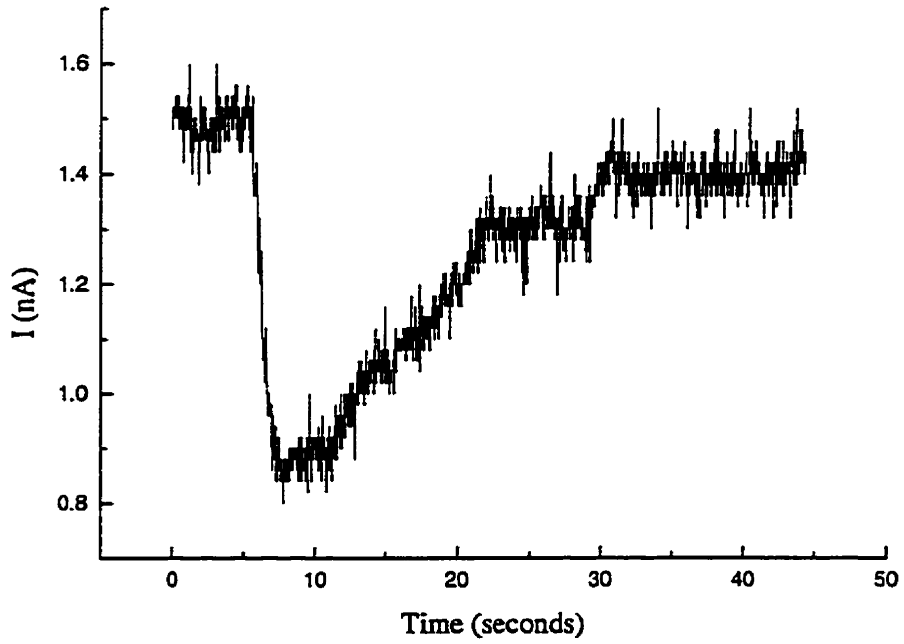

Figure 4.21 Plot of current vs. time for an amorphous WO_3 based sensor exposed to 3.0 ppm NO_x at 242°C (500 nm)

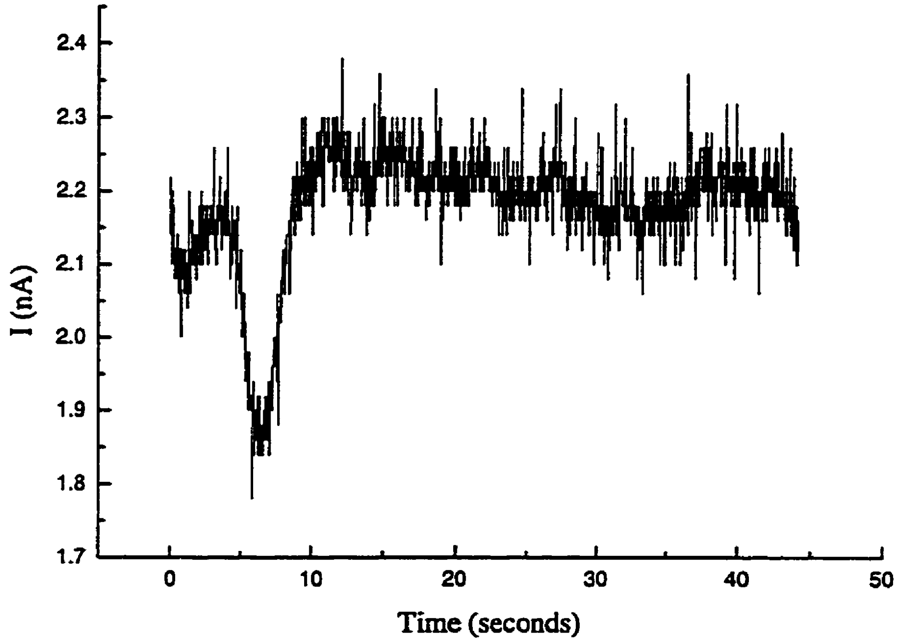

Figure 4.22 Plot of current vs. time for an amorphous WO_3 based sensor exposed to 0.1 ppm NO_x at 251°C (500 nm)

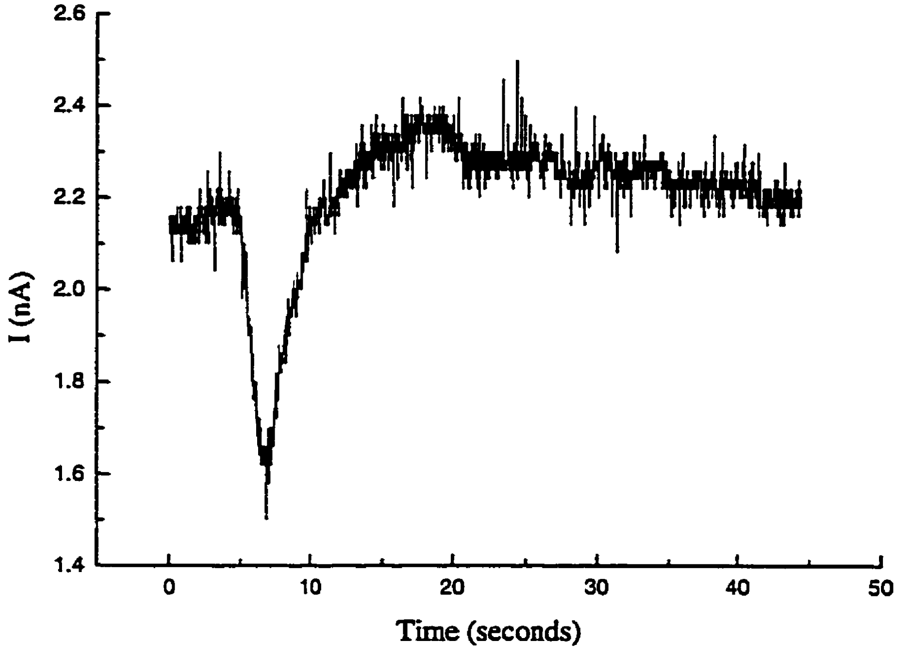

Figure 4.23 Plot of current vs. time for an amorphous WO_3 based sensor exposed to 0.5 ppm NO_x at 251°C (500 nm)

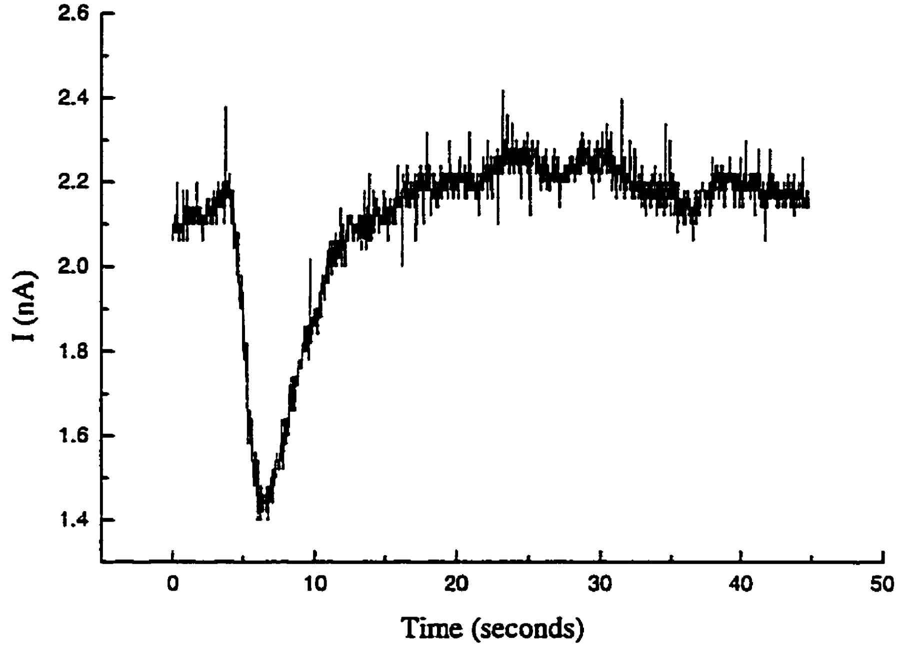

Figure 4.24 Plot of current vs. time for an amorphous WO_3 based sensor exposed to 1.0 ppm NO_x at 251°C (500 nm)

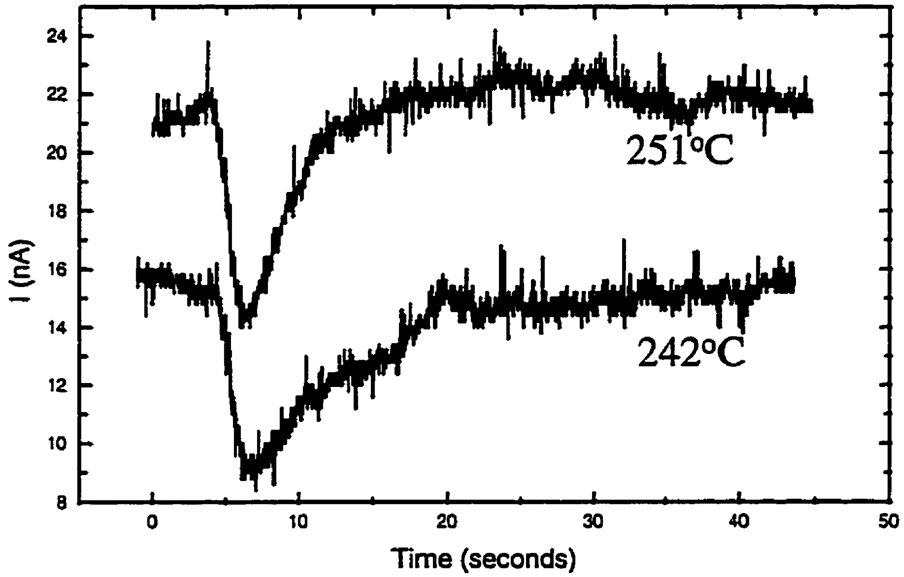

Figure 4.25 Plot of current vs. time for an amorphous WO_3 based sensor exposed to 1.0 ppm NO_x at 242 and 251°C (500 nm)

Table 4.4 **Table showing the sensor response of devices whose active elements are amorphous and polycrystalline WO_3**

Forms of WO_3	Thickness (nm)	Temp (°C)	ppm NO_x	Voltage (V)	Initial Current (nA)	Final Current (nA)	Recovery Time (sec)
amorphous	250	242	0.1	1.53	7	4	10
amorphous	500	242	0.1	1.53	15.5	13	10
			0.2		16	12	15
			0.5		16	10	25
			1.0		16	9	40
			3.0		16	8	40
		251	0.1	1.53	22	18.5	5
			0.5		22	16	5
			1.0		22	14	15
polycrystal-line	500	242	0.1	1.53	90	40	40
		242	0.5	1.53	90	20	40
		17	0.1	6.8	170	120	2.52×10^4

In general, the deflection of the current at fixed bias is dependent on the amount of NO_x introduced. An increase in the working temperature of the sensor results in a faster recovery time. The thickness of the sensor device does not change characteristics of the sensor significantly. Upon exposure to the same amount of NO_x the sensors took approximately the same time period to recover; however, for a given temperature, a thicker film resulted in a higher conductivity, as seen in Figure 4.10. A simplified molecular orbital diagram (Figure 4.26) is used to illustrate how NO_x affects the conductivity of the WO_3 sensor. The adsorption of an NO_x molecule on one of the surface sites of WO_3 leads to the combination of an excess electron in the band gap with the electron on the p-orbital from NO_x. As discussed in section 4.5.2 these excess electrons are a result of the oxygen vacancies in the materials. Since these excess electrons are responsible for conduction, the conductivity of the material will decrease if the amount of these majority carriers decreased (or the charges in the materials have been transferred to the gas molecules). In addition, since the adsorption and desorption rates are temperature dependent, a higher working temperature results in faster desorption. Presumably, the current would start to decrease as soon as the first NO_x molecule arrived and transferred charges from the metal oxide films to NO_x, and the current would continue to decrease as more NO_x adsorbed onto the surface. (According to the calculation in Section 4.7.3, some NO_x would arrive at sensor 0.16 second after injection.) However, at some point, the rate of adsorption and desorption of the NO_x on the surface will become equal. It would be difficult to determine the adsorption and desorption rate at this point, since it was impossible to determine the amount of NO_x adsorbed and the amount of NO_x desorbed from the surface. Moreover, since the total energy of NO, NO^{-1}, NO_2, and NO_2^{-1} are different, the corresponding adsorption heat and desorption heat are thus different. Therefore, the rate of the adsorption/desorption can only be determined when a systematic study is performed in a thermodynamically or kinetically controlled environment. There is another factor which determines the rate of the sensing response, i.e., the rate of the charge transfer between the adsorbate and the sensing materials. This would have to be carried out in more detailed spectroscopic study which will be described in Chapter 6. Hence, the rate limiting step in the sensing response was unable to conclude at this point.

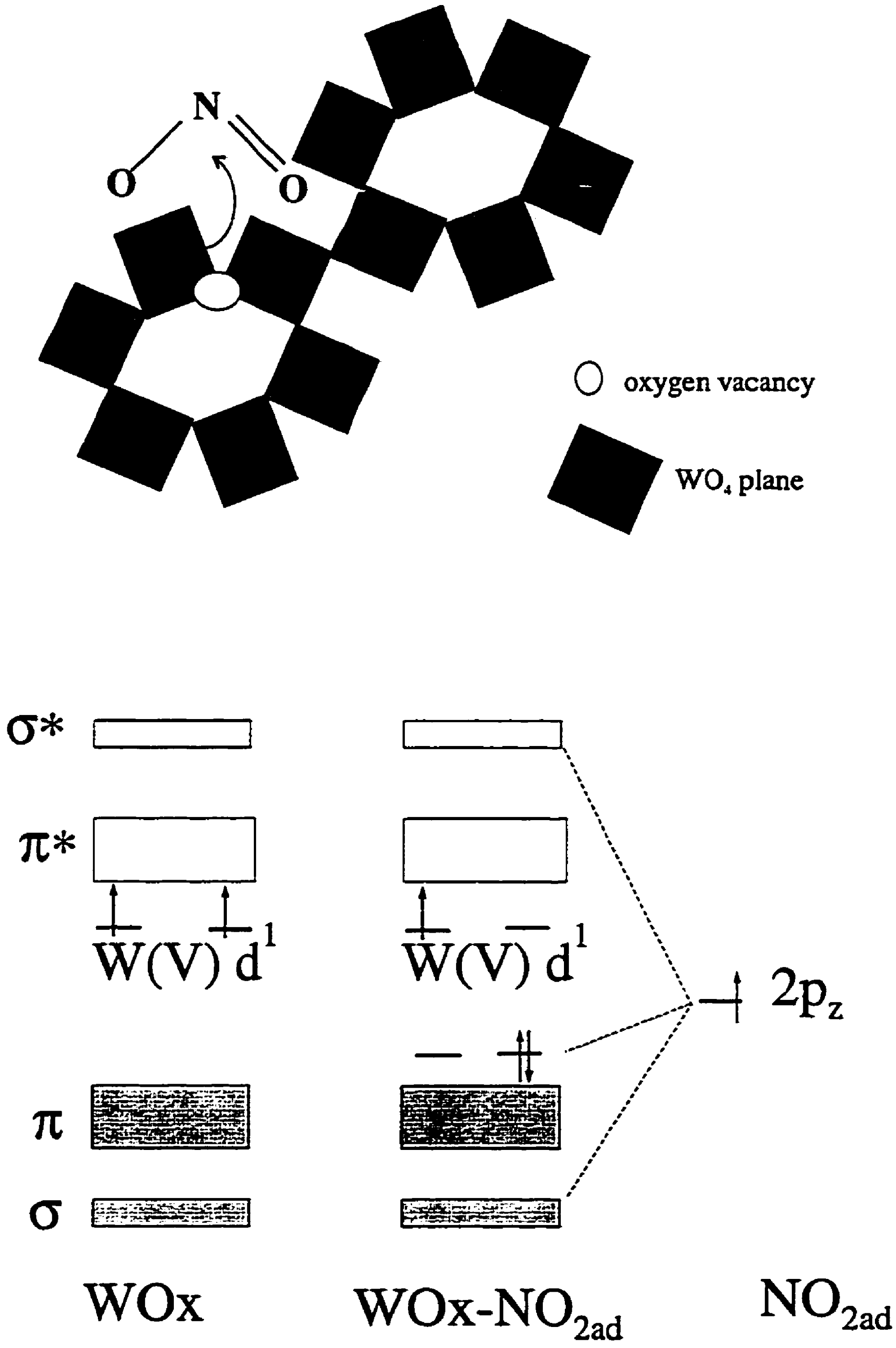

Figure 4.26 The adsorption of NO_2 on WO_3 surface

4.5.4.2 Polycrystalline based sensors

In order to compare the polycrystalline sensors to the amorphous ones, the polycrystalline based sensor was operated at 242°C. Figures 4.27-28 illustrates the sensor response of the 500 nm thick polycrystalline tungsten oxide based sensor to 0.1 and 0.5 ppm NO_x at 242°C. For the same bias voltage (1.53 V), the conductivity of the polycrystalline based device was six times that of the amorphous based devices; however, the recovery time was 30 seconds longer. In general, the behaviour of the polycrystalline based sensor was similar to that of the amorphous ones. A higher operating temperature resulted in a higher current and shorter recovery time. However, the polycrystalline based sensors could be operated at much lower temperatures than the amorphous based sensors (see Table 4.4). This is due to the higher conductivity of the sensing element that has been achieved by heat treatment. It was mentioned previously that because of instrumental limitations, the lowest temperature where sensor operation can be characterised is the temperature at which the current can be detected. The polycrystalline based sensor could be operated at 17°C; however, its recovery time at this temperature was as long as 7 hours. This observation indicates that the polycrystalline based sensors could not be used in an environment where prompt recovery time is required. All sensors have been monitored for a year, and their sensor response was reproducible for that time period.

4.5.4.3 Cross sensitivity

The cross sensitivity to NH_3, CO, C_2H_5OH and N_2 gases for the tungsten oxide based sensors has been tested.

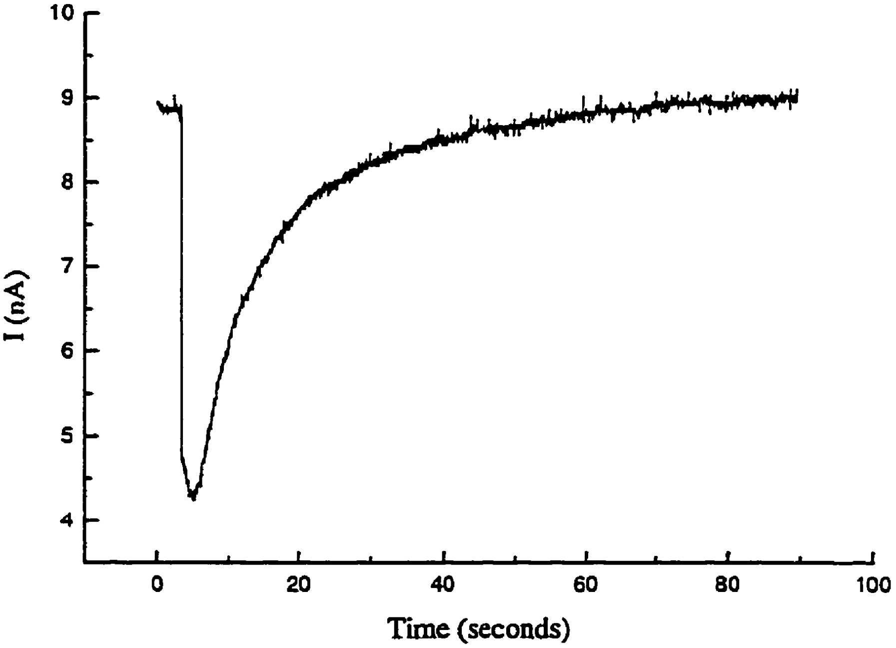

Figure 4.27 Plot of current vs. time for an polycrystalline WO_3 based sensor exposed to 0.1 ppm NO_x at 242°C (500 nm)

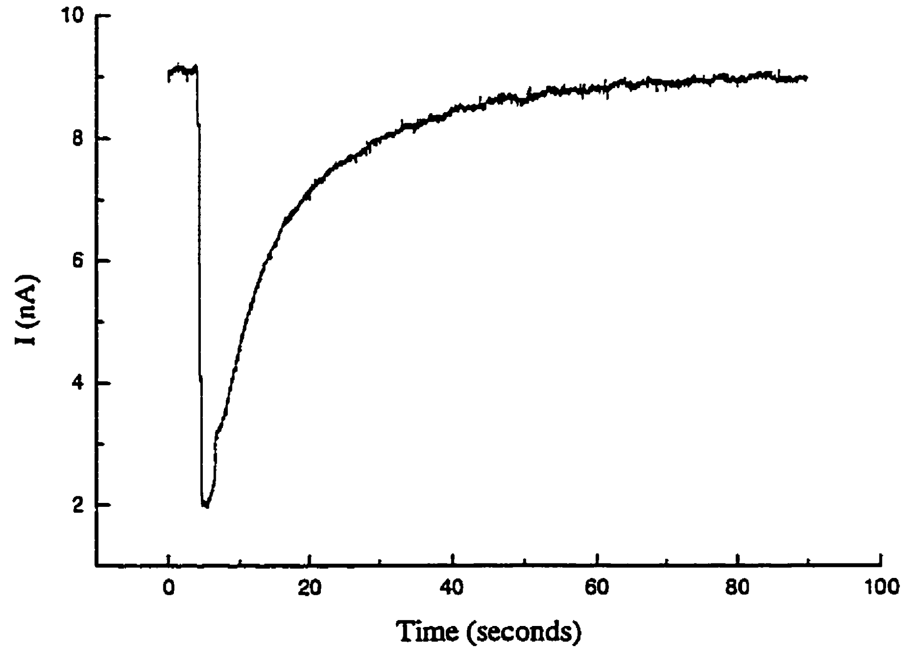

Figure 4.28 Plot of current vs. time for an polycrystalline WO_3 based sensor exposed to 0.5 ppm NO_x at 242°C (500 nm)

These gases were introduced into the gas chamber at 242°C for the devices based on amorphous materials and 17°C for the device based on polycrystalline materials. The temperatures chosen were the respective optimised working temperature for each sensor. It was found that none of the above gases cause any changes in the current through the device. Thus, there was no cross sensitivity between these gases and NO_x when the tungsten oxide based sensors were used. Although the exact concentrations of these gases were not calibrated, in excess of 1000 ppm of each was used. Even though the detailed cross sensitivity tests still need to be performed on the tungsten oxide based devices, this preliminary result is encouraging. The tungsten oxide based sensors can detect sub-ppm NO_x; however, they cannot detect the above gases at much higher concentrations. Hence, there was no cross sensitivity found at the optimised operating temperature of these sensors eliminating the possibility of a false alarm at this temperature when there are gases other than NOx present in the air.

4.6 Conclusion

A room temperature photochemical method for fabricating amorphous WO_3 based sensors has been presented. Amorphous WO_3 based devices of different thicknesses were made, and it was found that thicker sensors had lower resistance and hence a lower optimised working temperature. Since oxygen defects in the WO_3 material leave excess electrons in the metal centres, these excess electrons in the band gap induce the conduction in the semiconducting WO_3 material. The electron transport in amorphous materials was determined to be via variable range hopping. The activation energy for hopping between the initial and the final states can not be calculated because there is more than one final state. The electron flow in the polycrystalline material was via thermionic emission rather than via either the single or variable range hopping mechanism. The activation energies for polycrystalline WO_3 based devices of different thicknesses were calculated. The 500 nm thick films have higher conductivity and their activation energy could be determined more precisely than the 250 nm ones.

For all sensors tested, the sensitivity of the sensors was not influenced by thickness of the sensor. However, it was found that higher NO_x concentration and lower temperatures prolonged the recovery time. This is due to more NO_x on the surface requiring more time to desorb and a higher temperature causing a faster desorption rate. The sensor response of the polycrystalline WO_3 based sensors was approximately the same as the amorphous ones but with significantly lower working temperatures. The amorphous sensor has the advantage owing to its faster and easier production. All sensors were monitored for a year. The sensing response was reproducible over that time period. Even though the detailed cross sensitivity test on all gases to NO_x has not been carried out, preliminary results demonstrated that tungsten oxide based sensors were not influenced by gases other than NO_x at the optimised operating temperatures. The direct deposition method largely simplified the process of fabricating the sensors, and offered the possibility of producing the devices at ambient conditions. The high sensitivity and reproducibility found in both the amorphous and polycrystalline WO_3 based sensors have promised us better NO_x sensors for environmental monitoring.

4.7 Experimental

4.7.1 Instruments and chemicals

The Mask Aligner used for photolithography was the Quintel Q-4000 Wafer Alignment System. The wafer scriber is diamond saw style. The packages used for the devices were 24-pin ceramic device carriers. The photoresist used for photolithography was the positive resist Shipley SPR2. The developer was Shipley MF319. The developer used in the dark room for the development of the photoplate is the D19 from Kodak.

X-ray diffraction measurements were performed using a Philips MPD 1830 powder diffractometer with graphite monochromated Cu Kα radiation in the Bragg-Brentano parafocusing geometry. The FTIR spectra with 4 cm^{-1} resolution were obtained using a Bomem Michelson 120 FTIR spectrophotometer. Auger electron spectra were obtained at the Surface Physics Laboratory, Dept. of Physics, Simon Fraser University using a PHI double pass CMA with 0.85 eV resolution. Film thickness was determined using a Leitz Laborlux 12 ME S with an interference attachment.

4.7.2 Materials and substrates

Starting materials, $W(CO)_4(Et_2\text{-en})$, were synthesised following the literature method [79] and characterised by FTIR and elemental analysis. The substrate used was silicon oxide on which there were interdigitated aluminum electrodes. Those electrodes were deposited photolithographically with 1000 μm length, 15 μm width and 15 μm spacing.

4.7.3 Production and concentrations of NO_2

The NO_2 gas was produced by dissolving copper in nitric acid according to Equation 4.6 [83].

$$Cu_{(s)} + 4\,HNO_3\,(12M) \rightarrow Cu(NO_3)_{2(aq)} + 2NO_{2\,(g)} + 2H_2O_{\,(l)} \qquad (4.6)$$

The amount of NO_2 in the reactor was calibrated by producing the NO_2 with a known amount of copper in a known amount of a sealed flask. For example, complete reaction of 0.01 g Cu in 12 M HNO_3 would produce 0.014 g NO_2 and 0.0057 g H_2O. If the reaction proceeded in a 1 L sealed flask, then the concentration of NO_2 in the flask would be 14 ppm. If the sensor was going to be tested at 14 ppm NO_2, then 0.1 mL of the NO_2 gas was injected into the hose with dry N_2 flowing constantly at 37.1 mL/min flow rate. If the sensor was going to be tested at 0.1 ppm concentration of NO_2, then 0.007 mL of the 14 ppm NO_2 was mixed with dry N_2 to a total volume of 1 mL and then 0.1 mL of the 0.1 ppm NO_2 was injected into the hose. The travelling distance between the sensor and the injection point on the hose is 1.2 cm. The diameter of the hose is 0.5 cm, the amount of dry N_2 in the 1.2 cm hose is about 0.23 mL. In an ideal case, 0.1 mL of NO_2 would arrive at the sensor after 0.16 seconds of the injection time. The 0.1 ppm NO_2 injected into the hose would result in a lower concentration than 0.1 ppm. The concentration of NO_2 in the N_2 stream would increase gradually during the injection. The peak concentration would be 0.1 ppm, in an ideal case. The largest current change of the sensor should reflect the peak concentration of the NO_2. Hence, the reported sensor response provides a lower estimate of the sensor response to 0.1 ppm NO_2.

4.7.4 Purity of NO_2

It has been reported in Section 4.7.3 that the production of NO_2 was accompanied by the formation of H_2O. It was assumed that since the limiting reagent is the amount of Cu dissolved in HNO_3, the amount of NO_2 produced was calculated according to the amount of Cu used. Another factor which may contribute to the error on the amount of the NO_2 produced was the formation of H_2O. Since NO_2 would dissolved in H_2O to form HNO_3 and HNO_2. However, this error was assumed to be small since the amount of H_2O produced was very small, e.g., 0.0057 g of water would be produced while 14 ppm of NO_2 was produced in a 1 L flask. The possible of water effect on the sensor resulting from the non-dried NO_2 was eliminated experimentally. The sensor was exposed to a 1 mL sample of non-dried air to see whether or not the conductivity of the sensor would change. There was no significant change in the current of the sensor with the biases and temperatures used in this study. (Generally, the conductivity of thin films would increase with higher moisture content in the material and in air.) Even though a detailed study of the moisture effect on the sensor is still required, preliminary result indicated that the non-dried air did not change the conductivity of the sensor significantly under the conditions used in this work.

Another situation which may contribute some degree of error in the concentration of NO_2 was that nitrogen dioxides and dinitrogen tetroxides were assumed to exist in a strongly temperature-dependent equilibrium, and the equilibrium constant, Keq, at 25°C is 0.0046 [94].

$$N_2O_{4(g)} \rightarrow 2\ NO_{2(g)} \qquad (4.7)$$

It was then important to calculate the amount of N_2O_4 would be produced, if 14 ppm of NO_2 was produced in a 1 L sealed flask. After performing the calculation, the amount of N_2O_4 would be produced in this case was 0.0426 ppm. These produced N_2O_4 molecules would introduce 0.3% error into the reported concentrations of NO_2. According to Equations 1.8-1.10, NO_2 would be converted to NO with the presence of light, and NO would be converted to NO_2 with the presence of O_3. The ratio of NO to NO_2 varied with the concentration of O_3 and the light intensity. For example, there are more NO than NO_2 in the day time and more NO_2 than NO at dark, or at night [1]. Since not only both nitrogen oxides are air pollutant, but also their concentrations vary with the atmosphere, it is therefore important to fabricate a NO_x sensor which can be used to monitor both NO and NO_2 at various of conditions.

4.7.5 Procedures on the NO_x sensor testing

A known amount of NO_x was injected into the dry N_2 hose under conditions of constant voltages and flow rates. The conductivity change with respect to the various concentrations of NO_x was monitored at different temperatures.

4.7.6 Darkroom preparation

An acetate sheet with defined features was placed in direct contact with a photoplate. The photoplate was then exposed through the acetate sheet for 30 seconds. After turning off the light, the photoplate was transferred to the developer for one and a half minutes. The photoplate was rinsed in water for five minutes and then transferred to the fixer for 5 minutes. After its removal from the fixer, the photoplate was rinsed in running water for 20 minutes. The plate was slowly dried with nitrogen for 2 minutes. The clarity of pattern on the plate was examined under the microscope.

4.7.7 RCA cleaning

Wafers were cleaned by using standard RCA SC1 and SC2 cleaning procedures. In the RCA SC1 procedure, 1000 mL of de-ionised (DI) water, 200 mL 30% NH_4OH and 200 mL 50% H_2O_2 were placed in a 2000 mL beaker and heated to approximately 70°C. The temperature of the solution was adjusted to 80 ± 5°C. The volume of the solution was sufficient to clean six wafers at a time. Wafers were placed in the beaker for 10 minutes, and then rinsed with running de-ionised (DI) water for at least three minutes. Wafers were then ready for the HF acid cleaning. This step was to strip the native oxide. A solution containing 1600 mL DI water and 16 mL HF was made in a 2 L plastic beaker. The wafers were placed into the solution for 30 seconds at room temperature, and then rinsed with running DI water for at least 3 minutes. The next step was the RCA SC-2 Clean. The purpose of this step was to remove any metals from the surface. In this procedure, 1050 mL DI water was placed in a 2 L glass beaker. 175 mL HCl and 175 mL H_2O_2 were added to the beaker after the temperature of the de-ionised water has been heated to approximately 80°C. Once the temperature of the solution was at 80±5°C, wafers were immersed in it for 10 minutes. The wafers were then rinsed with running DI water for at least 5 minutes. The rinsing procedure was repeated twice with clean water. The wafers were then transferred to a spinner for drying. They were spun at 4000 RPM for approximately 30 seconds. Any water left on the back side of the wafer was removed with dry N_2.

4.7.8 Photolithography

Cleaned wafers which has been sputtered with aluminum layers on top were baked at 100°C for 25 minutes before depositing photoresist on them. The wafers were allowed to cool to room temperature before spinning the photoresist. Three drops of the photoresist were carefully placed on top of the wafer, and the spinner was turned on. In order to form a uniform film, the wafers were spun at 4000 RPM for 30 seconds. The wafers were examined for defects under a microscope equipped with a yellow filter. The purpose of using the yellow filter is because it cuts off the wavelength of light which the photoresist absorbs. The wafers were then placed in the oven at 100°C for 25 minutes. The mask for this wafer was loaded in the mask aligner correctly with the x-y stage. Once loaded, the wafers should be in contact with the mask and exposed to light for 15 seconds. The wafers were then rinsed with MF319 developer at room temperature for 60 seconds causing the features on the wafers to appear. The wafers were then rinsed with running DI water for at least 3 minutes, and spun dry at 4000 RPM. At this point, the features on the wafers were examined under the microscope. If the features were fine and clear, the wafer was ready for the hard bake (20 minutes at 120°C in the oven). Otherwise, the photoresist was stripped off (20 minutes in acetone at room temperature), the photolithography process could thus be started afresh.

The aluminum etchant was used at 50°C to obtain an etch rate of 100 Å/sec. Wafers were soaked in the aluminum etchant for 50 seconds if the aluminum layer was 500 nm thick, and then rinsed in running DI water for 5 minutes. The features on the wafer were examined under the microscope for possible underetching or overetching. The wafers were soaked in room temperature acetone for 5 minutes, and then for a further 2 minutes in fresh acetone in order to strip the photoresist. Again, the wafers were rinsed in running DI water for at least three minutes. After this procedure, the wafers were ready for cutting.

4.7.9 Wafer Scribing, Cutting and Packaging

The wafer was scribed by a diamond tip and then cleaved to separate the devices. Individual devices were then gold bonded to a 24-pin device carrier. Ceramic device carriers were used for packaging.

4.7.10 Hot-probe method

In order to determine whether the semiconductor is n-type material with electrons as the majority carriers or p-type with holes as the majority carriers, hot probe method was used. First of all, heat was applied on a certain metal tip which touched the surface gently. One side of the voltage-meter was then connected to the metal tip, and the other side was connected to the surface with a distance away from the hot tip. Since the hot point made carriers expand away from the contact point, the charge of the dominant carrier species (electrons or holes) determined the voltages measured. If the measured material was n-type, electrons would be excited by the heat and moved away from the hot tip. Therefore, a positive voltage would be read in the meter and vise versa.

CHAPTER 5

Novel amorphous $Mo_{0.05}WO$ and $Mo_{0.09}W_{0.73}O$ based sensors made photochemically at room temperature for sub-ppm NO_x detection

5.1 Introduction

In the previous chapter, sensors based on amorphous films of tungsten oxide were fabricated and they responded to sub-ppm NO_x. However, the resistivity of the amorphous tungsten oxide films was low and therefore a high operating temperature (~ 200°C) was required to operate these sensors. Thus the objective of this chapter is to fabricate sensors with lower resistivity in order to achieve lower operating temperatures. Doping is one common method used in material fabrication to increase the conductivity of a material. Tungsten oxide will therefore be doped with other elements in order to decrease its resistivity. Molybdenum oxide was chosen to act as dopant in the tungsten oxide films, since there have been a few molybdenum complexes used as catalysts for converting NO_2 to N_2 and O_2 [96]. In order to make mixed metal oxides by the same photochemical method, $Mo(CO)_4(Et_2\text{-en})$ was used to mix with $W(CO)_4(Et_2\text{-en})$ before deposition. In this chapter, the material, structural and electrical properties of the mixed metal oxide thin films will be presented first. Their electron transport mechanism will be determined and reported. Finally, the sensitivity of these devices is described and discussed. This is the first time that amorphous $Mo_{0.05}WO$ and $Mo_{0.09}W_{0.73}O$ thin film sensors have been made, and they will be proven to respond to sub-ppm NO_x at temperatures ~100°C.

5.2 Results and discussion

5.2.1 Materials characterisation

Approximately 0.002 g of a one to twenty stoichiometric mixture of $Mo(CO)_4(Et_2\text{-en})$ and $W(CO)_4(Et_2\text{-en})$ was dissolved in CH_2Cl_2 to make a stock solution. A portion of the stock solution was spun cast onto the interdigitated electrode device to make an amorphous film of the starting material. The design of the device as well as the fabrication sequence has been described previously. Under identical conditions, a single drop of the stock solution was placed on a silicon chip with no electrodes for reference. This chip was used to characterise the solid state material via FTIR spectroscopy. The FTIR spectrum was monitored on a substrate without aluminium electrodes because the highly conducting electrodes scatter photons decreasing the signal of the spectra to noise ratio. In order to construct a thicker film, the above process was repeated several times. For example, ten consecutive sequences of a spin-coat followed by photolysis were used to generate 500 nm thick films. The FTIR spectra in Figure 5.1 show the changes upon photolysis of a 1:20 mixture of $Mo(CO)_4(Et_2\text{-en})$ and $W(CO)_4(Et_2\text{-en})$ as surface film. The peaks centred at 1800 and 1850 cm^{-1} are due to the carbonyl stretches of the starting materials. The study of the photochemistry of each starting material has been described in Chapter 3.

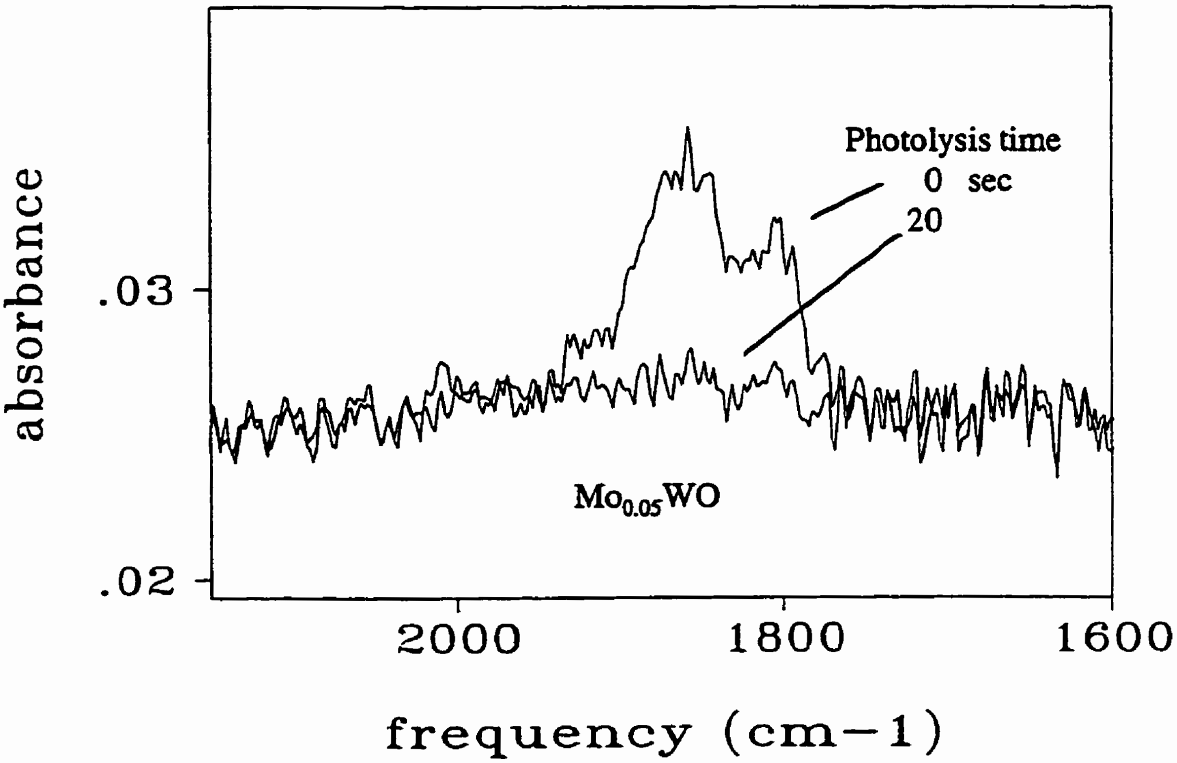

Figure 5.1 FTIR spectra associated with the photolysis of 1:20 $Mo(CO)_4(Et_2\text{-}en)$: $W(CO)_4(Et_2\text{-}en)$ mixture as a surface film on silicon

All starting materials reacted photochemically to form metal oxide films. The dosage required in order to complete this photochemical reaction was found to be 140 mJ/cm^2 per layer. The resultant film was analysed by AES at both the surface and two different spots inside the film in order to characterise the composition throughout the film. Auger analysis of the final film indicated that the composition of the product was $Mo_{0.05}WO$ (see Table 5.1). For comparison, similar preparation and deposition methods were carried out on the production of a more heavily doped tungsten oxide film. The photochemistry of mixture is similar to that of the $Mo_{0.05}WO$ film while its composition was found to be $Mo_{0.09}W_{0.73}O$. The dosage required to convert the precursor mixture to $Mo_{0.09}W_{0.73}O$ photochemically was found to be 420 mJ/cm^2 per layer. Both metal oxide films were 500 nm thick, and were found to be n-type semiconductors when tested by the hot probe method [95]. Although carbon was found at the surfaces of both films, the 10 second sputtering, which probe deeper into the layers, shows that there were no contaminants found inside the films (see Table 5.1). This indicates that pure mixed metal oxide films had been made, and their compositions inside the films were uniform.

Table 5.1 Auger analysis of MoWxOy thin amorphous films

sputter time (sec.)	% Mo	%W	% O	%C	Composition (Calculation)
0	4.3±2.3	35±4	54±5	7±5	$Mo_{0.08}W_{0.65}O$
10	5.4±2.2	40±5	55±5	-	$Mo_{0.098}W_{0.73}O$
10	5±2.2	40±5	55±5	-	$Mo_{0.09}W_{0.73}O$
0	1.7±1	39±2	43±3	17±10	$Mo_{0.04}W_{0.9}O$
10	2.5±1.2	49±2	49±2	-	$Mo_{0.05}WO$
10	2.4±1.5	49±2	48±2	-	$Mo_{0.05}WO$

5.2.2 Structural characterisation

The film of $Mo_{0.05}WO$ was transferred to the X-ray diffraction spectrometer. Figure 5.2 shows the XRD pattern of the as-deposited film. There is no observable reflection for the photolysed film, implying that it is amorphous in nature. The amorphous $Mo_{0.05}WO$ film was then annealed at 500°C in the air for two hours. The resultant film has three peaks in the XRD spectrum (see Figure 5.2). The peaks were assigned according to the ones found in the molybdenum tungsten oxides as (1 1 1) plane at $2\theta = 33.31°$, (1 0 3) plane at $2\theta = 37.75°$ and (-2 1 3) plane at $2\theta = 44.51°$ [91]. A well crystallised film of primarily a (111) orientation was suggested by the observation of this strongest peak centred at 33.31°. The crystal structures of molybdenum doped tungsten oxides are very similar to that of WO_3 when the molybdenum content in the mixture oxides is less than 25 mole % [91]. The lattice structure of polycrystalline films derived from $Mo_{0.05}W_{0.95}O_3$ assumed to be similar to that of WO_3 with a ReO_3 type of structure. Figure 5.3 illustrates the lattice structure, with an oxygen at each corner of the cube, and a tungsten or molybdenum at the centre. Since the tungsten to molybdenum ratio is 1:20, one out of every twenty-one tungsten atoms is replaced by a molybdenum atom while each oxygen atom is shared by two neighbouring tungsten atoms. Since both tungsten and molybdenum have an oxidation state of six, they both donate all d-electrons to the oxygens surrounding them. Band structures for $Mo_{0.05}W_{0.95}O_3$ are illustrated in Figure 5.3. The d-orbitals from the molybdenum and tungsten atoms combine with the p-orbitals from oxygen to form four molecular orbitals - σ, π, σ^*, and π^*.

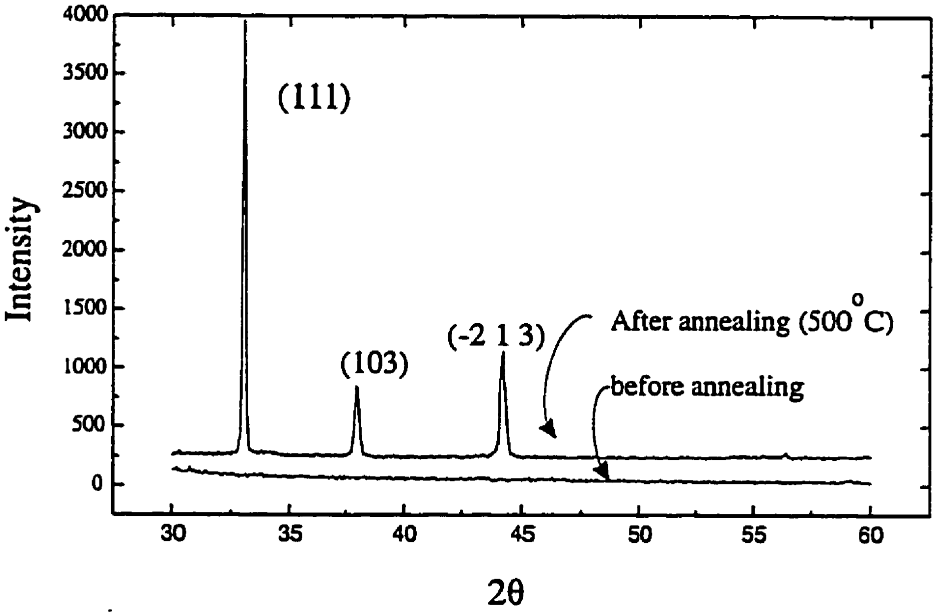

Figure 5.2 XRD patterns of the as-deopsited and annealed $Mo_{0.05}WO$at 500°C

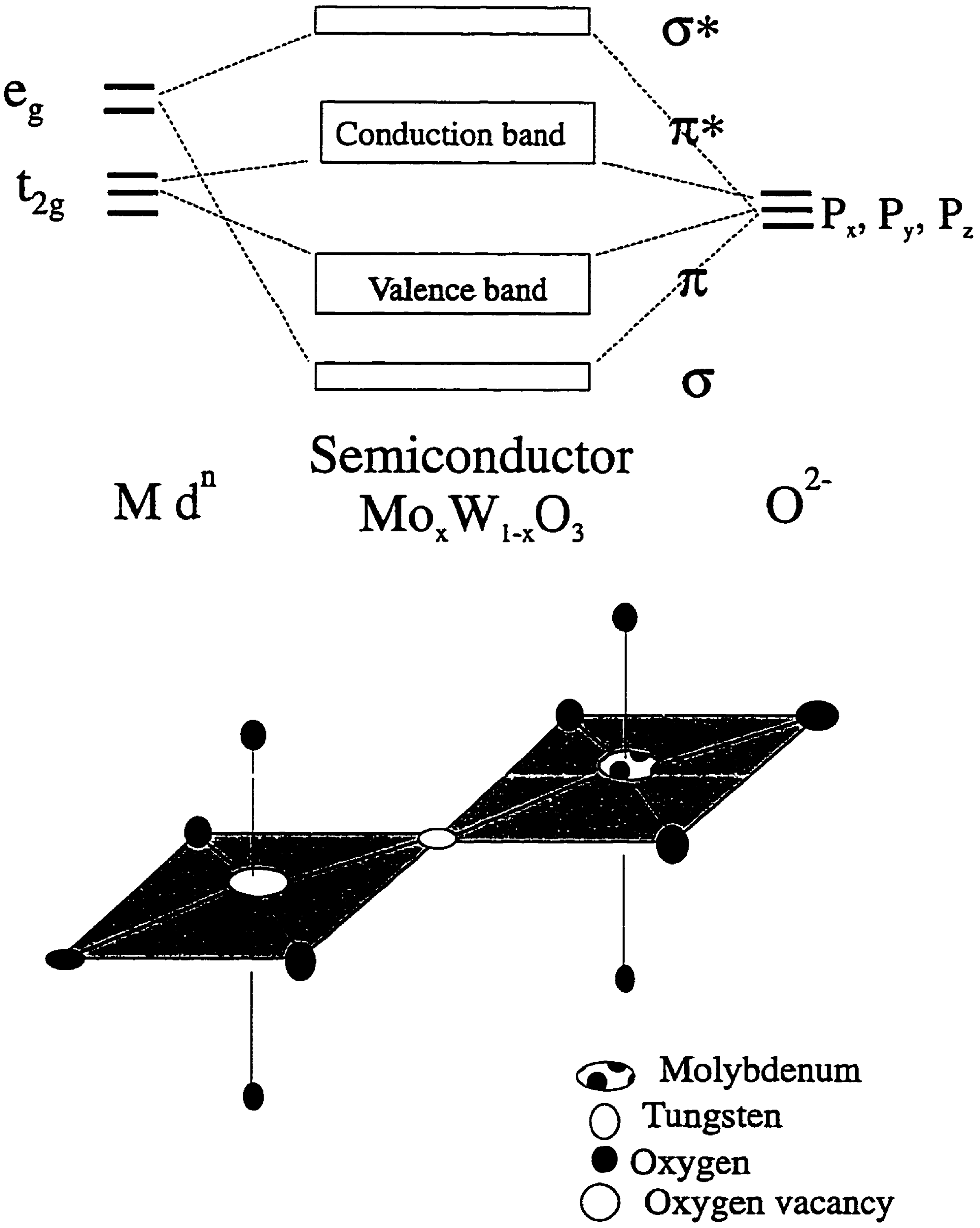

Figure 5.3 The lattice and band structure of $Mo_xW_{1-x}O_3$

Since the σ and π orbitals are full and the σ^* and π^* orbitals are empty, the band gap separates π and π^* orbitals. The most stable metal oxide for molybdenum is MoO_3, and for tungsten is WO_3 [97]. However, from the analysis of the Auger spectra it was found that the composition of the amorphous mixed metal oxide is $Mo_{0.05}WO$. This result indicated that there was an even greater oxygen deficiency in the mixed metal oxides than in the amorphous WO_3. As previously discussed in Chapter 4, an increase in the number of oxygen defect sites results more electrons in the band gap. Because these electrons are the majority carriers responsible for conduction, the conductivity of the mixed metal oxides will be enhanced. This hypothesis will be supported by an examination of the electronic characteristics of the mixed metal oxides in the next section.

5.2.3 Electrical characteristics

5.2.3.1 Current-Voltage behaviour for devices based on amorphous $Mo_{0.05}WO$ and $Mo_{0.09}W_{0.73}O$

The I-V characteristics of the amorphous $Mo_{0.05}WO$ based devices have been measured at different temperatures. The current through the amorphous $Mo_{0.05}WO$ based devices was measured for bias voltages between 5 and 20 V, and has been periodically monitored over a year (see Figure 5.4). The current-voltage relationship stayed roughly the same throughout that time period, and can be approximated by Ohm's law - current increases linearly with the bias voltage.

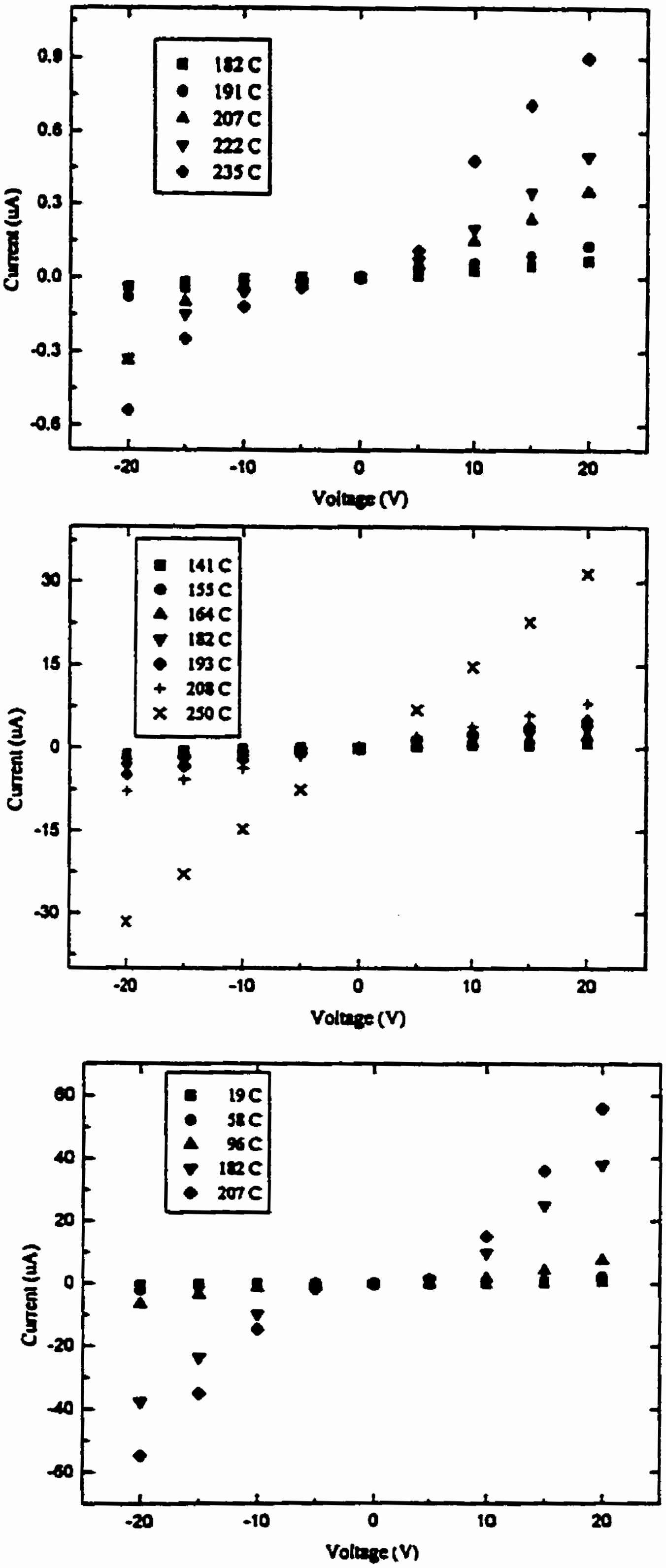

Figure 5.4 IV characteristics of devices based on amorphous $Mo_{0.05}WO$, amorphous $Mo_{0.09}W_{0.73}O$ and polycrystalline $Mo_{0.05}W_{0.95}O_3$ of 500 nm thickness

The current-voltage behaviour was monitored for temperatures between 182°C and 235°C for each bias voltage. It was found that the conductivity of the amorphous films was very sensitive to temperatures because the resistance of these films decreased with increasing temperatures. The I-V characteristics of the $Mo_{0.09}W_{0.73}O$ based devices were measured in a similar manner to that of the $Mo_{0.05}WO$ devices (see Figure 5.4). Their current-voltage relationship was also found to agree with Ohm's law. It can be seen from the I-V curves for both metal oxide devices that the $Mo_{0.09}W_{0.73}O$ device has higher conductivity than the $Mo_{0.05}WO$ device at a given temperature.

5.2.3.2 Current-Voltage behaviour for devices based on polycrystalline $Mo_{0.05}W_{0.95}O_3$

The current of the polycrystalline $Mo_{0.05}W_{0.95}O_3$ based devices was measured using a similar protocol to the one used for the amorphous devices. The I-V characteristics for the annealed $Mo_{0.05}W_{0.95}O_3$ are also plotted in Figure 5.4. The current-voltage relationship did not obey Ohm's law; instead, the current of the polycrystalline devices increased exponentially with increasing voltages. It was found that the conductivity of the $Mo_{0.05}W_{0.95}O_3$ based devices increased by a factor of eight after annealing. The current-voltage behaviour has been monitored for a year, and it stayed roughly the same.

5.2.3.3 Electron transport in amorphous $Mo_{0.05}WO$ and $Mo_{0.09}W_{0.73}O$

In order to determine the electron transport mechanism in the amorphous materials, there are three types of conduction mechanisms which must be considered. As discussed in Section 4.5.4, the three possible mechanisms are variable-range hopping conduction, single electron hopping conduction, and ohmic conduction. The conductivity data was fitted with three equations, each representing one of the three types of electron conduction. The equation used for variable range hopping is $\sigma = \sigma_o$ EXP($- \alpha T^{-1/4}$); where σ is the conductivity of the device, σ_o and α are constants, and T is the temperature. The equation used for single electron hopping conduction is J = Jo EXP(-Ea/kT); where J is the current density of the device, Ea is the activation energy, and T is the temperature. The equation used for ohmic conduction is J = F EXP(-Ea/kT); where J is the current density, F is the electric field, and Ea is the activation energy. The fitted curves for the amorphous $Mo_{0.05}WO$ based devices are plotted in Figure 5.5, and the fitted data is summarised in Table 5.2. In order to determine which is the best fit, both the fitted curves and data must be further examined. The fitted plots for the variable range hopping and single electron hopping conduction are respectively illustrated in the first and the third graphs of Figure 5.5. Ideally, the fitted straight lines should include all the data points; however, only the line in the single electron hopping conduction plot satisfies this theory. In addition, the four fitted lines in the ohmic conduction plot do not give similar slopes and intercepts, which should be the case if the electron flow in the material was via ohmic conduction.

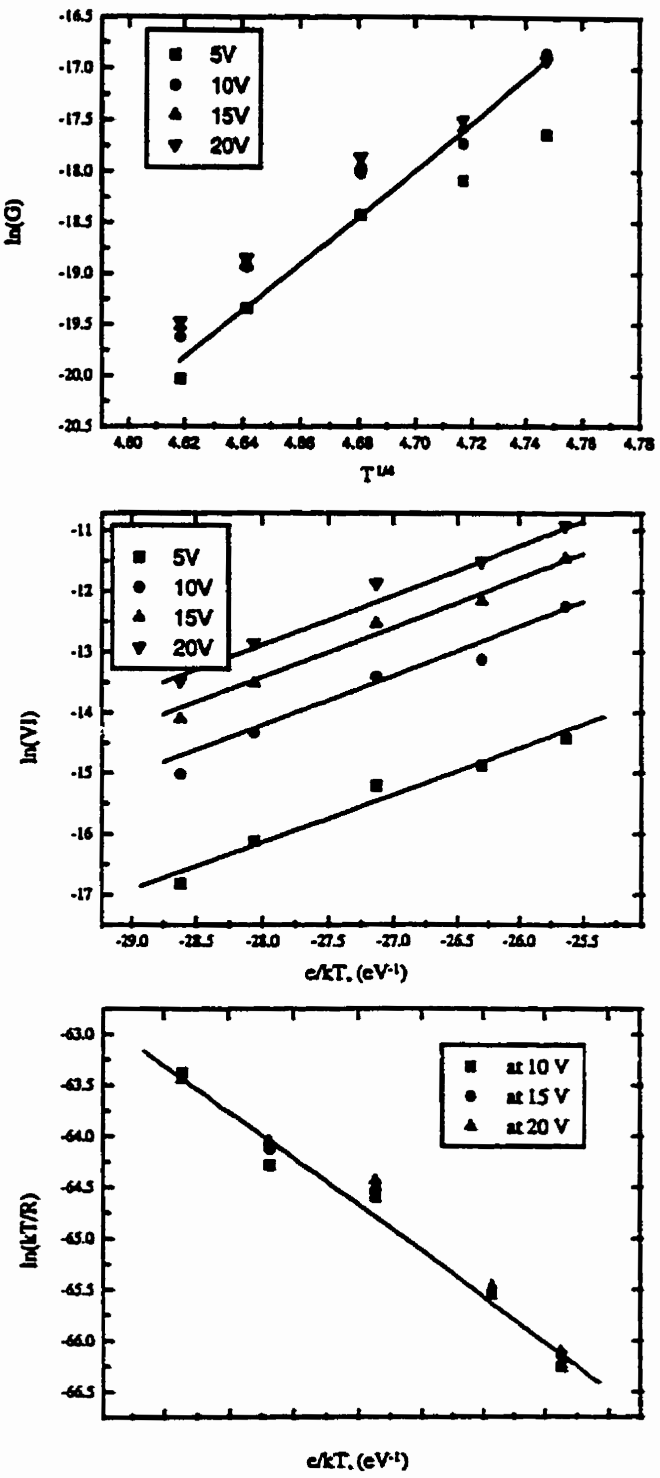

Figure 5.5 Plots of ln(G) vs. $T^{1/4}$ for variable range hopping, ln(VI) vs. (e/kT) for ohmic conduction, and ln(kT/R) vs. (e/kT) for single electron hopping conduction (500 nm amorphous $Mo_{0.05}WO$ based device)

Table 5.2 Activation energies for conduction in Mo$_{0.05}$WO and Mo$_{0.09}$W$_{0.73}$O based devices

Active material	electron transport mechanism	bias voltage (V)	activation energy (eV)	Intercept
amorphous Mo$_{0.05}$WO 500 nm	single electron hopping	5	0.82±0.07	43.12±1.71
		10	0.90±0.08	40.26±2.19
		15	0.90±0.06	40.40±1.63
		20	0.87±0.07	41.08±1.87
	ohmic conduction	5	0.78±0.08	5.68±2.25
		10	0.87±0.08	9.92±2.20
		15	0.86±0.06	10.59±1.63
		20	0.83±0.07	10.48±1.88
	variable range hopping	5	17.99±2.09	102.93±9.80
		10	20.06±1.94	112.15±9.10
		15	19.89±1.51	111.25±9.09
		20	19.25±1.77	108.22±8.26
amorphous Mo$_{0.09}$W$_{0.73}$O 500 nm	single electron hopping	5	0.54±0.03	46.62±0.96
		10	0.55±0.03	46.46±0.94
		15	0.58±0.01	45.45±0.29
		20	0.57±0.02	45.78±0.46
	ohmic conduction	5	0.50±0.03	2.21±0.96
		10	0.51±0.03	3.75±0.92
		15	0.55±0.01	5.58±0.28
		20	0.53±0.02	5.82±0.45
	variable range hopping	5	12.19±0.76	71.79±3.49
		10	12.39±0.61	72.76±2.83
		15	13.24±0.18	76.69±0.81
		20	12.94±0.16	75.28±0.73
polycrystalline Mo$_{0.05}$W$_{0.95}$O$_3$ 500 nm	thermionic emission	5	0.17±0.01	20.73±0.30
		10	0.21±0.01	17.55±0.17
		15	0.21±0.01	166.67±0.18
		20	0.19±0.01	16.61±0.17

Thus, electron flow in the amorphous $Mo_{0.05}WO$ based devices was via the single electron hopping conduction with activation energy of 0.87 eV. The electrical data from the $Mo_{0.09}W_{0.73}O$ based devices has also been fitted with the three equations (see Figure 5.6). The electron transport was found to follow the single electron hopping mechanism as concluded from a similar argument as that for the $Mo_{0.05}WO$ based device. The activation energy was found to be 0.56 eV. The fact that the activation energy in the $Mo_{0.09}W_{0.73}O$ based devices was lower than that of the $Mo_{0.05}WO$ devices was further proof that the conductivity in the $Mo_{0.09}W_{0.73}O$ devices was higher than that of $Mo_{0.05}WO$.

5.2.3.4 Electron transport in polycrystalline $Mo_{0.05}W_{0.95}O_3$

The conductivity data for the polycrystalline $Mo_{0.05}W_{0.95}O_3$ based devices was fitted with Equation 4.5 for thermionic emission transport in order to determine the activation energy for conduction. The fitted graphs are plotted in Figure 5.7, and the fitting data as well as the activation energy is summarised in Table 5.2. The fitted curves are parallel to each other, and the calculated activation energies are similar. The average activation energy was calculated to be 0.2 eV which is four times lower than that found for the amorphous $Mo_{0.05}WO$ based devices. Thus, the heat treatment on the amorphous solids greatly enhanced the conductivity of the material.

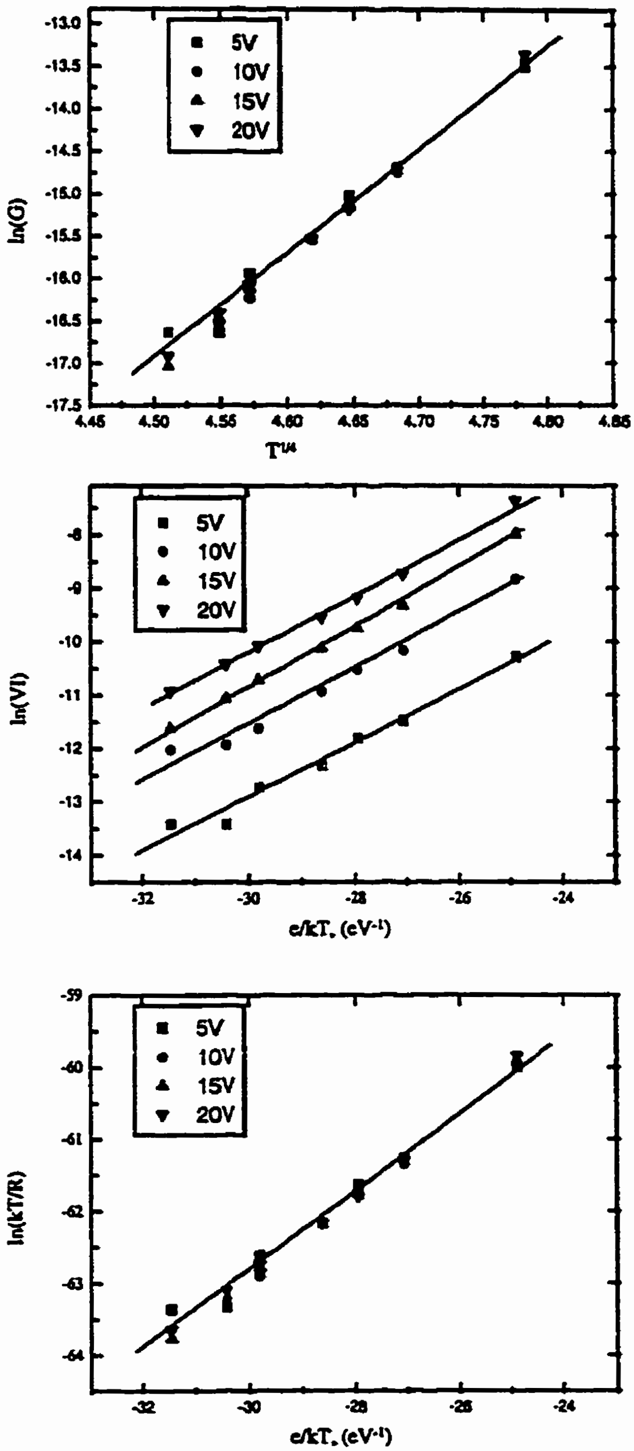

Figure 5.6 Plots of ln(G) vs. $T^{1/4}$ for variable range hopping, ln(VI) vs. (e/kT) for ohmic conduction, and ln(kT/R) vs. (e/kT) for single electron hopping conduction (500 nm amorphous $Mo_{0.09}W_{0.73}O$ based device)

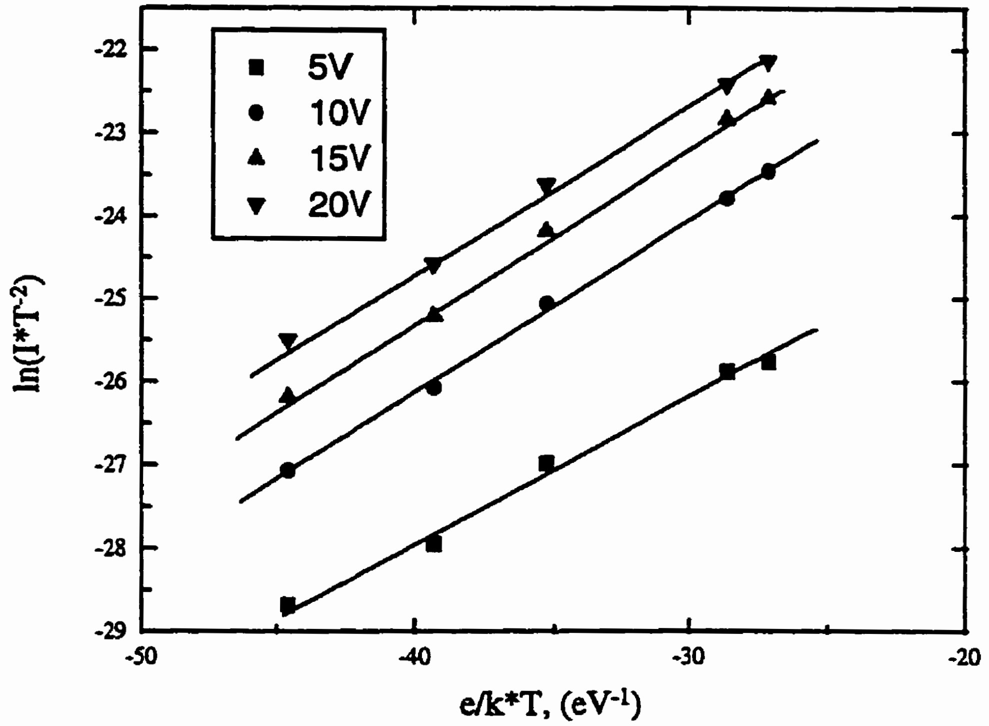

Figure 5.7 Plot of $\ln(I^*T^{-2})$ vs. e/kT for thermionic emission conduction (500 nm polycrystalline $Mo_{0.05}W_{0.95}O_3$ based devices)

5.2.4 Sensor response

5.2.4.1 Sensor response for devices based on amorphous $Mo_{0.05}WO$

The sensitivity of the amorphous $Mo_{0.05}WO$ based sensors to various concentrations of NO_2 has been monitored. Figures 5.8-11 shows the response of the $Mo_{0.05}WO$ amorphous based sensor to 0.1, 0.2, 0.5, and 1.0 ppm NO_x at 224°C. The current of the sensor decreased from 23 nA to 15 nA at 2.43 V when 1.0 ppm NO_x was introduced. However, the current only decreased from 23 to 21 nA when the concentration of NO_x introduced into the system was 0.1 ppm. Therefore, more NO_x resulted a larger change in the current of the device. The current changes and recovery times for various concentrations of NO_x at different temperatures are summarised in Table 5.3. The recovery time for the sensor operated at 184°C was 240 seconds if 0.5 ppm NO_x was applied; however, it only took 160 seconds to recover if 0.1 ppm NO_x was used at the same temperature. Thus, a greater quantity of NO_x introduced into the chamber resulted a longer recovery time. Furthermore, these devices were tested at different temperatures using the same amount of NO_x in order to study their temperature dependence. Figure 5.12 shows the sensor response to 0.1 ppm NO_x at both 184 and 197°C. It was found that a higher operating temperature results a higher conductivity in the sensor devices. The sensor operated at 197°C had approximately twice the current and half the recovery time of the sensor operated at 184°C at the same applied bias voltage. All sensors tested had a shorter recovery time at higher temperature. These sensors have been monitored for a year, and the sensing response was reproducible throughout the year.

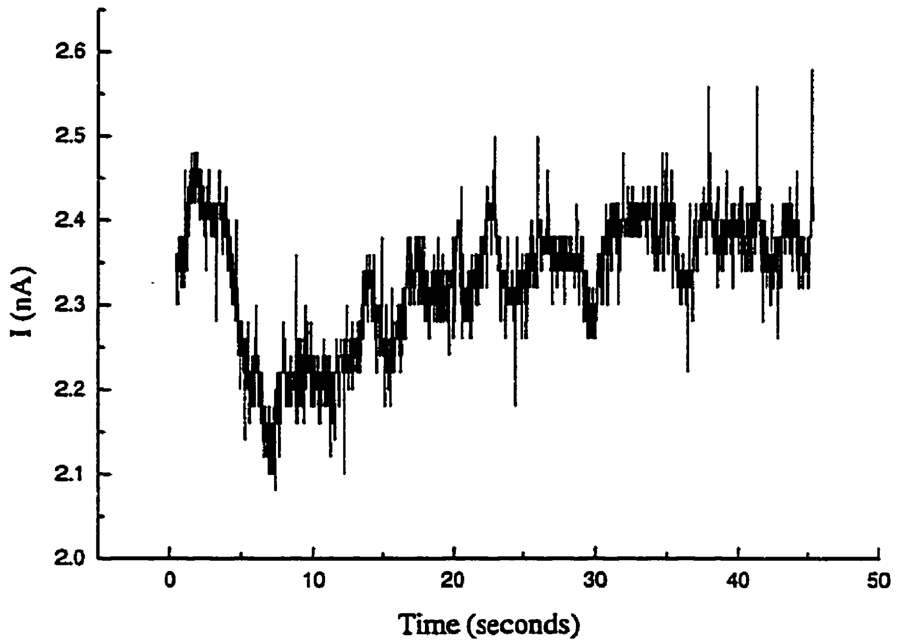

Figure 5.8 Plot of current vs. time for an amorphous $Mo_{0.05}WO$ based sensor exposed to 0.1 ppm NO_x at 224°C (500 nm)

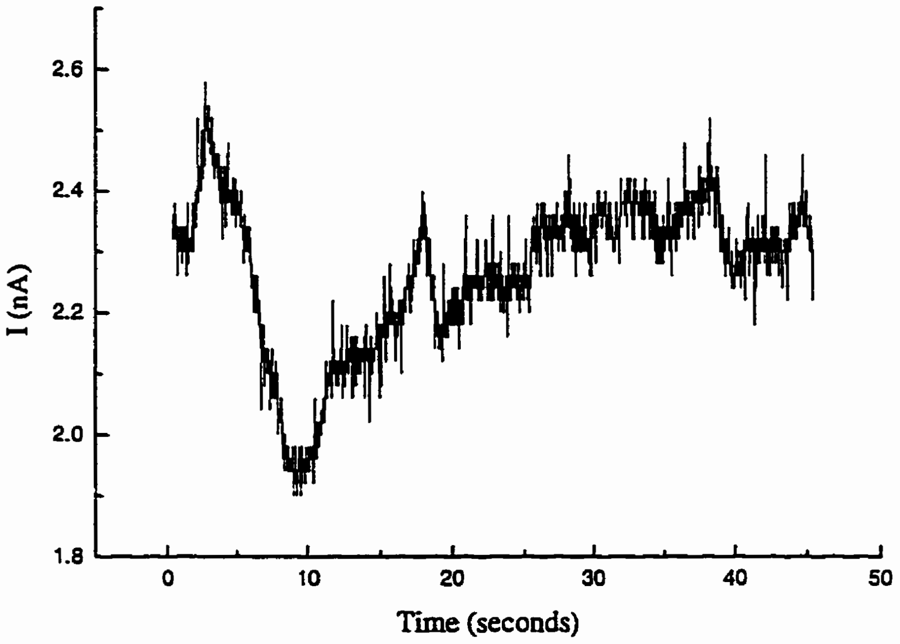

Figure 5.9 Plot of current vs. time for an amorphous $Mo_{0.05}WO$ based sensor exposed to 0.2 ppm NO_x at 224°C (500 nm)

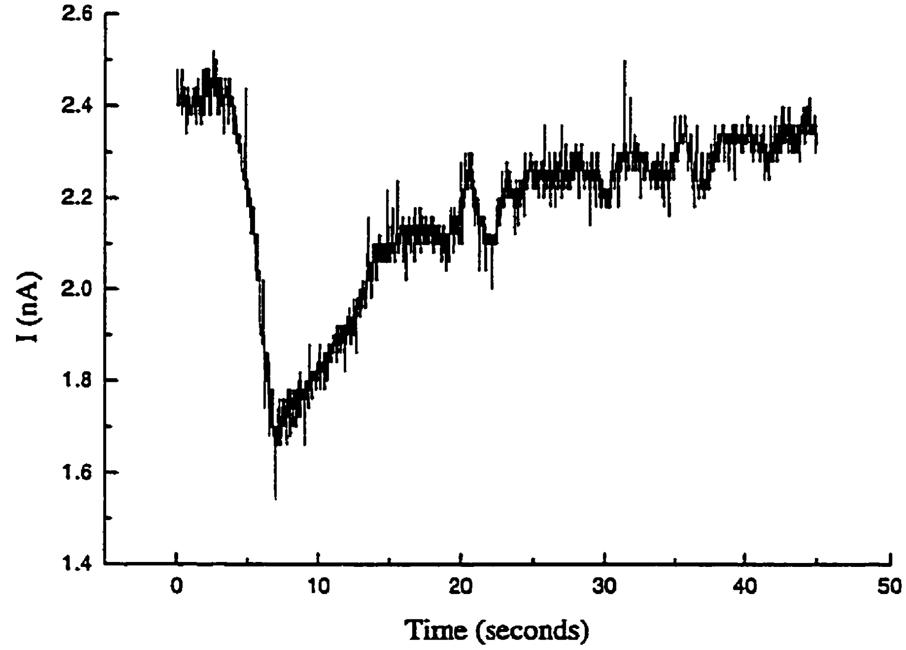

Figure 5.10 Plot of current vs. time for an amorphous $Mo_{0.05}WO$ based sensor exposed to 0.5 ppm NO_x at 224°C (500 nm)

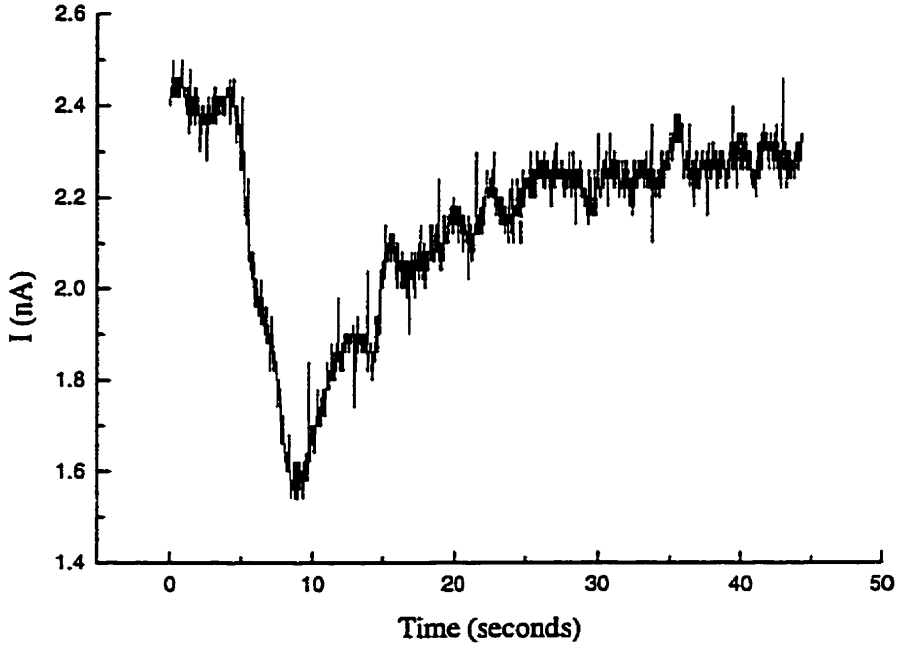

Figure 5.11 Plot of current vs. time for an amorphous $Mo_{0.05}WO$ based sensor exposed to 1.0 ppm NO_x at 224°C (500 nm)

Table 5.3 **Sensitivity of the sensor devices based on amorphous Mo$_{0.05}$WO and Mo$_{0.09}$W$_{0.73}$O, and polycrystalline Mo$_{0.05}$W$_{0.95}$O$_3$**

Active materials	Temp (°C)	ppm NO$_x$	Voltage (V)	I initial (nA)	I final (nA)	Recovery Time (second)
Mo$_{0.05}$WO amorphous	184	0.1	5.12	20	16	160
		0.1	6.26	40	33	160
		0.5	6.26	40	31	240
	189	0.1	6.18	33	28	80
	197	0.1	6.26	63	51	90
	217	0.1	5.12	59	49	40
		0.1	6.26	142	116	40
		0.5	6.26	158	120	60
	224	0.1	2.43	23	21	5
		0.2	2.43	23	19	10
		0.5	2.43	23	17	20
		1.0	2.43	23	15	20
	248	0.1	6.27	436	336	15
		0.1	5.12	193	163	10
		0.1	2.07	17	11	5
Mo$_{0.09}$W$_{0.73}$O amorphous	111	0.1	1.24	10	8	160
	158	0.1	0.23	10	7	120
		0.1	1.24	74	63	120
	172	0.1	0.05	3	1	40
	173	0.1	1.24	170	144	70
		0.5	1.24	170	115	120
	184	0.1	0.05	11	7	17
		0.5	0.05	11	7	17
		1.0	0.05	11	1	40
	189	0.1	6.18	33	28	40
	242	0.1	0.05	1300	1100	7
Mo$_{0.05}$W$_{0.95}$O$_3$ polycrystalline	96	0.1	15	4280	4220	40
	58	0.1	15	1240	1200	3600
	19	0.1	15	360	330	10800

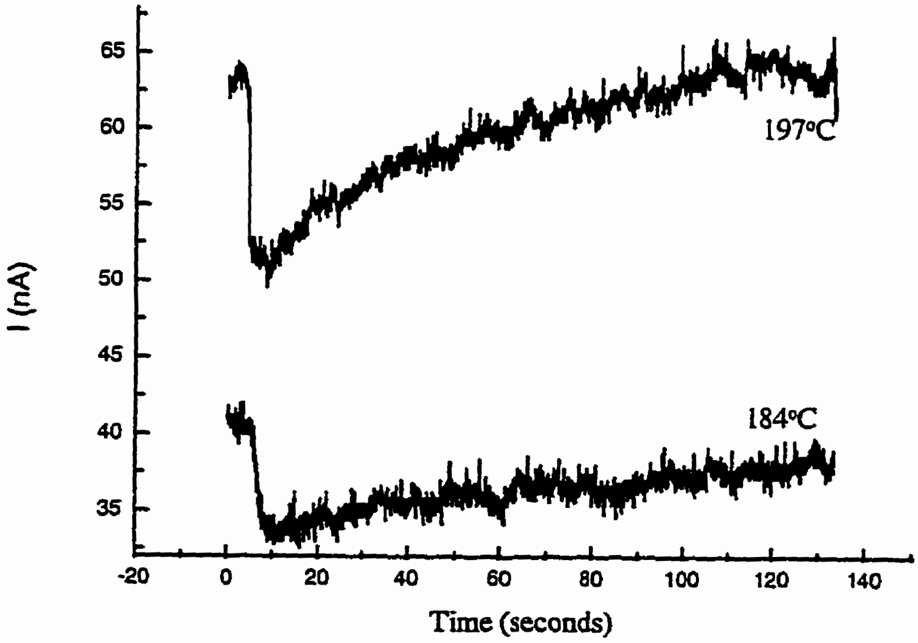

Figure 5.12 Plot of current vs. time for an amorphous $Mo_{0.05}WO$ based sensor exposed to 1.0 ppm NO_x at 184 and 197°C (500 nm)

5.2.4.2 Sensor response for the devices based on amorphous $Mo_{0.09}W_{0.73}O$

The amorphous $Mo_{0.09}W_{0.73}O$ based sensor devices have been monitored at different temperatures and with different concentrations of NO_2 (see Table 5.3). Figures 5.13-15 show the sensor response towards 0.1, 0.5, and 1.0 ppm NO_2 at 184°C. The current change was larger following exposure to a higher concentration of NO_2. The effect of temperature on the $Mo_{0.09}W_{0.73}O$ based sensor was similar to that of $Mo_{0.05}WO$ sensor. A higher working temperature resulted in a higher current and a faster recovery time (see Figure 5.16). The response of the $Mo_{0.09}W_{0.73}O$ based sensor has been monitored for a year, and the result has been found to be consistent.

5.2.4.3 Sensor response for the devices based on polycrystalline $Mo_{0.05}W_{0.95}O_3$

The sensor response of the polycrystalline $Mo_{0.05}W_{0.95}O_3$ based sensors was monitored at different temperatures and exposed to different concentrations of NO_x. The lowest temperature at which the polycrystalline based sensor can be operated was 19°C since its conductivity was still reasonably high and could be detected at this temperature. However, it took the sensor 10800 seconds to recover following exposure to NO_x. A shorter recovery time (40 seconds) was obtained when the sensor was operated at 96°C. The polycrystalline $Mo_{0.05}W_{0.95}O_3$ based sensor has been tested for a year. Its sensing behaviour stayed constant for that time period.

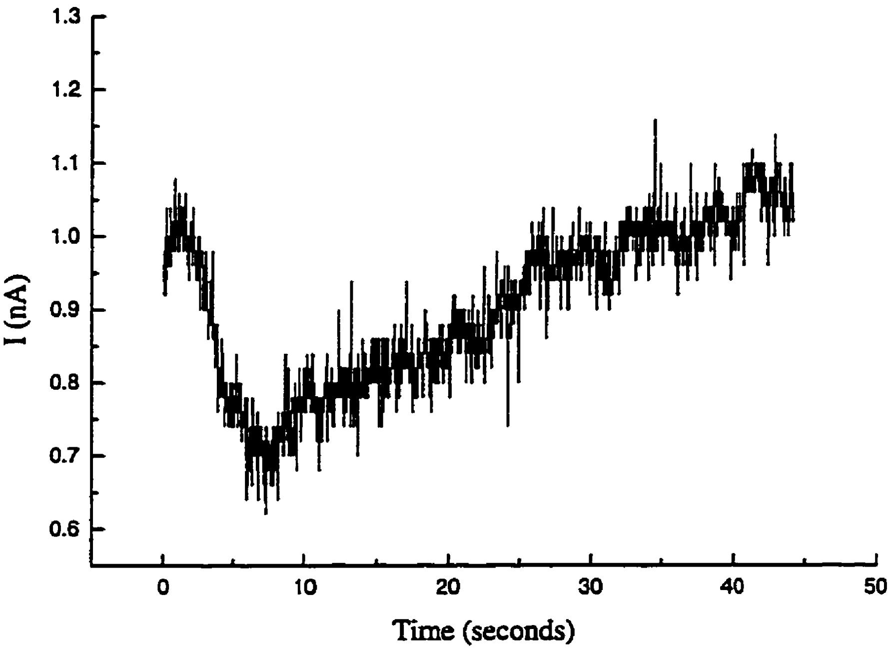

Figure 5.13 Plot of current vs. time for an amorphous $Mo_{0.09}W_{0.73}O$ based sensor exposed to 0.1 ppm NO_x at 184°C (500 nm)

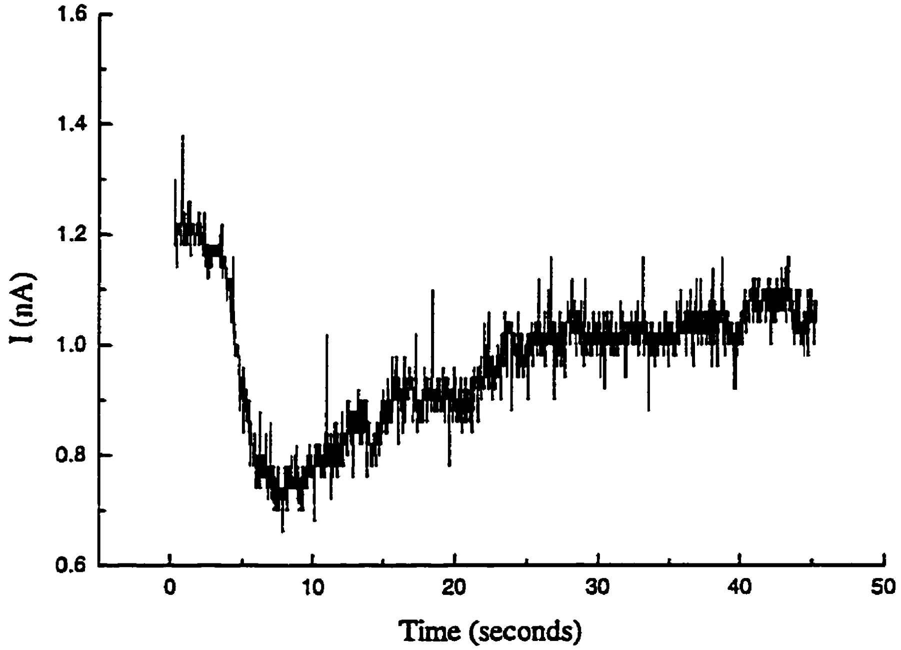

Figure 5.14 Plot of current vs. time for an amorphous $Mo_{0.09}W_{0.73}O$ based sensor exposed to 0.5 ppm NO_x at 184°C (500 nm)

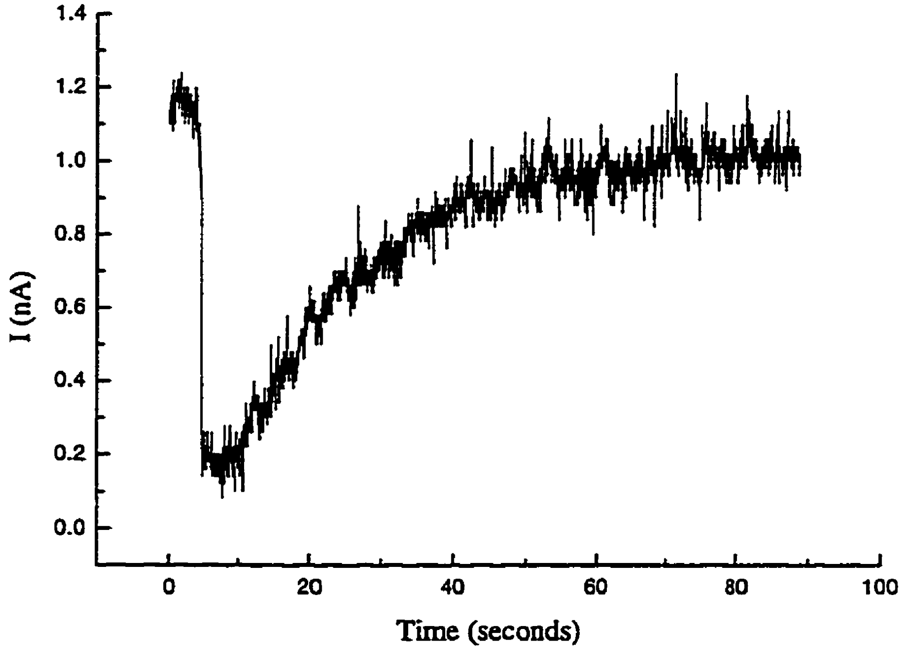

Figure 5.15 Plot of current vs. time for an amorphous $Mo_{0.09}W_{0.73}O$ based sensor exposed to 1.0 ppm NO_x at 184°C (500 nm)

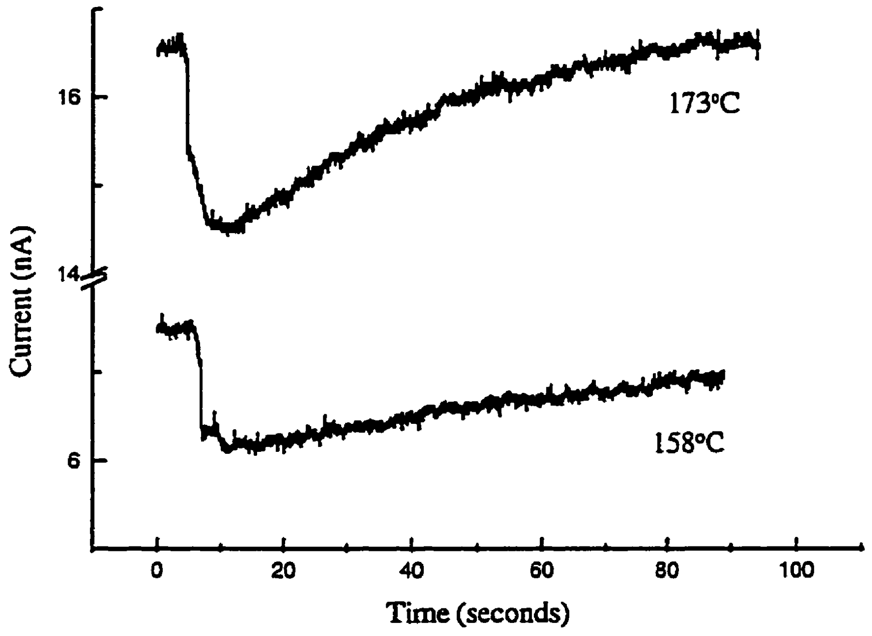

Figure 5.16 Plot of current vs. time for an amorphous $Mo_{0.09}W_{0.73}O$ based sensor exposed to 0.1 ppm NO_x at 173 and 158°C (500 nm)

5.2.4.4 Cross sensitivity

The cross sensitivity to NH_3, CO, C_2H_5OH and N_2 gases for the sensors based on molybdenum doped tungsten oxides has been tested. These gases were introduced into the gas chamber at 184°C for devices based on amorphous $Mo_{0.05}WO$, 111°C for devices based on amorphous $Mo_{0.09}W_{0.73}O$ and 19°C for devices based on $Mo_{0.05}W_{0.95}O_3$ polycrystalline materials. No cross sensitivity was found between these gases and the NO_2 for all three sensors tested. This demonstrated that the molybdenum doped tungsten oxide sensors have approximately the same specificity towards NO_x as tungsten oxide based sensors.

5.3 Conclusion

A room temperature photochemical method for the production of amorphous $Mo_{0.05}WO$ and $Mo_{0.09}W_{0.73}O$ thin film metal oxide sensors has been presented. Electrons in both the amorphous $Mo_{0.05}WO$ and $Mo_{0.09}W_{0.73}O$ based devices conducted via single electron hopping transport. The barrier height for the $Mo_{0.05}WO$ based device was found to be 0.87 eV, and 0.56 eV for the $Mo_{0.09}W_{0.73}O$ based device. Therefore, the probability for an electron to pass over the conduction barrier in the $Mo_{0.09}W_{0.73}O$ material is greater than in the $Mo_{0.05}WO$ material at a given temperature. Hence, the conductivity of the $Mo_{0.09}W_{0.73}O$ based devices is higher than that of the $Mo_{0.05}WO$ devices. Electron flow in the polycrystalline $Mo_{0.05}W_{0.95}O_3$ based devices was achieved via thermionic emission conduction, and the activation energy was found to be 0.2 eV. Therefore, the resistance of the amorphous solid was greatly decreased by the crystallisation.

The performances of these sensors were similar in that they all responded to sub-ppm NO_x. The sensing behaviour for these devices were also similar owing to more NO_x applied to the system resulted in a larger current deflection and a longer recovery time for all sensors tested. However, the operating temperatures for these sensors were somewhat different. The lowest working temperature for the amorphous $Mo_{0.05}WO$ based device was found to be 184°C while that of the $Mo_{0.09}W_{0.73}O$ based devices was 111°C. Therefore, a greater quantity of molybdenum in the starting material resulted in a higher conductivity and hence a lower working temperature. The polycrystalline $Mo_{0.05}W_{0.95}O_3$ based device has the advantage of sensing NO_x at low working temperatures (19°C); however, its recovery time is very long (10,800 s). Its recovery time can be shortened to 40 seconds if the sensor was operated at 96°C.

From the above results, it can be concluded that both enhanced performance of the sensor and the reduction in the operating temperature can be achieved by manipulating the composition of the materials. This is due to the larger quantity of oxygen defect sites in metal oxides results in higher current and hence lower operating temperatures. Thus, the composition trend for producing sensors that satisfy the requirements of low operating temperatures and high sensitivities has been found. The fabrication of pure metal oxide sensors has been achieved via the room temperature direct deposition method. Since this has proven to be an efficient process, more materials used in the fabrication of sensors which respond to various toxic gases for both environmental and emission control can be produced and tested in a similar way.

5.4 Experimental

The synthesis of the starting materials, $W(CO)_4(Et_2\text{-en})$ and $Mo(CO)_4(Et_2\text{-en})$, as well as their photo-sensitivities, are described in Chapter 3. The substrate is SiO_2 on which interdigitated aluminium electrodes were fabricated photolithographically. The dimensions of the Al electrodes are: - length = 1160 µm, width = 15 µm and spacing = 15 µm. The NO_2 gas was produced by dissolving copper in concentrated nitric acid. $Mo(CO)_4(Et_2\text{-en})$ and $W(CO)_4(Et_2\text{-en})$ were combined stoichiometrically and dissolved in CH_2Cl_2 to make a stock solution. A portion of the filtered stock solution was dropped onto a spinning interdigitated aluminium electrode. The resulting film was photolysed by placing it under a 254 nm UV lamp for a specified time in order to produce the metal oxide thin film sensor. A polycrystalline film sensor can then be produced by annealing the amorphous film sensor in air at 500°C for two hours. Films with different thicknesses were made by repeating the coating and photolysis procedure. The devices were placed in a temperature-controlled environment where the flow and concentration of different gases could be adjusted. Details on the design of the interdigitated and sensor devices as well as the general fabrication sequence was reported in Chapter 4. The oven system for testing these sensors was also described in Chapter 4.

CHAPTER 6

Conclusion

6.1 Summary of the research project

The main goal which has been achieved in this thesis was the fabrication of sensors which were capable of detecting 0.1 ppm NO_x. They were based on tungsten oxides and novel molybdenum doped tungsten oxides. These sensing materials were produced via a room temperature photochemical process which was efficient and economic.

Chapter 2 discussed the selection of the starting materials to be used in the room temperature photochemical process. The first requirement is that they must form amorphous films upon spin coating and the second is that they must be photosensitive. The first complex considered to be used as a precursor was $Cr(CO)_6$, because it was photosensitive in solution [63]. However, because of the highly symmetric shape of the complex, it formed crystalline films instead of amorphous films upon spin coating. Therefore, PPh_3 was used to replace one CO in the complex in order to lower the symmetry of the complex. The resultant complex, $Cr(CO)_5PPh_3$, formed amorphous films upon spin coating. Thus, the photochemistry of $Cr(CO)_5PPh_3$, $Mo(CO)_5PPh_3$, and $W(CO)_5PPh_3$ in the solid state was studied. These complexes were proposed to undergo the photochemical process as outlined in Equation 6.1.

$$M(CO)_5PPh_3 \xrightarrow{h\nu} M(CO)_4PPh_3 + CO \xrightarrow{h\nu} M + 5\,CO + PPh_3 \qquad (6.1)$$

where M = Cr, Mo and W.

The initial photochemical reaction generated an intermediate which decomposed upon further photolysis. In order to interpret the photochemical reactions, an orbital correlation for the $M(CO)_5PPh_3$ molecules was derived. There were two singlet excited states which could lead to the loss of one of the carbonyls and the formation of an intermediate. In order to study the photoefficiency of these complexes, a kinetic equation was derived to calculate quantum yields for two sequential photochemical processes. Their quantum yields were found to be independent of the thicknesses of the films. The relative order of efficiency was W > Mo >> Cr. Even though the photochemical processes of the three complexes were efficient, they were not used to fabricate sensors because of the phosphorus and carbon contamination in the final films. In order to improve this system, ethylenediamine ligands were used to replace one CO and the PPh_3 ligand on the metal centres. Since ethylenediamine ligands are poor π acceptor ligands, presumably, they would have less ability to stabilise low oxidation state molecules such as the intermediate. These ethylenediamine containing metal complexes were investigated in a similar manner to that used for the $M(CO)_5PPh_3$ molecules.

In Chapter 3, the solid state photochemistry of $M(CO)_4(L\text{-}L)$ (M= Cr (L-L = en, Me_2-en, Et_2-en), Mo (L-L = Me_2-en, Et_2-en), W (L-L = Et_2-en)) was reported. Metal oxide films of chromium, molybdenum and tungsten were made via the room temperature photochemical process. These films were found to be contamination free if photolysed in air. The ability to form amorphous films upon spin coating these complexes depended on both the identity of the metal and the ligands. All three chromium complexes formed amorphous films; however, of the remaining complexes only $Mo(CO)_4(Me_2\text{-en})$, $Mo(CO)_4(Et_2\text{-en})$ and $W(CO)_4(Et_2\text{-en})$ formed amorphous films. The complexes containing the Et_2-en ligands were found to be the best for forming amorphous films. All of the $M(CO)_4(L\text{-}L)$ complexes have approximate C_{2v} symmetry with four carbonyl stretching fundamentals. Their stretching absorptions in the solid state were found to be at approximately the same energy as the ones found in solution. The photochemical reaction mechanism of each of these complexes was similar and was discussed using molecular orbital theory. It was concluded that photo-dissociation of the M-N bond occurred as the primary photoprocess. The overall photochemical reaction was the loss of all ligands leaving only metals on the substrate consistent with Equation 6.2.

$$M(CO)_4(\eta^2\text{-L-L}) \xrightarrow{h\nu} M(CO)_4(\eta^1\text{-L-L}) \longrightarrow M + 4\,CO + \text{L-L} \qquad (6.2)$$

M= Cr, Mo, and W, L-L = en, Me_2-en, and Et_2-en

It was mentioned previously in Chapter 2 that the presence of a thermally stable intermediate resulted in an inefficient process. The substitution of the poor π-acceptor nitrogen ligands on the metals for the phosphorus ligands may decrease the thermal stability of the intermediate. This substitution was useful because no intermediate was observed in the photochemical reactions of the ethylenediamine containing metal complexes. The quantum yields have been measured, and the relative order of the quantum yields was found to be: $Cr(CO)_4(Et_2\text{-en}) > Cr(CO)_4(Me_2\text{-en}) \cong Cr(CO)_4(en)$ and

$Mo(CO)_4(Et_2\text{-}en)$ > $Mo(CO)_4(Me_2\text{-}en)$. The difference was assumed to arise from the electron donating ability of the organic substituents on the nitrogen ligand. Since there was no detectable nitrogen or carbon contamination inside the metal oxide films produced in air, the proposal to use a lighter ethylenediamine ligand with higher vapour pressure to replace the heavy PPh_3 ligand with lower vapour pressure has solved the purity problem associated with the heavy PPh_3 ligand. The lower molecular weight ethylenediamine ligand diffused out of the film more readily than the PPh_3 ligand. The films produced from ethylenediamine containing metal complexes in vacuum were found to contain carbon; however, the ones produced in air were found to be carbon free. Presumably, this carbon resulted from the contamination of the pump oil inside the vacuum chamber. Having produced pure metal oxide films with high efficiency, the next step was to fabricate metal oxide sensors via this efficient photochemical process.

In Chapter 4, the fabrication and the performance of tungsten oxide sensors for the detection of NO_x as well as a suggested model of the sensing mechanism were presented. The design of the sensor device and the reactor chamber for testing the performance of the sensors were also described. Sensors with different thicknesses were fabricated via the room temperature photochemical process. It was found that thicker sensors had lower resistance and hence a lower optimised working temperature. It was also found that the tungsten oxide films were oxygen deficient. Oxygen defects in the WO_3 material would result in excess electrons in the metal centres. These excess electrons reside in the band gap and provide carriers for the conduction in the semiconducting WO_3. The electron transport in amorphous materials was determined to be via variable range hopping conduction. The electron flow in the polycrystalline material was consistent with thermionic emission. For all sensors tested, the sensitivity of the sensors was not influenced by the thickness of the sensor element. However, it was found that higher NO_x concentrations and lower temperatures prolonged the recovery time. One interpretation of the response and recovery time is presented in Section 6.3.2. The sensor response of the polycrystalline WO_3 based sensors was approximately the same as the amorphous ones but with significantly lower working temperatures. All sensors were monitored for a year, and their sensing behaviours were reproducible over that time period. Even though detailed cross sensitivity tests on all gases have not been studied, preliminary results showed that these sensors were not influenced by gases other than NO_x at the optimised operating temperatures. In conclusion, NO_x sensors based on WO_3 have been made via the room temperature photochemical process, and these sensors exhibit high sensitivity and reproducibility.

Doping has been used in the electronics industry to increase the conductivity of semiconducting materials. Tungsten oxides may be doped with some other elements in order to increase their conductivity. Since contamination free metal oxide films of molybdenum and tungsten have been deposited via the efficient photochemical process, it may be possible to produce molybdenum doped tungsten oxides by this method. This may be achieved by spin coating with a solution containing both molybdenum and tungsten starting materials. If the photochemistry of each component is not affected by the presence of the other component then the deposition of mixed metal oxides may be achieved via this method. In Chapter 5, a room temperature photochemical method for the production of novel amorphous $Mo_{0.05}WO$ and $Mo_{0.09}W_{0.73}O$ thin film metal oxide sensors was presented. It was found that conduction in both the amorphous $Mo_{0.05}WO$ and $Mo_{0.09}W_{0.73}O$ based devices was via single electron hopping with a barrier height for the $Mo_{0.05}WO$ based device of 0.87 eV, and the $Mo_{0.09}W_{0.73}O$ based device of 0.56 eV. All sensors responded to sub-ppm NO_x, and the sensing behaviour of these devices were similar. The application of more concentrated NO_x applied to the system resulted in a larger current deflection and a longer recovery time. The lowest working temperature for the amorphous $Mo_{0.05}WO$ based device was found to be 184°C while that of the $Mo_{0.09}W_{0.73}O$ based devices was 111°C. A conclusion was drawn according to these observations that a greater quantity of molybdenum in the mixture resulted in a higher conductivity and hence a lower working temperature. The polycrystalline $Mo_{0.05}W_{0.95}O_3$ based device was able to respond to NO_x at low working temperatures (19°C); however, its recovery time was very long (10,800 s). The recovery time of this polycrystalline sensor was shortened to 40 seconds when the sensor was operated at 96°C.

From the above results, it was concluded that both enhanced performance of the sensor and a reduction in the operating temperature could be achieved by manipulating the composition of the materials. Moreover, the room temperature photochemical process which can be used to fabricate many materials efficiently has been shown to be an alternate approach to sensor construction. The sensors fabricated are sensitive to sub-ppm NO_x concentrations. The design of the complexes and sensors as well as the testing of the sensor performance serve as a guideline for the fabrication of various types of sensors for gas detection. It is thus the goal of the thesis not only to fabricate sensors for NO_x, but also to serve as a guideline for the fabrication of many other types of sensors. The direct deposition method largely simplified the process of fabricating the sensors, and offered the possibility of producing the devices at ambient conditions.

6.2 Comparison of these sensors with current analytical methods

NO_x sensors have been used in monitoring the emissions from chemical plants and from automobiles where the exhaust gases are at high temperature [33-39]. They are also used to detect NO_x in our daily life (environmental monitoring), where the gas particles in the atmosphere are at room temperature. The sensors fabricated in this work were directed to environmental monitoring, therefore, a comparison would be made between the conventional detector and the new sensor for environmental monitoring. The conventional nitrogen dioxide (NO_2) analysis is based on a colorimetric method: NO_2 is dissolved in water to form nitrite ions which are then reacted with a reagent to produce a reddish-purple azo dye [98, 99]. This method has 0.02 ppm sensitivity and can analyse 60 samples per hour with 8 minutes hold-up time. This method suffers from long analysing time as well as the inaccuracy of the results [100]. The inaccuracy of the results arises from the fact that NO_2 does not dissolve readily in water, and when it does, various ratios of nitrite and nitrate ions form. Therefore, the calculated results are adjusted by empirical calibration factors. In comparison, the sensors produced in this work have advantages over the conventional analyser because they offers a faster measurement time as well as the potential of being constructed in a small portable unit. In addition, the new sensors provide comparable sensitivity. Moreover, since this sensor apparently operates by monitoring the equilibrium adsorption of NO_x according to a Langmuir isotherm (see Section 6.3.2), it could be used to monitor the levels of NO_x in equilibrium with the sensor provided that the surface concentration of NO_x does not exceed the saturation level, i.e., monolayer coverage.

6.3 Future recommendations

The area of chemical sensors is very broad and the number of different solid state based gas sensors is very large. It was therefore necessary to limit the scope of this thesis to the preparation of the sensing material, the design and fabrication of the sensors as well as the search for the optimised operating conditions of the sensor. There are many directions which can be taken following this work, some of which are described in the following sections. Also included in the following is a preliminary interpretation of some of the details of the sensing mechanism.

6.3.1 Study of the uniformity

The metal oxide films produced via the room temperature photochemical process were assumed to be uniform because there were no grains or holes observed by either optical or scanning electron microscope. It was impossible to conclude more about the film structure without detailed structural studies on the uniformity of the thin films via transmission electron microscopy (TEM). Hence, a TEM study of both surfaces and cross sections of the films would be useful to study the uniformity. Even though uniformity is a key parameter for the structure of the thin film and hence the electrical properties, there have been only a few structural characterisation studies carried out on sensing materials [33, 34, 35, 38]. The surface characterisation was performed via scanning electron microscopy (SEM), and the crystallinity of the films was studied by x-ray diffractometer. From the SEM micrographs of the surface of a film, the grain size of the particles, porosity as well as the surface roughness can be determined. It has been reported that sensitivity of the sensor increased with decreasing grain size of the sensing elements [36]. This was thought to be due to the surface area for sensing: when the sensing element consisted of many small grains rather than a few large grains, a larger surface area forms. Generally, an element with a larger grain size would have higher conductivity than one with a smaller grain size. However, if the sensitivity of the sensing element would decrease with increasing grain size, it may be better to fabricate a sensor with low conductivity but high sensitivity. The current measurements on both the amorphous and polycrystalline films were performed with a similar set-up to the published sources [36-39]. However, it was difficult to compare the resistance measured in this work with the published results since the surface area as well as the type of the sensor devices were different.

6.3.2 Sensing mechanism

Although a sensing mechanism was suggested in this thesis according to the available experimental observations, detailed sensing mechanism remains unknown. In order to construct a model for the sensing mechanism, both theoretical and experimental aspects on charge transfer reactions between semiconductor surfaces and adsorbing particles must be considered [10]. In general, the adsorption of atoms results in a electronic charge transfer between the adsorbed atoms and the semiconductor and hence a conductivity change of the solid. The magnitude of the changes are related to the nature of the adsorbate particles on the surface of the substrate, the properties of the substrate itself, as well as the type of adsorption reaction between the adsorbate particles and the substrate. The rate of the adsorption may be influenced by diffusion both in the gas phase and in the sensing material. The first step in the adsorption reaction is assumed to be the physisorption between the adsorbed atoms and the substrate. After physisorption, either desorption or chemisorption (the charge transfer between the substrate and the adsorbate) may take place. Thus, the response and recovery times of the sensor are determined by the rate of reaction between the adsorbates and the substrate. In order to study each reaction separately, it is necessary to carry out the adsorption study in either thermodynamically or kinetically controlled environment. By varying temperature and pressure systematically, adsorption isotherms $f(P)_T$ and isobars $f(T)p$ can be measured for the determination of heats of adsorption. Moreover, the heat of adsorption would depend on the geometric configuration of the adsorbate as well as the sticking coefficients. The above adsorption study should be carried out on sensing element of different structures. These should include: single crystal, polycrystalline, amorphous, thin and thick films.

The gas chamber built in this work can be modified in order to study the sensor response in detail. The outlet of the gas chamber can be equipped with a mass spectrometer for the analysis of the gas phase concentrations in order to determine the concentration profile of the gas species over a period of time. The concentration profile could then be used to compare to the resistance vs. time profile of the sensor. The rate of the resistance change may be a function of both the rate of reaction between the absorbates and the sensing material as well as the diffusion in both the gas and the sensor. The adsorption of the adsorbate particles and the bulk material could be prolonged if there is diffusion of the adsorbate into the bulk. In general, the concentration of the adsorbed species was related to the change of the resistance of a sensor [33, 37, 39]. Ideally, the deflection of the current at a given bias is linearly related to the concentration of the adsorbate molecules at sub-monolayer coverage. The dose of NO_x injected into the N_2 containing hose was calculated to be 1.2×10^{14} molecules for 0.1 ppm injection, theoretically, this amount of NO_x would occupy approximately 4×4 mm^2 area. Therefore, it is assumed that the coverage of 0.1 ppm NO_x on the sensor device is approximately less than one monolayer. The dose of NO_x vs. current change profile in this thesis reflects a Langmuir isotherm, presumably, an equilibrium between the adsorbate particles and the substrate has been achieved [101]. Therefore, the response and recovery time observed in the sensor operation can be assumed to be due to processes other than the adsorption/desorption of the gas molecules on the sensor. The asymmetric shape of the observed current-time profile is consistent with the gas mixing in the chamber [102]. It is assumed that the rate limiting step in the sensing operation is the gas mixing time for the sensors operated at their optimised working temperature. The sensors operated at temperatures other than their optimised working temperature exhibits longer recovery time (see Tables 4.4 and 5.3), therefore, it reflects that the adsorption of gas particles on the sensor plays an important role on the recovery time. Even though the amount of NO_x in the chamber was calculated to cover approximately less than one monolayer of the sensor surface, the discussion of the current-concentration profile in terms of a Langmuir isotherm was not included in the main body of the thesis because it is speculative. In order to confirm this interpretation, the apparent isotherm must first be compared with one obtained under equilibrium conditions.

6.3.3 Humidity and selectivity

Preliminary results have been obtained in this work with respect to the influence from water vapour and other gases, respectively. However, detailed humidity and cross-sensitivity experiments still need to be carried out. Different chemical reactive species should be injected into the gas stream with and without NO_x at various of concentrations, respectively, in order to study the effect of these gases on the sensors. Systematically varying the humidity content in the gas stream should also be carried out in order to determine the humidity effect on the sensor devices.

6.3.4 Design and fabricate sensor devices

An ideal chemical sensor should be cheap, selective, sensitive, reproducible and microelectronic-compatible, however, current sensors on the market are far away from ideal sensors [103]. Therefore, different types of sensor devices based on tungsten oxides and/or molybdenum doped tungsten oxides should be fabricated in order to improve the quality of the sensor. For example, an integrated sensor can be fabricated with a heater and a temperature sensor on chip to maintain the sensing material at its optimised working temperature. In addition, since the room temperature photochemical process can be used to produce different materials efficiently, a sensor arrays can be fabricated with various sensing elements to monitor various of gases at the same time.

REFERENCES

1 D. A. Lynn, *Air Pollution, Threat and Response*, New York: Addison-Wesley (1976) Chapter 3.

2 P.T. Moseley, Sensors and Actuators B 6 (1992) 149.

3 J. Tamaki, T. Fujii, K. Fujimori and N. Yamazoe, Sensors and Actuators B 24-25 (1995) 396.

4 N. Yamazoe, Sensors and Actuators B 6 (1992) 9.

5 V. Demarne and A. Grisel, Sensors and Actuators B 15-16 (1993) 63.

6 Y. Cheng, Y. Li, D. Lisi, and W. M. Wang, Sensors and Actuators B 30 (1996) 11.

7 N. E. Agbor, M. C. Petty, and A. P. Monkman, Sensors and Actuators B 28 (1995) 173.

8 P. T. Moseley and D. E. Williams, Gas Sensors 8 (1989) 1615.

9 D. Baresel, W. Gellert, W. Sarholz, and P. Scharner, Sensors and Actuators 6 (1984) 35.

10 W. Gopel, Sensors and Actuators A 56 (1996) 83.

11 I. Lundstrom, Sensors and Actuators B 35-36 (1996) 11.

12 P. Camagni, G. Faglia, P. Galinetto, C. Perego, G. Samoggia, and G. Sberveglieri, Sensors and Actuators B 31 (1996) 99.

13 D. H. Yun, C. H. Kwon, H. Hong, H. W. Shin, S. Kim and K. Lee, Sensors and Actuators B 35-36 (1996) 48.

14 J. R. Brown, M. T. Cheney, P. W. Haycock, D. J. Houlton, A. C. Jones, and E. W. Williams, Journal of Electrochemical Society 144 (1997) 295.

15 M. Egashira, Y. Shimizu, Y. Takao and S. Sako, Sensors and Actuators B 35 (1996) 62.

16 D. Kohl, Sensors and Actuators 18 (1989) 71.

17 G. Sulz, G. Kuhner, H. Reitcher, G. Uptmoor, W. Schweizer, H. Low, M. Lacher, and K. Steiner, Sensors and Actuators B 15-16 (1993) 390.

18 X. Wang, W. P. Carey and S. S. Yee, Sensors and Actuators B 28 (1995) 63.

19 H. L. Tuller and R. Mlack, Sensors and Actuators B 35-36 (1996) 255.

20 W. S. Ruska, Microelectronics Processing : *An Introduction to the Manufacture of Integrated Circuits*, New York: McGraw-Hill (1987).

21 J. L. Vossen and W. Kern, Eds., *Thin Film Processes* II, San Diego: Academic Press (1991).

22 K. Wasa and S Hayakawa, *Handbook of Sputter Deposition Technology: Principles, Technology and Applications*, New Jersey: Noyes Publications (1992).

23 D. L. Smith, *Thin Film Deposition: Principles and Practice*, New York: Mcgraw-Hill, Inc. (1995).

24 L. F. Thompson, C. G. Wilson and M. J. Bowden, *Introduction to Microlithography, 2nd ed.*, Washington, D.C.: American Chemical Society (1994).

25 B. G. Streetman, *Solid State Electronic Devices*, 2nd ed., New Jersey: Prentice-Hall (1980).

26 S. M. Sze, ed., *Semiconductor Sensors*, New York: John Wiley & Sons (1994).

27 C. A. Harper and R. N. Sampson, Eds., *Electronic Materials and Processes Handbook, 2nd ed.*, New York: McGraw-Hill, Inc. (1994).

28 C. G. Granqvist, *Handbook of Inorganic Electrochromic Materials*, Amsterdam: Elsevier Science (1995).

29 D. H. Dawson, G. S. Henshaw and D. E. Williams, Sensors and Actuators B 26-27 (1995) 76.

30 N. Hykaway, W. M. Sears, R. F. Frindt and S. R. Morrison, Sensors and Actuators 15 (1988) 105.

31 J. Zhang and K. Colbow, Sensors and Actuators B 40 (1997) 47.

32 T. Ishihara, S. Sato, and Y. Takita, Sensors and Actuators B 24-25 (1995) 392.

33 P. Nelli, L.E. Depero, M. Ferroni, S. Groppelli, V. Guidi, F. Ronconi, L. Sangaletti and G. Sberveglieri, Sensors and Actuators B 31 (1996) 89.

34 C. Cantalini, H. T. Sun, M. Faccio, M. Pelino, S. Santucci, L. Lozzi and M. Passacantando, Sensors and Actuators B 31 (1996) 81.

35 C. Cantalini, H. T. Sun, M. Faccio, M. Pelino, S. Santucci, L. Lozzi and M. Passacantando, Sensors and Actuators B 35-36 (1996) 112.

36 J. Tamaki, Z. Zhang, K. Fujimori, M. Akiyama, T. Harada, N. Miura, and N. Yamazoe, Journal of Electrochemical Society 141 (1994) 2207.

37 T. Inoue, K. Ohtsuka, Y. Yoshida, Y. Matsuura and Y. Kajiyama, Sensors and Actuators B 24-25 (1995) 388.

38 F. Bregani, C. Casale, L. E. Depero, I. Natali-Sora, D. Robba, L. Sangaletti, and G. P. Toledo, Sensors and Actuators B 31 (1996) 25.

39 T. Ishihara, S. Sato, and Y. Takita, Sensors and Actuators B 30 (1996) 43.

40 L. E. Depero, I. N. Sora, C. Perego, L. Sangaletti and G. Sberveglieri, Sensors and Actuators B 31 (1996) 19.

41 M. Ferroni, V. Guidi, G. Martinelli and G. Sberveglieri, Journal of Materials Research 12 (1997) 793.

42 M. Waqif, A. M. Saad, M. Bensitel, J. Bachelier, O. Sauer, and J.-C. Lavalley, Journal of Chemical Society, Faraday Transactions 88 (1992) 2931.

43 D. D. Beck, J. M. White and C. T. Ratcliff, Journal of Physical Chemistry 90 (1986) 3123.

44 I. Lundstrom, Sensors and Actuators A 56 (1996) 75.

45 T. A. Albright, J. K. Burdett and M. H. Whangbo, *Orbital Interaction*, New York: Wiley (1988) Chapter 1.

46 V. Balzani and V. Carassiti, *Photochemistry of Coordination Compounds, 1st ed.*, New York: Academic Press (1970).

47 G. J. Ferraudi, *Elements of Inorganic Photochemistry*, New York: Wiley (1988).

48 H. -H. Perkampus, *UV-VIS Spectroscopy and Its Applications*, New York: Springer-Verlag (1992).

49 P. C. Ford, R. E. Hintze and J. D. Peterson, in A. W. Adamson and P.D. Fleischauer, Eds., *Concepts in Inorganic Photochemistry*, New York: Wiley, 1975.

50 G. L. Geoffroy, M. S. Wrighton, *Organometallic Photochemistry*, New York: Academic Press (1979).

51 B. J. Palmer, *Photochemistry of Inorganic and Organometallic Complexes in Various Media*, Ph. D. Thesis, Burnaby: Simon Fraser University (1992).

52 A. Becalska, R. J. Batchelor, F. W. B. Einstein, R. H. Hill and B. J. Palmer, Inorganic Chemistry 31 (1992) 3118.

53 M. Gao, *Solid State Photochemistry of Uranyl Carboxylate and 1,3-Diketonate Complexes: Photochemical Patterning of Uranium Oxide Lines via Uranyl Complexes Thin Film Precursors*, M. Sc. Thesis, Burnaby: Simon Fraser University (1995).

54 A. A. Avey and R. H. Hill, Journal of the American Chemical Society 118 (1996) 237.

55 L. B. Goetting, B. J. Palmer, M. Gao and R. H. Hill, Journal of Materials Science 29 (1994) 6147.

56 B. J. Palmer and R. H. Hill, Journal of Photochemistry and Photobiology A: Chemistry 72 (1993) 243.

57 S. R. Elliot, *Physics of Amorphous Materials*, New York: Longman (1983) pp.288-291.

58 W. D. Callister, Jr., *Materials Science and Engineering, An Introduction, 4th ed.*, New York: John Wiley & Sons (1997) pp. 30-60.

59 I. Lefkowitz, M. B. Dowell, and M. A. Shields, Journal of Solid State Chemistry 15 (1975) 24.

60 R.-F. Hung and W.-Y. Howng, Journal of Materials Research 11 (1996) 3077.

61 A. Gervasini, Applied Catalysis B: Environmental 14 (1997) 147.

62 A. Lecours, R. Izquierdo, M. Tabbal, M. Meunier, and A. Yelon, Journal of Vacuum Science and Technology B 11 (1993) 51.

63 F. A. Houle, and K. A. Singmaster, Journal of Physical Chemistry 96 (1992) 10425.

64 K. A. Singmaster, F. A. Houle, and R. J. Wilson, Applied Physics Letters 53 (1988) 1048.

65 H. H. Gilgen, T. Cacouris, P. S. Shaw, R. R. Krchnavek, and R. M. Osgood, Applied Physics B 42 (1987) 55.

66 T.A. Magee, C.N. Matthews,T.S. Wang and J.H. Wotiz, Journal of the American Chemical Society 83 (1961) 3200.

67 F. A. Cotton and C. S. Kraihanzel, Journal of the American Chemical Society 84 (1962) 4432.

68 D. J. Darensbourg and M. A. Murphy, Journal of the American Chemical Society 100 (1978) 463.

69 D. J. Darensbourg and T. L. Brown, Inorganic Chemistry 7 (1967) 959.

70 R. Marc Dahlgren and J. I. Zink, Inorganic Chemistry 16 (1977) 3154.

71 R. S. Drago, *Physical Methods, 2nd ed.*, New York: Saunders (1992).

72 P. Pyykko and J.-P. Desclaux, Accounts of Chemical Research 12 (1979) 276.

73 P. S. Braterman and A. P. Walker, Discuss. Faraday Society 47 (1969) 121.

74 M. Wrighton, Chemical Reviews 74 (1974) 401.

75 M. Poliakoff, Inorganic Chemistry 15 (1976) 2892.

76 K. Nakamoto, *Infrared and Raman Spectra of Inorganic and Organometallic Compounds, 4th ed.*, New York: John Wiley & Sons (1986).

77 M. S. Wrighton and D. L. Morse, Journal of Organometallic Chemistry 97 (1975) 405.

78 R. E. Dessy and L. Wieczorek, Journal of the Americal Chemical Society 91 (1969) 4963.

79 C. S. Kraihanzel and F. A. Cotton, Inorganic Chemistry 2 (1963) 533.

80 H. Saito, J. Fujita, and K. Saito, Bull. Chem. Soc. Jap. 41 (1968) 359.

81 H. Saito, J. Fujita, and K. Saito, Bull. Chem. Soc. Jap. 41 (1968) 863.

82 D. Briggs and M. P. Seah, *Practical Surface Analysis by Auger and X-ray Photoelectron Spectroscopy*, New York: John Wiley & Sons (1983) pp. 437.

83 R. Chang, *Chemistry* 4th Ed., New York: McGraw-Hill (1994) pp. 186.

84 H. Meixner and U. Lampe, Sensors and Actuators B 33 (1996) 198.

85 X. Wang, S. S. Yee and W. P. Carey, Sensors and Actuators B 24-25 (1995) 454.

86 B. Gerand, G. Nowogrocki, J. Guenot, and M. Figlarz, Journal of Solid State Chemistry 29 (1979) 429.

87 M. T. Weller, *Inorganic Materials Chemistry*, New York: Oxford Chemistry Primers (1994) pp. 38.

88 S. M. Sze, *Physics of Semiconductor Devices*, 3rd ed., New York: Wiley (1969).

89 N. F. Mott, and E. A. Davis, *Electronic Processes in Noncrystalline Materials*, New York: Clarendon Press (1979) Chapter 7.

90 M. J. Deen, A. A. Naem and L. Y. Lee, Journal of Applied Physics 76 (1994) 5253.

91 E. Salje, Journal of Applied Cryst. 7 (1974) 615.

92 L. Kopp, B. N. Harmon, and S. H. Liu, Solid State Communications 22 (1977) 677.

93 A. de Haan and A. de Croly, Sensors and Actuators B 30 (1996) 143.

94 S. R. Radel and M. H. Navidi, *Chemistry*, New York: West Publishing (1990) pp. 625.

95 R. F. Pierret, *Semiconductor Device Fundamental*, New York: Addison-Wesley (1996) pp. 484.

96 R. Belanger and J. B. Moffat, Journal of Catalysis 152 (1995) 179.

97 F. A. Cotton, G. Wilkinson, *Advanced Inorganic Chemistry*,5th ed., New York: John Wiley & Sons (1988).

98 P. N. Cheremisinoff and A. C. Morresi, *Air Pollution Sampling & Analysis Deskbook*, Ann Arbor: Ann Arbor Science (1978) pp. 152.

99 G. B. Morgan, E. C. tabor, C. Golden and H. Clements, *Automated Laboratory Procedures for the Analysis of Air Pollutants*, New York (1966) as referenced by Reference 98.

100 H. F. Lund, Industrial Pollution Control Handbook, New York: McGraw-Hill (1971) Chapter 14.

101 J. S. Winn, *Physical Chemistry*, New York: HarperCollins College (1995) pp. 1088.

102 R. D. Brann, *Introduction to to Instrumental Analysis*, New York: MacGraw-Hill (1987) Chapter 26.

103 J. Janata and R. J. Huber, *Solid State Chemical Sensors*, New York: Academic Press (1985) pp. 155.

IMAGE EVALUATION
TEST TARGET (QA-3)

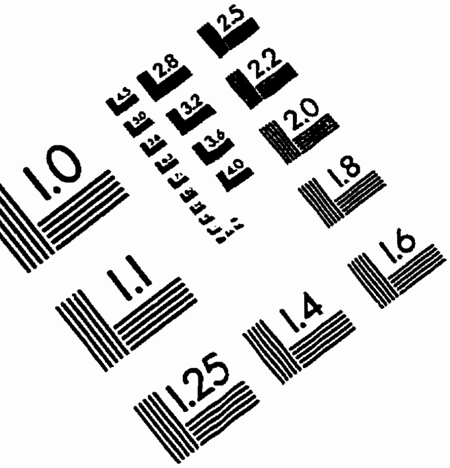

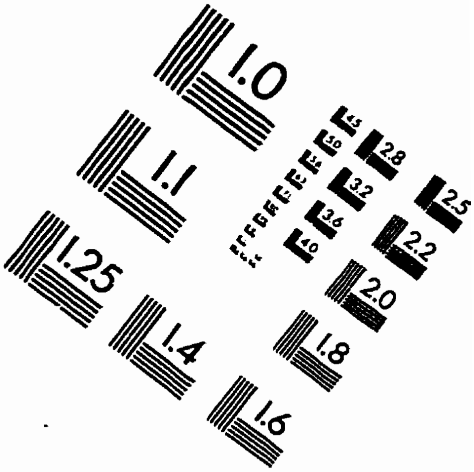

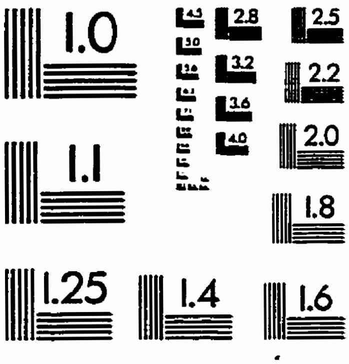

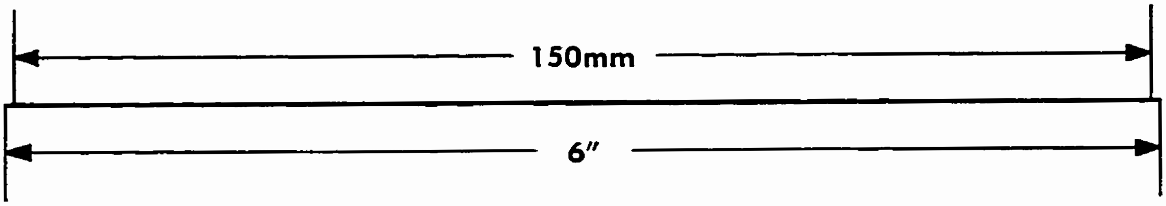

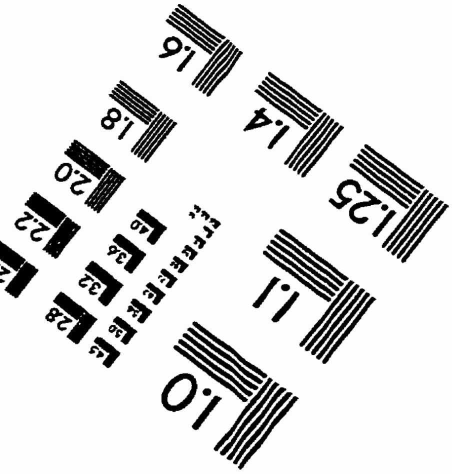

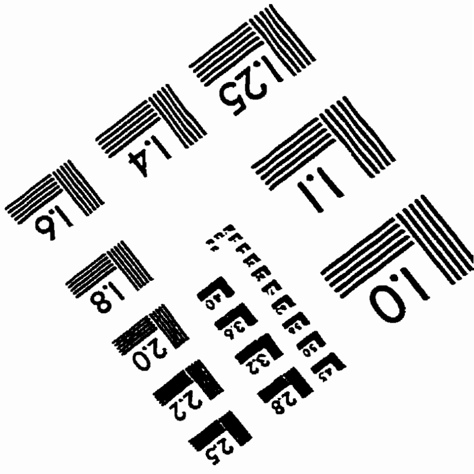

APPLIED IMAGE . Inc
1653 East Main Street
Rochester, NY 14609 USA
Phone: 716/482-0300
Fax: 716/288-5989